Oil & Natural Gas Technology

DOE Award No.: DE-FE0013531

Quarterly Research Performance
Progress Report (Period ending 12/31/2015)

Assessing the response of methane hydrates to environmental change at the Svalbard continental margin
Project Period (11/1/2013 to 10/31/2016)

Submitted by:
Marta E. Torres

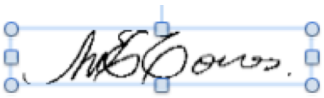

Oregon State University
DUNS #: 053599908
104 COAS Admin. Bldg.
Corvallis, OR 97331-5503
e-mail: mtorres@coas.oregonstate.edu
Phone number: (541) 737-2902

Prepared for:
United States Department of Energy
National Energy Technology Laboratory

Office of Fossil Energy

EXECUTIVE SUMMARY

In November 2013, Oregon State University initiated the project entitled: **Assessing the response of methane hydrates to environmental change at the Svalbard continental margin**. In this project, we will take advantage of a unique opportunity to collect samples from the Svalbard continental margin. The overall objective of this research is to constrain the biogeochemical response of the gas hydrate system on the Svalbard margin to environmental change. Because of a delay in the planned expedition, we reconfigured the program based on discussions with NETL program managers and submitted a revised SOPO. In the new plan, we will collect samples in three expeditions, the first of which happened Oct 7-21, 2014. We were able to also join an expedition to the area onboard the RV Helmer Hanssen during May15-29, 2015 and another one onboard the RV Heincke August-September 2015. This completes the sampling tasks of the project. We have began analyses of the samples collected during these expeditions as well as completed a computational model for methane hydrate formation under conditions of variable salinity.

PROGRESS, RESULTS, AND DISCUSSION

1. Expedition(s) update: We participated in a cruise onboard the RV Heinke in August-September 2015, which was focused on collecting water column samples along the Svalbard and Barents Sea margins. A cruise report is attached
2. Water column results. We conducted extensive sampling campaign of the water column along the entire Barents Sea-Svalbard margin in August-September 2015, including the shelf regions, to document the significance of methane release at the upper limit of gas hydrate stability relative to additional sources on the shelf. Water and air samples collected during two RV Heinke expeditions indicate that the methane released in the slope does not contribute to the atmospheric input, however the shelf regions do. In addition extensive hydroacoustic surveys along the entire edge of has hydrate stability do not show any methane discharge expect for the well-studied region offshore Prins Karl Foreland.
3. Geochemistry: We continue the analyses from the various expeditions, which include carbon isotopes in the DIC, oxygen and hydrogen isotopes in water and nutrient concentrations. Preliminary data from a series of cores recovered at on the fan of Storfjordrenna, west Barents Sea from a location where gas hydrate was recovered as shallow as 0.82 mbsf indicate that the increase in methane flux inferred sulfate profile, may be linked to an enhanced gas hydrate dissociation in this area. Ongoing studies are aimed at testing this postulate, with the aim to bridge the gap between hydroacoustic flare detection in the water column and the mapping of hydrate reservoir at depth, and provide additional clues to unravel the complex interactions among ice, ocean, microbiology and climate and their sensitivity to both natural and anthropogenic change in Arctic regions. A data report is attached. We will present these results at the upcoming Gordon Conference on Natural Gas Hydrates next February, 2016. We expect to submit a manuscript on these observations early 2016.
4. Microbiology. Static high-pressure bioreactors were used to incubate sulfate-methane transition zone (SMTZ) samples from below a gas flare off Svalbard at saturating (3.8 MPa) and 0.2 MPa methane are being sampled after 1 week, 4 weeks, and 4 months; sul-

fide production rates of 8-18 nmol/cm^3/day were first observed after 4 weeks of incubation. Sediment samples at all specified time points for both sets of incubations were collected for nucleic acid extraction and cell fixation. These results are compared with samples from a Mediterranean mud volcano gas flare, and presented at the AGU Fall meeting (Dec. 2015). A more thorough understanding of AOM community dynamics in response to changes in methane concentrations is expected to yield more accurate carbon cycling models pertaining to the world's largest reduced carbon reservoir.

5. Modeling- A manuscript entitled " Methane hydrate formation under conditions of variable salinity II. Time-stepping variants and sensitivity of reduced numerical model" by M. Peszynska, F. P Medina, W-Hong, M.E. Torres is in the final stages of editing; galley proofs are attached to this report. In this paper we consider a reduced model of methane hydrate formation in variable salinity conditions presented in a companion paper, and give details on discretization and three time-stepping variants: Implicit, Semi-implicit, and Sequential. We compare their accuracy and efficiency depending on the spatial and temporal discretization parameters. We also study sensitivity of the model to the simulation parameters and in particular to the reduced phase equilibria model. (Keywords methane hydrate formation; numerical discretization; implicit and non-implicit time-stepping; model sensitivity and convergence; multiphase multicomponent model).

PROBLEMS OR DELAYS

No new problems since the set-back last year when the planned expedition in the R/V M.S. Merian got cancelled due to massive engine failure of the vessel. We completed our expedition plan to the area as documented in the revised project plan and added an additional cruise on the RV Hanssen in May 2015.

PRODUCTS

- FITI article. An article summarizing these results entitled "Gas Hydrate, Carbonate Crusts and Chemosynthetic Organisms on a Vestnesa Ridge pockmark" was published in the Fire in the Ice, volume 15, issue 2, pages 14-17.
- Geochemistry Data Report, summarizing pore water data from the expeditions to the region is attached
- Cruise report from Expedition HE 450, is attached
- Abstract of poster presentation at the American Geophysical Union Fall Meeting, (Dec 2015) describing resilience and dynamics of anaerobic methane-oxidizing microbial communities to short-term changes in methane partial pressures, is attached.

CRUISE REPORT R/V Heinke HE450

Investigating of gas emission sites at the seafloor of the western margin of Spitsbergen

Tromsø to Tromsø

25 August - 08 September, 2015

Prof. Gerhard Bohrmann, Chief Scientist

Participants: Ferreira, Christian; Hong, Wei-Li; Hsu, Chieh-Wei; Lange, Mirko; Loher, Markus; Pape, Thomas,;Torres, Marta; Wintersteller, Paul; and Yao, Haoyi

Cruise Summary

The objective of the cruise was to explore methane emission sites along the continental margin of the Barents shelf and Svalbard areas to understand their relationship to geological structures, sediment deposits and hydrocarbon sources. We used the hydro-acoustic systems of the ship (multibeam EM710, fish finder EK60, and the narrow-beam parametric sub-bottom profiler SES2000) to detect gas emissions as anomalies in the water column (so-called flares), and accumulations of free gas in the sediment imaged as blanking zones in the sub-bottom sonar records. We sampled the water column using a 12 bottle rosette mounted on the R/V HEINCKE Sea Bird Electronics (SBE) 911 CTD (conductivity, temperature, depth) profiler, and measured the methane concentrations using a new technique with an off-axis integrated cavity output spectrometer (OA-ICOS). This instrument was also used to measure the methane in air using its continuous flow option. The sampling stations were selected based on gas emission surveys, geological provinces and local oceanographic pathways that are part of the general sea water circulation along the margin of the northernmost Atlantic. In addition, we sampled sediments at specific stations and extracted pore water and gas to better understand the relation of gas hydrate dynamics and gas seepage.

The cruise started on Tuesday, 25 August 2015 in Tromsø and followed along the 400m isobath to the north beginning at the Bjørnøya Trough mouth and surveyed over cross shelf troughs like the Kveithola, Storfjordrenna, Hornsund, Bellsund, and Isfjord reaching the Kongsfjord at the northern end of the transect. Due to strong winds of Beaufort 6 and 7 between 28 to 31 August, we could not reach the Vestnesa Ridge area and sampled instead the inner Kongsfjord. On the way back south we completed our sampling stations based on the knowledge we gained on the way to the north. In total we mapped the margin by analyzing the bathymetry and flare imaging along 2,400 nautical miles. We took 37 CTD stations with water samples in different water depths, 5 grab samples, 2 gravity cores and 2 mini-corers. The cruise ended with the entry to the harbor of Tromsø on Tuesday 08 September 2015.

1 Preface

Gas emissions from the continental margin and the shelf west of Spitsbergen became recently well known (e.g. Westbrook et al. 2009; Sahling et al. 2014). Specifically west of Prins Karls Forland gas emissions in around 400 m water depth have been interpreted from decomposing hydrates due to a temperature increase from 2°C to 3°C over the last 30 years (Westbrook et al. 2009). Although this interpretation is not accepted by all scientists the global impact of that mechanism would be very important in the context of global change. Investigations on that problem are therefore highly welcome. During R/V HEINCKE HE450 (Fig. 1) we explored gas emissions using the echosounders of the ship along the slope of the Barents Sea up to Svalbard to find more evidence for dynamic changes of gas hydrates and emissions of free gas.

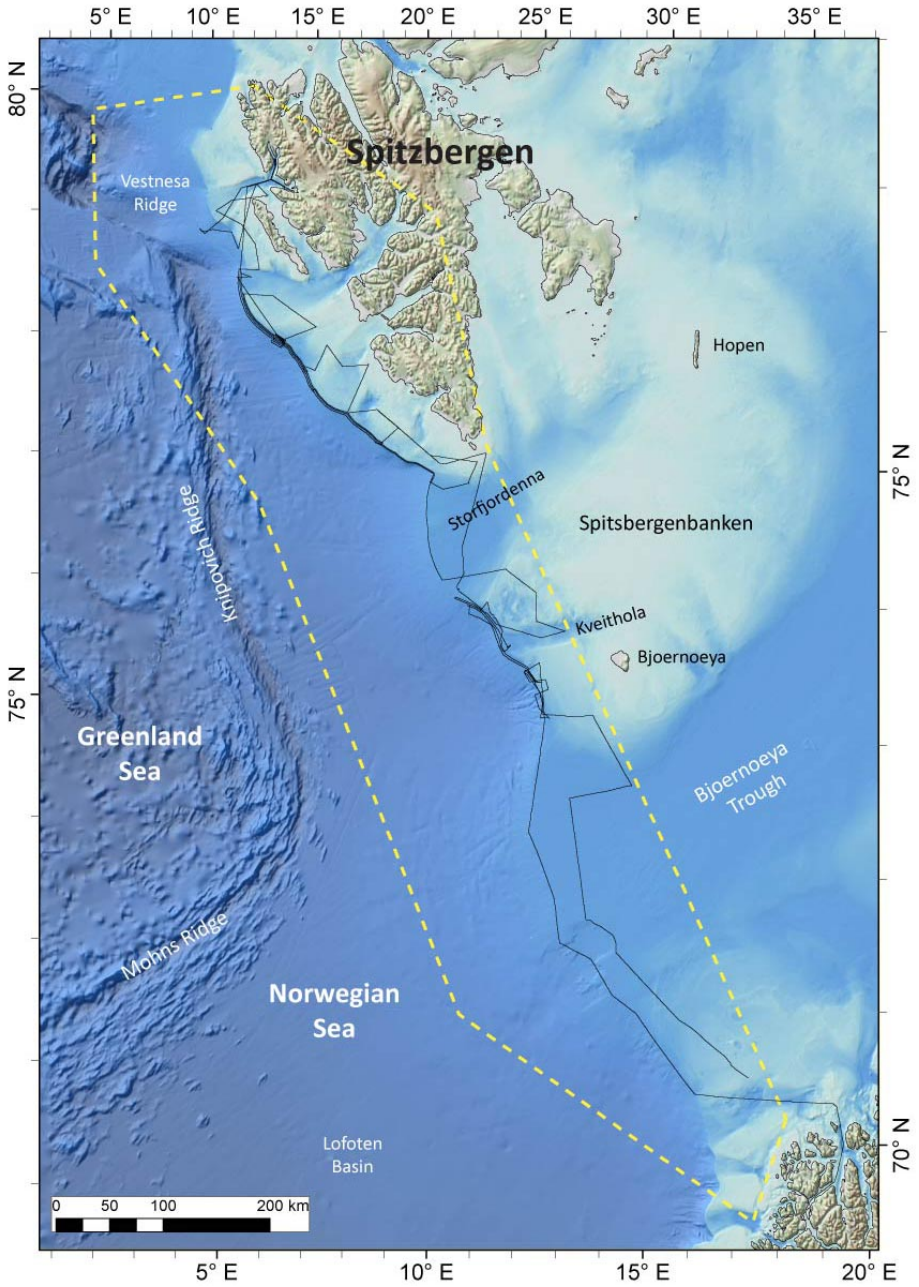

Fig. 1: Track lines of R/V HEINCKE Cruise HE450 along the northernmost European margin of the Nordic Seas. The outline of the area of permission is shown by the stippled line.

R/V HEINCKE Cruise HE450 was requested and planned within the BMWi project IMGAM „Intelligentes Monitoring von klimaschädlichen CO_2/CH_4 Gasaustritten im Meer“, to investigate gas emission sites at the seafloor of the western margin of Spitsbergen. The cruise was coordinated and carried out by MARUM Center for Marine Environmental Sciences at University of Bremen, with participation from scientists from Oregon State University and the Center for Gas Hydrate, Environment and Climate. We acknowledge the Master of the vessel Werner Riederer, and his crew for their continued contribution to a pleasant and professional atmosphere aboard R/V HEINCKE. We thank the German Federal Ministry of Economics and the United States Department of Energy, National Energy and Technology Laboratory for financial support of the project.

Fig. 2: Scientific crew onboard R/V HEINCKE HE450. The photo was taken in Ny Ålesund where R/V HEINCKE berthed for two hours, while the scientists visited the German Koldewey Station in this northernmost settlement of scientists.

Personel aboard R/V HEINCKE

Table 1: Scientific crew

Name	Discipline	Affiliation
Bohrmann, Gerhard	Chief scientist	MARUM
Ferreira, Christian	Multibeam	MARUM
Hong, Wei-Li	Pore water chemistry	CAGE
Hsu, Chieh-Wei	Mapping, sediments	GeoB
Lange, Mirko	Chemistry, ICOS	GeoB
Loher, Markus	Sediments, mapping	MARUM
Pape, Thomas	Gas analyses, Cores	MARUM
Torres, Marta	Cemical analyses	OSU
Wintersteller, Paul	IT, mapping	GeoB
Yao, Haoyi	Geochemistry	CAGE

MARUM Center for Marine and Environmental Sciences, DFG Research Center and Cluster of Excellence, University of Bremen, Postfach 330440, 28334 Bremen, **Germany**

GeoB Department of Geosciences, University of Bremen, Klagenfurter Str., 28359 Bremen, **Germany**

OSU Oregon State University, Corvallis OR, **USA**

CAGE Centre for Arctic Gas Hydrate, Environment and Climate, Dramsveien 201, 9010 Tromsø, **Norway**

Fig. 3: Crew members onboard R/V HEINCKE HE450.

Table 2: Crew members onboard

Name	Discipline	Name	Discipline
Riederer, Werner	Master	Trautmann, Stefan	A.B.
Franke, Remo	Chief Mate	De Vries, Steffen	A.B.
von Aswegen, Marvin	2.NO	Vareiro Do Amaral, Bruno	A.B.
Klinder, Klaus-Dieter	Chief Engineer	Heeren, Derk	A.B.
Starke, Wolfgang	Electrician	Dräger, Martin	A.B.
Baron, Heiko	Boatswain	Klafack, Ronald	Cook

Shipping operator: Briese Schiffahrts GmbH & Co KG, Abteilung Forschungsschifffahrt, Hafenstr. 12, 26789 Leer, **Germany**

2 Introduction (Gerhard Bohrmann, Marta Torres)

2.1 Geological Setting of Svalbard and Barents Sea Shelf

Svalbard forms an Arctic archipelago at the northwestern edge of the Barents shelf, far north of Norway. Svalbard is the official Norwegian name for the archipelago, which includes all islands between 74° and 81°N, and 10° and 35° E like Spitsbergen, Bjørnøya, Hopen and Kong Karls Land. Geologically Svalbard is the emergent northwestern corner of the Barents shelf, which was uplifted by Late Mesozoic and Cenozoic crustal movements. The record of rocks ranges in age from Precambrian to Recent and the geological history includes several tectonic events from Neoproterozoic to Early Palaeogene. Passive continental margins occur to the north to the Eurasian Basin and offshore to the west to the northern part of the Atlantic Ocean where the Knipovich Ridge is forming the plate boundary between the North American and the Eurasian Plates. The central part of the ridge, the active spreading zone is highly segmented by transform faults from which the Molly and Spitsbergen Fracture zones are the pronounced examples. When seafloor spreading started in the Nordic Seas in the Eocene about 52 Ma ago (Magnetic Anomaly 24), Svalbard and the Barents Shelf were tectonically separated from Greenland by a continental transform fault system from which the present Hornsund Fault complex was part of it (Dallmann 2015).

The Barents Sea Shelf between Svalbard and Fennoscandia is a platform area. Precambiran crust is mainly buried under thick pile of Late Palaeozoic to Neogene sedimentary rocks. The western margin includes an extension of the Ordovician-Silurian (Caledonian) Orogen. Structural basins and elevations of the sedimentary sequences were formed under the influence of transform faulting and crustal extension during the formation of the North Atlantic basin. Those basins like the Sørvestsnagsen (Perez-Garcia et al. 2013) Trømsø or Hammerfest basins (Ostanin et al. 2013) contain oil and gas fields often with shallow gas deposits. Leakage of thermogenic methane was well shown in seismic records and seafloor expressions like pockmarks and acoustic flares (e.g. Ostanin et al. 2013; Chand et al. 2012).

The western margin of Spitsbergen is influenced by the landward continuation of the slow-spreading Knipovich Ridge. It is a segmented, sheared transform margin partly characterized by under-plating of thinned oceanic crust (Ritzmann et al., 2004) which may generate together with magmatic intrusions at the continent-ocean boundary a higher geothermal gradient (Vanneste et al. 2005). The area was repeatedly glaciated and accordingly experienced rapid changes in sea-level sedimentation and erosion (Landvik et al. 2005; Svendsen et al., 2004). The ice of the Svalbard-Barents Sea Ice Sheet of the last major glaciations on Svalbard retreated from this margin approximately 13 ka ago (Landvik et al., 2005). The present rate of uplift in Svalbard is 4-5 mm/yr (Sato et al., 2006), which is a combination of post-glacial rebound and acceleration from recent ice loss of retreating glaciers on Svalbard.

The western continental shelf off Svalbard is morphologically characterized by the glacial cross shelf troughs of Kongsfjord, Isfjord, Bellesund, Hornsund and Storfjord, their lateral and terminal morainal ridges and their broad trough mouth fans. The sedimentary architecture is composed of glacigenic debris flows of the trough mouth fans (TMF), hemipelagic glacio-marine sediments occasional forming drift bodies of contourite deposits and the transitional areas between them. The alternation of hemipelagic deposits with stacked debris flows have been identified to play an important role for preconditioning of submarine slides due to the increase of pore pressure in sediments between less permeable layers under load (Winkelmann & Stein 2007). Fluid and gas migration on this shelf occurs

along major geological structures (Knies et al. 2004). The occurrence of large areas with bottom-simulating seismic reflectors indicates the presence of gas hydrates and pockmarks (Vogt et al. 1994; Vanneste et al. 2005).

2.2 Gas Venting at the Western Svalbard Margin

The Arctic region is warming faster than other regions on our planet. Since the Arctic Ocean is also storing methane hydrates at its margins, significant amounts of methane can be released (Archer and Buffett, 2005). Hydrates are stable under low-temperature and high-pressure conditions. Methane hydrates in high-latitude regions are characterized by relatively low bottom-water temperatures and can therefore persist in relatively shallow water depths. Because those regions are highly sensitive to increase in bottom-water temperatures in the course of global warming, shallow hydrates are highly susceptible to thermal dissociation, which might lead to methane release from the seafloor. Moreover, methane escaping the seafloor at shallow depths eventually reaches the atmosphere, where it might contribute as greenhouse gas to further global warming (Mienert et al. 2010).

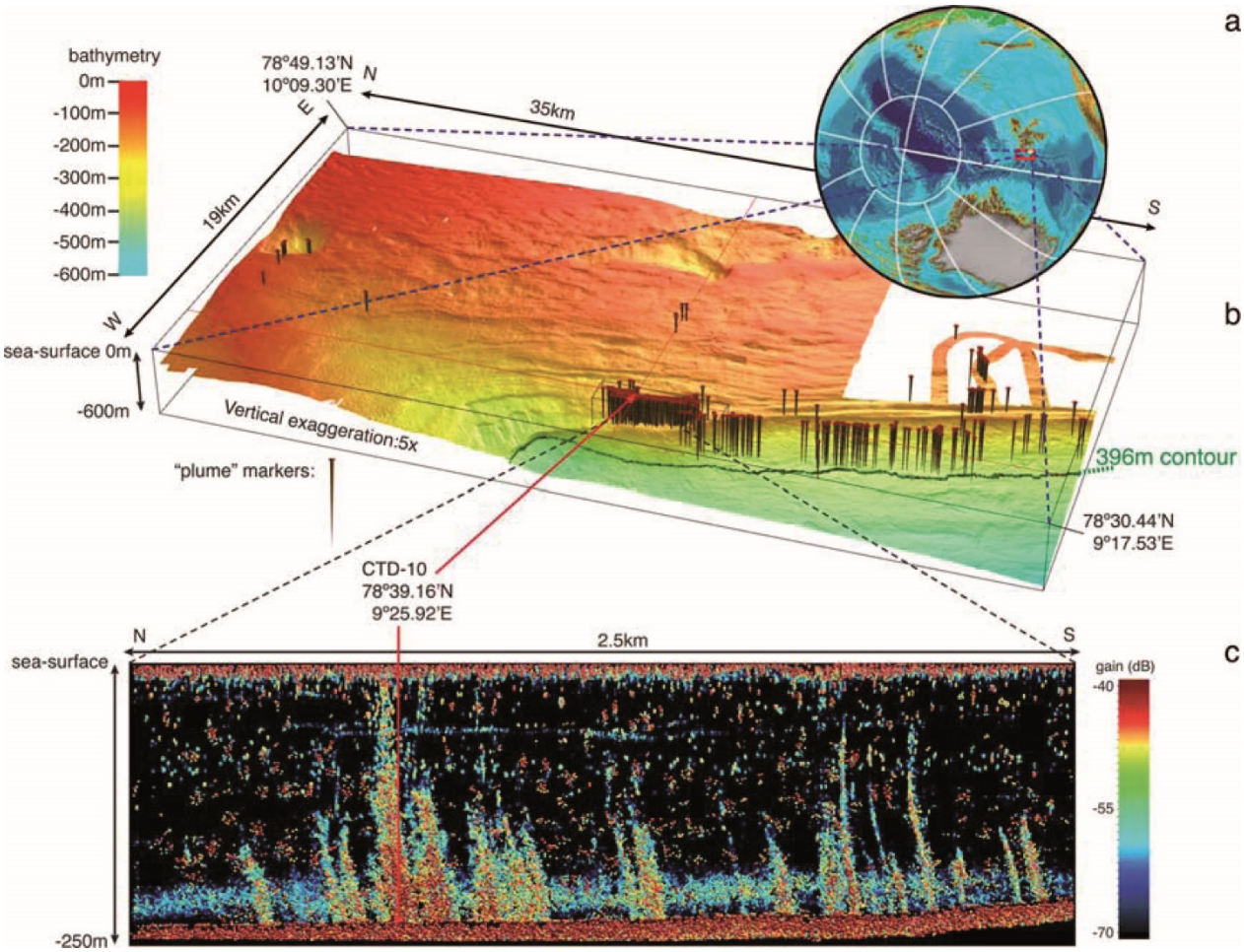

Fig. 4: Location of survey west of Svalbard (a), position of flares imaged by EK60 during JR211 superimposed on perspective view of bathymetry (b), part of the record from the acoustic survey showing examples of observed gas plumes (from Westbrook et al. 2009).

In this light, the finding of numerous gas emissions at the continental margin west of Svalbard (Fig. 4) concentrated along the 396 m isobaths representing the upper limit of the gas hydrate stability zone was alarming. Westbrook et al. (2009) argued that during the last three decades, the bottom water at that depth has increased from 2°C to 3°C assuming that the upper boundary of the GHSZ deepened from 360 m to 396 m. This temperature increase could have caused hydrate dissociation in the sediments and, as a consequence, bubbles of free gas are emitting to the water column (Fig. 5). If this interpretation is right, then this location would be the first site where the hypothesis of global warming-induced hydrate dissociation may actually be confirmed.

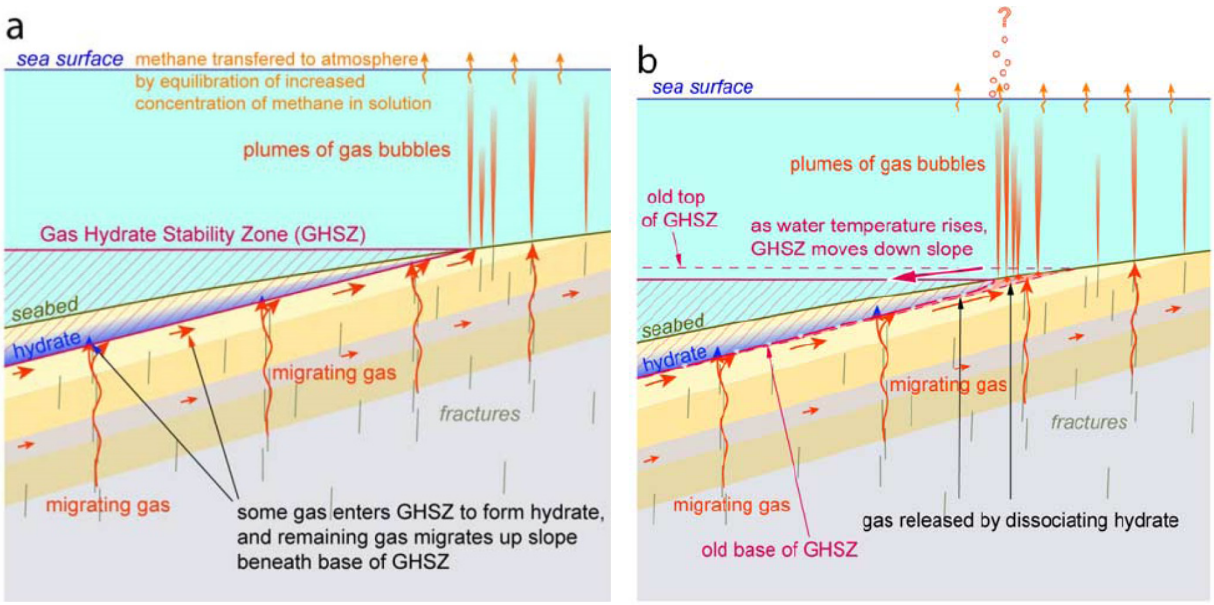

Fig. 5: Scenario described by Westbrook et al. (2009): (a) Migrating methane gas is restricted from reaching the seabed in the GHSZ by its conversion to hydrate and by the overall reduction in permeability caused by the growth of hydrate at the base of the GHSZ. Methane gas escaping from the seabed beyond the GHSZ rises as bubbles through the seawater. (b) An increase in the temperature of the seawater causes the GHSZ to contract down slope, dissociating hydrate to methane and water. Where the GHSZ is removed entirely, all the released gas is free to move to the seabed, guided by local variation in lithology and structure. Where a thinner GHSZ remains, gas from the dissociated hydrate at its base can migrate into the GHSZ to form hydrate again and may also migrate up slope.

Westbrook et al. (2009) also offered an alternative hypothesis for the slope-parallel presence of seafloor gas emissions. Free methane in the deep slope sediments may migrate upward along the base of the GHSZ, because of the sealing effect of concentrated hydrate (Fig. 5). The free gas could escape the sediments where the GHSZ is outcropping and could therefore explain a clustering of the gas emissions at the depth around 396 m. Theories including gas hydrates to explain the clustering of emission sites around 396 m are not verifiable, because gas hydrates have not been documented by sampling or geophysical documentation so far. Sampling using conventional methods like gravity or piston coring from research vessels failed up to now because of the difficult lithology, which did not allowed for cores to penetrate. Sampling this shallow sediment sequence by drilling using a mobile drilling system (Freudenthal and Wefer 2014) will probably happen in August 2016 and is even not available by now. The presence of hydrate is documented by a clear bottom-simulating seismic reflector (BSR) at this continental margin below 600 m water depth (Vanneste et al., 2005; Chabert et

al., 2011). In addition, hydrates were recovered from shallow sediments in around 900 m water depth (Fisher et al., 2011).

Further investigations at gas emission sites were performed by Berndt et al. (2014). Uranium–thorium dating of methane-derived authigenic carbonates sampled at the seafloor of the gas emission sites revealed ages of up to 3000 years for the carbonate formation. Since carbonate precipitation is related to anaerobic oxidation of methane (AOM) triggered by gas seepage, gas emissions at the seafloor at 396 m water depths are not only related to the warming of bottom water and the potential shift in the gas hydrate stability zone (Berndt et al. 2014). The findings suggest a long history of methane seepage, which clearly weakens the hypothesis of recent global-warming-induced hydrate decomposition.

Gas-related seismic features occur at the upper slope and outer shelf in varies water depths (Ker et al. 2014; Sarkar et al. 2012; Rajan et al. 2012) and gas emissions occur not only at the upper boundary of the GHSZ (Westbrook et al. 2009). Typical hydrocarbon seep-related bacterial mats were observed at the shelf (Knies et al., 2004). Elevated bottom-water methane concentrations and the stable carbon isotope composition of methane in the water column indicate seepage at the shelf and within the fjords of Spitsbergen (Damm et al. 2005; Gentz et al. 2014).

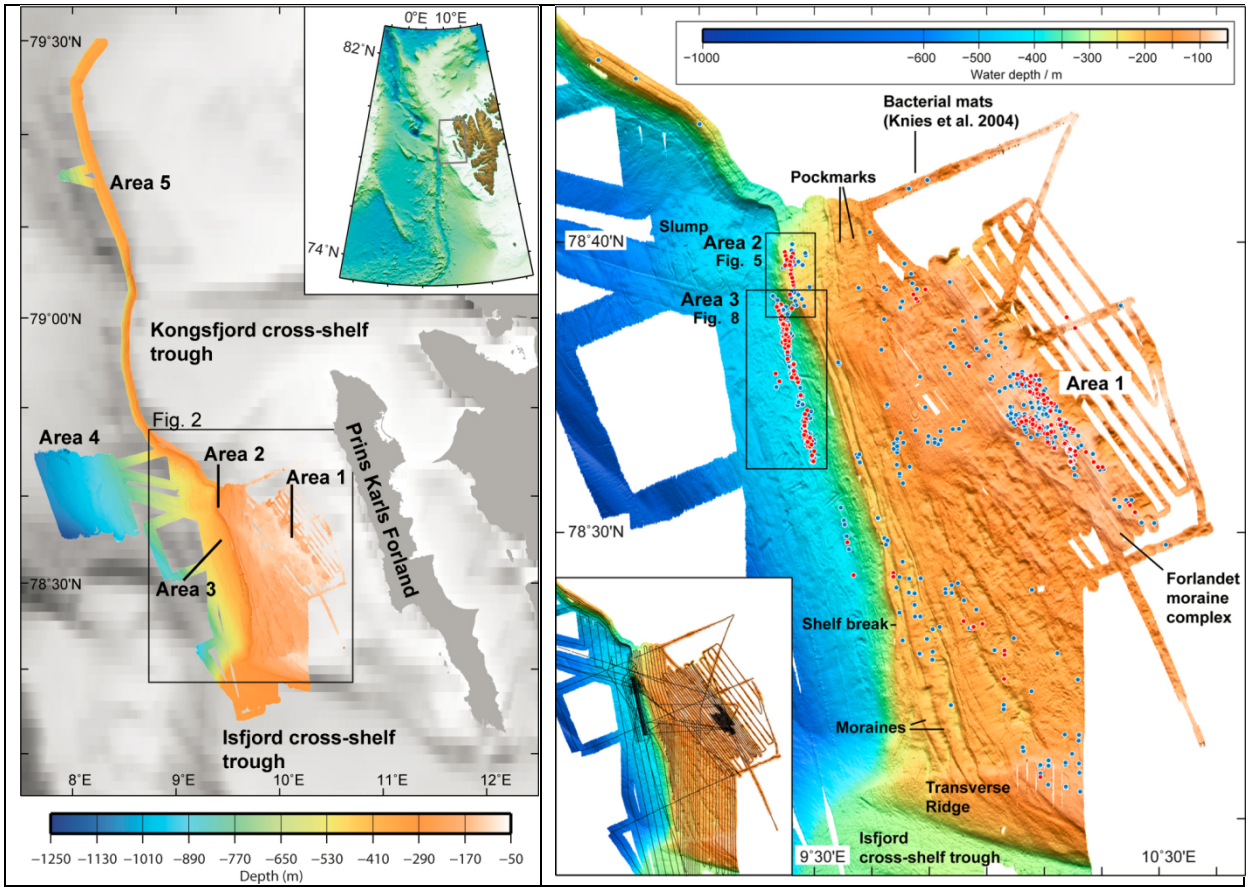

Fig. 6: Location of investigation by the R/V HEINCKE Cruise HE387 at Prins Karls Forland (left) and multibeam bathymetry and location of gas flares explored during summer 2012 as picked from EK 60 echosounder records separated in 3 regions (from Sahling et al. 2014).

A widespread investigation of gas emissions at the Prins Karls Forland margin and shelf was performed during R/V HEINCKE Cruise He387 in late summer 2012 (Fig. 6). Gas emissions were mapped, sampled, and quantified. Hydro-acoustic mapping revealed that gas emissions were not limited to a zone just above 396 m water depth and occurred widespread between about 80 and 415 m water depth, which indicates that hydrate dissociation might only be one of several sources for active hydrocarbon seepage in that area. Gas emissions were remarkably intensive at the main ridge of the Forlandet moraine complex in 80 to 90 m water depths, and may be related to thawing permafrost (Sahling et al. 2014).

Focused seafloor investigations were performed with a remotely operated vehicle (ROV). Geochemical analyses of gas bubbles sampled at about 240 m water depth as well as at the 396 m gas emission sites revealed that the vent gas is primarily composed of methane (> 99.70 %) of microbial origin (average $\delta^{13}C$ =−55.7‰ V-PDB). Estimates of the regional gas bubble flux from the seafloor to the water column in the area were achieved by combining flare mapping using multibeam and single-beam echosounder data, bubble stream mapping using the ROV-mounted horizontally looking sonar, and quantification of individual bubble streams using ROV imagery and bubble counting. The estimates by Sahling et al (2014) show that gas emissions at the margin west of Svalbard were in the same range of magnitude as bubble emissions at other geological settings. The quantification which forms a baseline for the year 2012, can be used to calibrate models predicting hydrate decomposition at present and in the future.

2.3 Objectives of the Cruise

The main objective of the HEINCKE cruise was to perform exploration along the continental margin of Spitsbergen and the Barents Sea for gas emission sites. The concentration of gas flares west of Prins Karls Forland seem to be an exceptional place for this type of geosphere-hydrosphere interaction and there might be more places of strong gas exchange. The improvements in acoustic methods in recent decades led to a significant advance in finding gas emissions by acoustic anomalies in the water column. However, compared to satellite-based investigation of land areas, sea-floor mapping is a time-consuming work that is highly dependent on good weather and the water depth. Systematic sonar surveys around Svalbard and in the Barents Sea are therefore fragmentary. Since R/V HEINCKE is well equipped with modern sonar systems to contribute to the incomplete knowledge about gas release from shallow subsea-floor and potential from dynamic changes in gas hydrate deposits. In addition to the mapping we performed investigations on methane distribution in the water column and the air to increase our knowledge about gas seepage in the area. Sediment sampling by gravity corer, minicorer and van Veen grab and measurements of pore water and gas composition should give us further indication for seepage –related processes.

Main questions have been: Are there more areas of strong gas release from the sea-floor? In which sediments or at which geological settings are gas emission sites existing? Can we confirm an exchange between seawater and air? Are there typical pattern of gas emissions and what about the composition of gases at gas vents from different areas around Svalbard?

3 Cruise Narrative (Gerhard Bohrmann)

Tuesday 25 August: R/V HEINCKE left the harbor of Tromsø on 08:00 exact time after three days berthing at Pier 24 located very close to the Tromsø University. The vessel came into the harbor on Saturday 22 August and change of the scientists and the loading happened on Monday 23 August. A track from Germany brought several boxes and equipment for the HE450 cruise and loaded equipment from the HE499 including a 20' Container to be transported back to Bremen. Embarkation of ten scientists took place for cruise HE450. Seven scientists from MARUM, Dr. Wei-Li Hong and Haoyi Yao from the Centre for Arctic Gas Hydrate, Environment and Climate (CAGE), UiT, Norway, and Marta Torres from College for Ocean, Atmosphere and Earth Science, Oregon State University, USA are the team for the next 14 days onboard. After the vessel started from the pier the safety officer introduced the new scientific crew to all safety rules onboard the ship. The vessel steamed through the fjords in northernmost direction and changed to a course towards west after free water was reached. The hydro-acoustic instruments of the ship started recording after we passed the 12 nm zone of Norway. After further 70 nm we reached the shelf break and followed the 450 m isobaths northwestwards (Fig. 7).

Wednesday 26 August: Mapping overnight along the 450 m isobaths northwestwards using EM710, EK64 and the SES 2000 guided the vessel to pass over the omega-shaped slide scar of Bjørnøyrenna slide where also the well-known Håkon Mosby mud volcano is located in a deeper level of the scar in 1270 m water depth to the west. There was hope to find some gas emission sites for further sea floor sampling at the edge of the extensive Barents Island Trough Mouth Fan, however, no indication of gas emission could be observed.

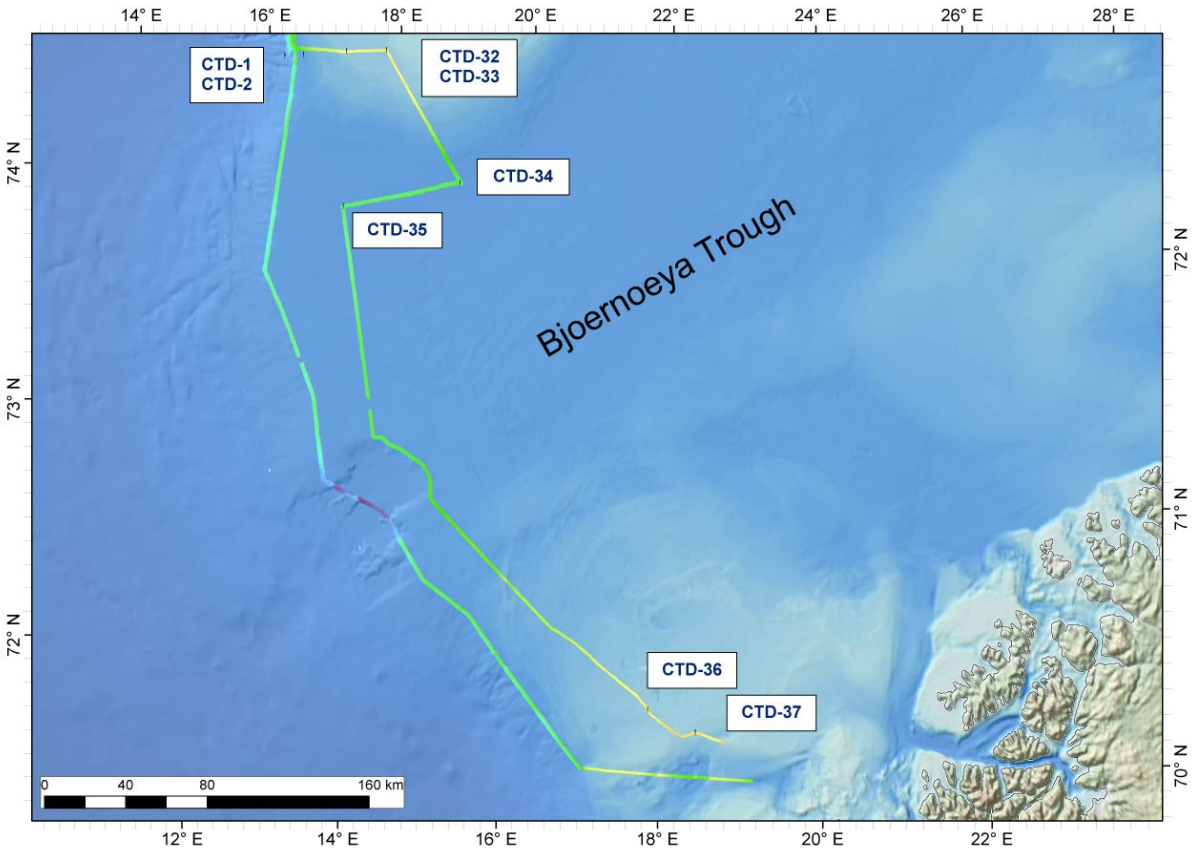

Fig. 7: Bathymetry lines and stations of Cruise HE450, southernmost part of three areas.

Thursday 27 August: At 74°10'N we deployed our first CTD in 353 m water depth and shortly after that a second CTD (CTD-2) in 690 m water depth to acquire methane profiles from the water column. The shallow CTD-profile showed higher methane values, which is contributed from the shelf to the water column. After the stations have been finished we continued in mapping along the upper continental slope and took an additional CTD station where a flare was observed. As expected the methane concentrations in the lower water column close to the sea floor showed elevated values between 40-50 nmol/L. Along the shelf edge at latitudes west of Bjørnøya Island several flares were observed during R/V HEINCKE Cruise HE449 and our cruise which guided us to perform several tracks parallel and perpendicular to the slope during the night.

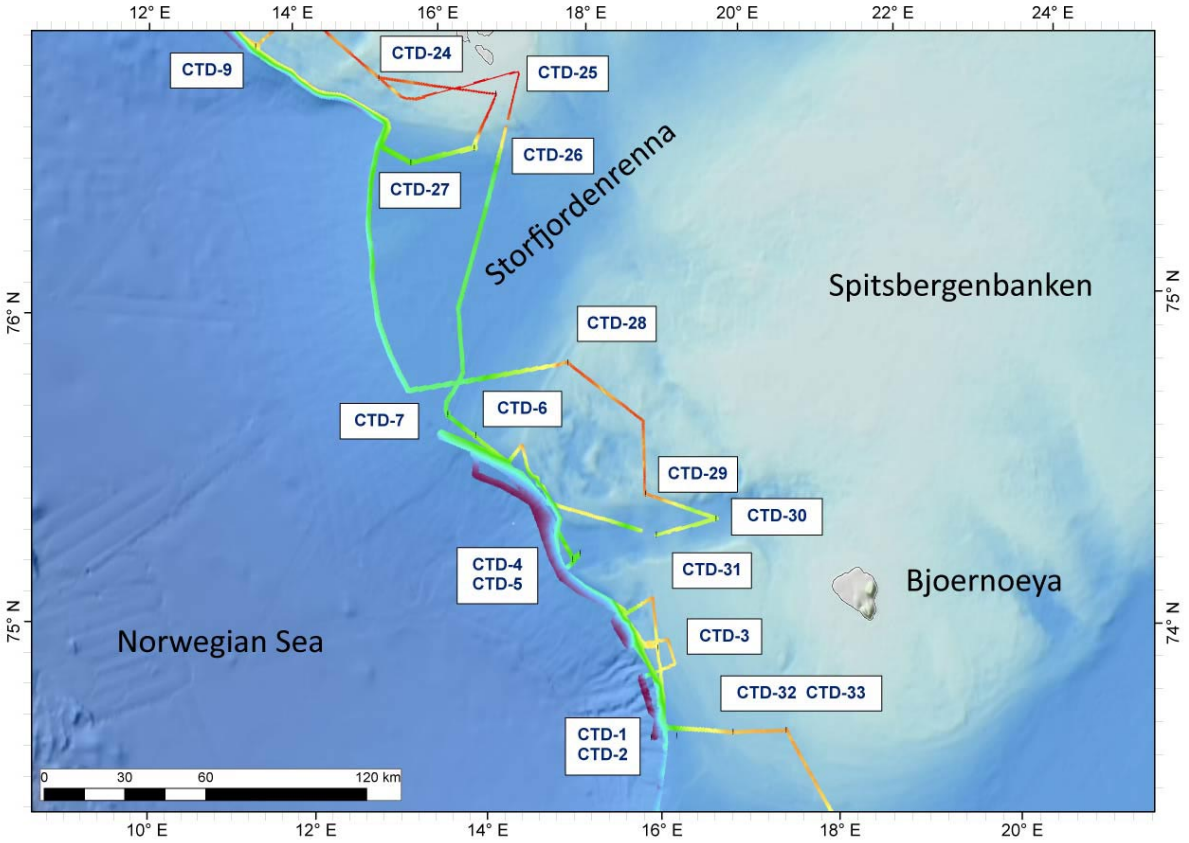

Fig. 8: Bathymetry lines and stations of Cruise HE450, middle part of three areas.

Friday 28 August: This night's survey showed no more flare positions and the weather became increasingly windy. At 08:00 we started CTD-4 and CTD-5 in the Kveithola Trough Mouth Area where we had flare indications in 360 m from a former cruise. Hydro-acoustic indications could not be seen this time and the water column sampling revealed only very little increased methane concentrations at the bottom of 15-20 nmol/L. During early morning we had Beaufort 6 which increased to lower Beaufort 7 (Fig. 9). A second pair of water column sampling (CTD-6 and CTD-7) was performed during the afternoon north of Kveithola Trough and showed even less enhanced methane values close to the surface. Following the weather forecast and the actual wind situation we decided to cross during sea-floor mapping the Storfjord to the north and reached an area close to the southernmost tip of Spitsbergen on the shelf.

Saturday 29 August: The course was probably too rough to find more gas emission sites using the acoustic systems of the ship, which changed on the shelf and immediately when we mapped with the ship on the shelf northwestwards flares have been observed. We followed a track covering several CTD stations at the Hornsund area where the highest methane concentrations have been measured during the cruise before (HE449). In comparison to the background values of 5 nmol/L in the upper water column stations at the Hornsund seeps and close by showed values of up to 15.6 nmol/L indicating most probably methane emission from the water to the atmosphere. We therefore recorded during the transect methane concentration in the air. CTD-8 was performed directly at the Hornsund seep to repeat a former measurement and CTD-9 sampled the shelf edge and added a seaward station to the Hornsund profil of HE449.

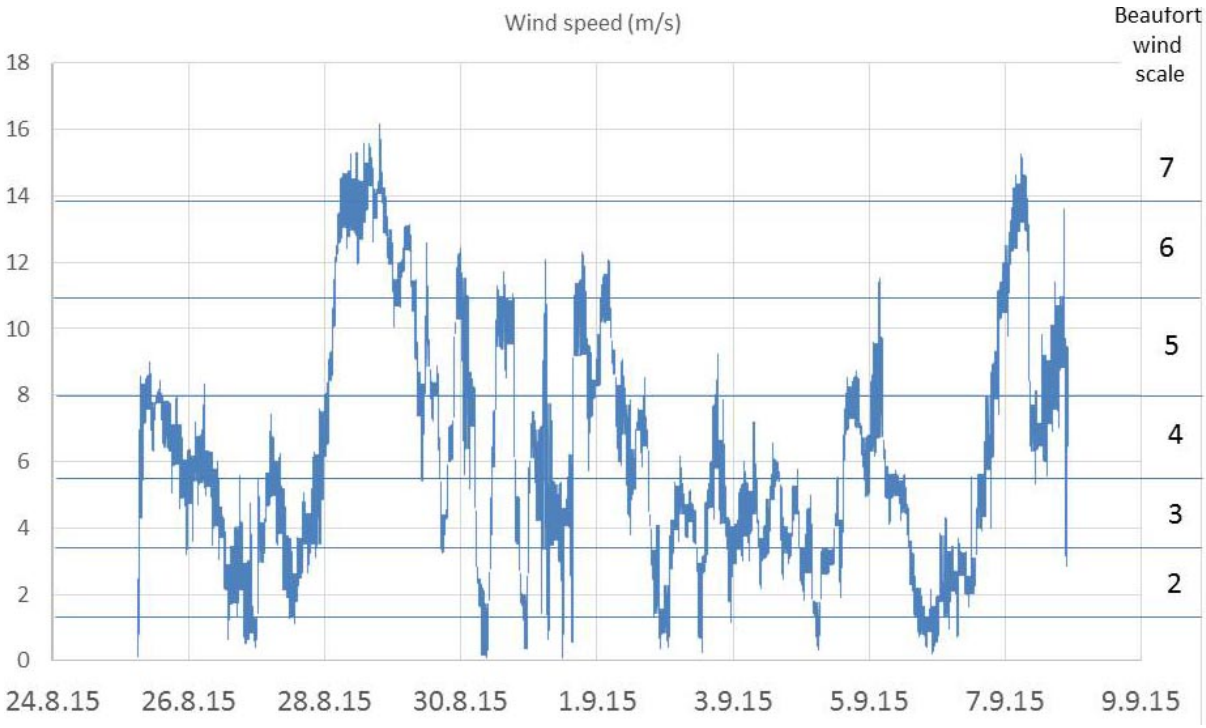

Fig. 9: Plot of wind speed during R/V HEINCKE Cruise HE450. Ten minutes values are plotted from the ship's meteorological data.

Sunday 30 August: Based on the weather forecast from the day before the exploration strategy was to perform mapping northwards over the Prins-Karls-Forland gas seeps (PCF-GS) in around 400 m water depth and to test whether Vestnesa Ridge can be reached under acceptable weather conditions. Sunday's weather forecast showed, however, too much wind over Vestnesa Ridge (Beaufort 6), so that we reject this plan and developed a plan for station work 40 nm southward. The mapping during the night showed some flares in an area in around 400 m water depth at the upper slope of Isfjordbanken Margin which became the new target. After having taken two CTD stations in the northern Isfjorden Trough Mouth Area, CTD-10 in 300 m water depth and CTD-11 in 660 m water depth, R/V HEINCKE steamed to the area where the new flares have been found in the night before. Unfortunately, the weather was too rough (Beaufort 6) to take a gravity core and we only took a grab sample for sampling the bottom sediment. A large portion of cm-sized pebbles were mixed with soft

sediment lumps which gave no hope for good gravity coring at that site. We extended the multibeam lines by five parallel lines parallel to the slope and we hoped that the processing of the data will give us more information for sampling when coming back to the area during the later cruise. The night's mapping course brought us along the Isfjorden Trough Mouth Fan to the north over the margin of PCF to the Kongsfjord.

Monday 31 August: Since the weather data showed strong winds in our potential sampling areas west and south of Spitsbergen we decided to search for gas emission sites in the wind-protected area of the Kongsfjord and Krossfjord, where no flares have been reported up to now. By moving with the ship to the east we found several flares and turned in front of the Kongsbreen glacier back to the west. Since there was space at pier of Ny Alesund beside an old sailing ship we decided to visit this northernmost settlement for two hours. We have been impressed by all of the town which is above all a research base of many nations mostly for atmospheric and climatic research and geophysics. We could visit the German Koldewey Station of the AWI and could take samples, which have to be transported back to Bremerhaven constantly cooled. After this unusual and unexpected break of the research work on the vessel we took CTD-12 at the deepest part of the Kongsfjord in 360 m water depth, during which we recorded a gas emission site close to the CTD-station (CTD-12) and took this site as a new location for a mini-corer (MIC-1) and gravity corer (GC-1). Both worked successfully and pore water and gas samples have been taken. The lithology of the 3.6 m long core was dominantly composed of silty clay, partly laminated in the upper part. Dropstones of various size and composition have been intercalated and dominate the lithology in few horizons.

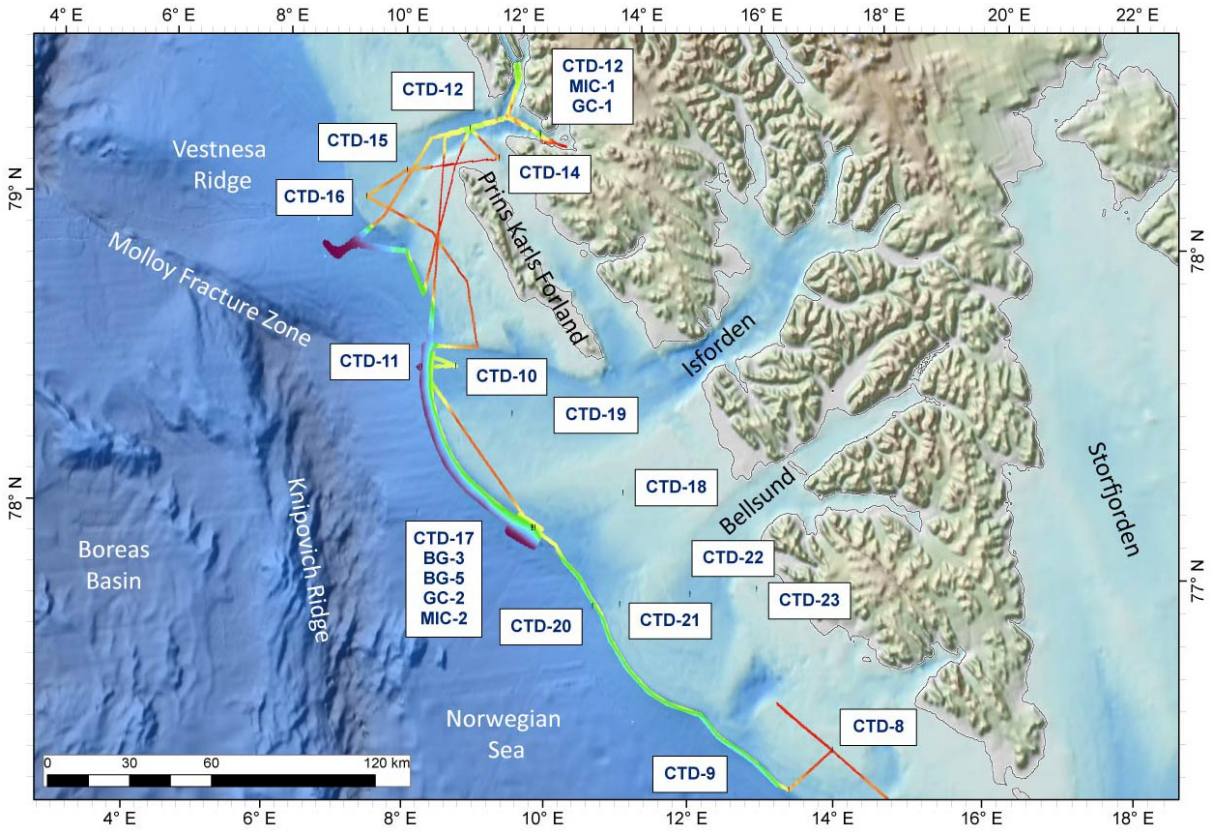

Fig. 10: Bathymetry lines and stations of Cruise HE450, northernmost and main area of three regions.

Some mapping tracks were performed within the Krossfjord, where no methane bubbles have been recorded in the water column. The second half of the day was very sunny until late evening and showed us wonderful insight into the glacial landscape and the geology surrounding the fjords.

Tuesday 1 September: During the night's mapping on the way to Vestnesa Ridge we recognized that the weather became too bad for taking sediment cores. Three cores in and between well-known pockmarks on the ridge were planned to sample gas hydrates, however, this program was rejected. We decided to work closer to Prins Karls Forland where the wind speed was less. A NW/SE profile along the 400 m isobath covered the dense gas emission sites described by Westbrook et al. (2009). In order to finalize the water measurements for methane in our northernmost area, we decided to perform 4 CTDs along a line within the Kongsfjord cross-shelf trough. CTD-14 of that profile was placed in Forland Sund to document the contribution of methane from this broad passage, between mainland Spitsbergen and the Prins Carls Forland. The westernmost CTD of the profile (CTD-16) was placed in the Kongsfjord Trough Mouth area. The following hydro-acoustic mapping we took over the Forlandet moraine complex where many gas emission sites in about 85 m water depth have been found during Cruise HE-387. Gas emission sites have been very active as before and could be recorded by EK60 as well as by EM710 sonars. The ship moved afterwards to the west and followed the margin at around the 500 m isobath and added an additional line in the deeper slope to extend the multibeam map of that part of the margin.

Wednesday 2 September: In the morning we reached at 08:00 the area at the margin in 390 m water depth where several flares have been observed some days before when we headed to the north. We started to take 3 grabs to test the sediment composition at various positions and had to recognize, that pebbles of various diameters up to fist-size were to be found on the seafloor location. Since the ship could use the online acoustic image of a flare for navigation we took a gravity corer and sampled just some meters beside a bubbling area. The sediment core of 1.90 m recovery was well preserved, however, gas hydrate was not sampled. Unfortunately the winch stopped 2 times and the wire which came between some rolls loosened and formed several loops. Since this operation was too dangerous, the decision came to the point that the gravity corer should not be used anymore during this cruise. Unfortunately, this was a serious consequence for our cruise because gas hydrates could not be sampled anymore. After the core we took a CTD-station close by, moved to the gravity core position again and sampled a minicorer (MIC-02). Two more CTD stations (CTD-18 and CTD-19) were taken in 100 m WD at the inner part of the shelf and in 218 m WD at the center of the Isfjorden Trough Mouth. Mapping for the night started from the last CTD station westwards and along the margin partly with 3 lines parallel to the margin.

Thursday 3 September: After a long mapping night a series of CTD stations started from the deepest station at the margin with 500 m water column (CTD-20) over the outer shelf (CTD-21 in 200 m water depth) to the inner shelf (CTD-22 in 170 m water depth) and close to the Bellesund Banken (CTD-23 in 90 m water depth). From CTD-23 station the hydro-acoustic mapping started over the shelf back to the margin, where first a line northwestwards along the shelf break of the Bellesund Trough Mouth Fan was performed. Further mapping guided the ship southeastwards back along a line at the upper slope. Today's weather was very calm so that the ship's speed of 10 knots could be used all the time.

Friday 4 September: In the morning the sea surface was completely flat, showing no waves at all. The only waves were made by the ship itself which makes hydro-acoustic mapping very productive and we could continue in mapping with a speed of 10 knots. In the morning the ship left the margin and

steamed over the outer shelf including the Hornsund gas seeps for measurements of methane in the air. This transect on the shelf parallel to the margin was made on Friday 28 September when the ship steamed in the opposite direction during high wind speed Beaufort 5 to 6 and higher methane concentrations have been measured in the air. The repetition of the measurements today under very calm sea state conditions should show the potential influence of the wind-induced waves on the methane concentrations in the air. Immediately when we steamed over the Hornsund gas seeps we recognized the well pronounced gas flares in the water column. At the end of the line we run CTD-24 in 175 m water depth. At the southern tip of Spitsbergen another CTD was performed in 50 m water depth. Two more CTD stations followed in the afternoon, CTD-26 and CTD-27. Both stations represent locations on the Storfjord Trough Mouth in deeper water of 370 m and 330 m. Mapping in the evening and night followed along the margin off the Hornsundbanken and to the south along the northern part of the Storfjord Trough Mouth Fan.

Saturday 5 September: During early morning we crossed the Storfjord Mouth Fan to its southeastern rim and took CTD station 28. Further three CTD stations CTD-29, CTD-30 and CTD-31, were performed north and within the Kveithola cross shelf trough during the day. The mapping in the evening brought us first along the shelf break to the north were we stopped at night before mapping.

Sunday 6 September: At very early morning on the way back we crossed to the south the Kveithola in the trough mouth area and have run the first CTD (CTD-32) around 40 nautical miles to the south and steamed 10 nm to the east for taking CTD-33. The weather was very calm and allowed sight to far distance. We could have a wonderful view to the Island of Bjørnøya around 30 nm away. The sea surface was extremely flat and we could observe a group of whales with their fountains, coming closer during steaming of the vessel. Before we took the further two CTD stations (CTD-34 and CTD-35) we had to steam 30 nm to the south and immediately after the last station we started the mapping to the south over the Barents Sea Trough in direction to the Barents.

Monday 7 September: Sea floor mapping became difficult because of the sea state. The sea surface became rough during wind speed of Beaufort 6 and 7. We had to cancel the first two CTD stations of the day because of high waves. We also had to shorten the track on the way to the south. During afternoon the sea state became more calm, so that we could perform the last two stations of the cruise CTD-36 and CTD-37. In the evening we reached the border of our research area and we stopped recording the sonar systems.

Tuesday 8 September: R/V HEINCKE reached the fjord systems in northern Norway, which form the passage to Tromsø. The ship entered the harbor of Tromsø in the morning and berthed at 08:00 at the same place pier 24, where we started exactly 14 days ago. The ship steamed 2,516 nm and we mapped about 2,400 nm using multibeam EM710, fish finder EK60, and subbottom profiler SES2000. We took 37 CTD stations, 5 grab samples, 2 gravity corer and 2 minicorer stations. R/V HEINCKE Cruise HE450 was a successful cruise.

4. Hydroacoustic Work (Paul Wintersteller, Christian Ferreira, Chieh Wei Hsu, Markus Loher)

During the HE450 several acoustic devices were used to map the water column, seafloor surface morphology and sub-bottom sediment layers. All georeferenced data are based on a geographic

coordinate system (WGS84) and large overview maps are displayed in a projected coordinate system (Polar Stereographic). For small scale maps a UTM projection (ETRS 1989 UTM Zone 32N) was used.

4.1 Multibeam Echosounder EM710

4.1.1 System Setup

The Kongsberg EM710 is a shallow to mid-water Multibeam Echosounder (MBES) operating between 70 and 100 kHz and optimal depth range from 10 to 1200 meters. With a transducer configuration of 1 by 2 degrees (TX/RX) this system has 200 beams, 400 soundings in the used high density mode, which allowed us to measure both bathymetry and backscatter. The Water Column Data (WCD) were recorded to detect and analyze gas seepage sites.

The system was operated with a maximum swath angle of 120 degrees except of Survey 9 to 11 where swath width was set to 130° in automatic ping mode. Between the surveys CTDs were conducted to calculate Sound Velocity Profiles (SVP) that were inserted in the acquisition software Seafloor Information System (SIS) version 4.1.2 (from October 2013). The Surface Sound Velocity (SSV) was measured by the C-Keel sensor, which is a very important parameter because it is used to calculate the initial direction of the beams transmitted/received. The logging of the data was set to generate a new file every 10 minutes with the water column in a separate file. The filter settings used were “Spike Filter Strength” as STRONG, “Range Gate” as SMALL, “Phase ramp” as NORMAL, “Penetration Filter Strength” as WEAK, and the activated additional filters were: “Slope”, “Aeration”, “Sector Tracking” and “Interference”. Roll, Pitch and Yaw corrections were active during the whole cruise.

During the surveys the EM710 experienced a few crashes (acquisition software and/or processing unit) but was otherwise stable nearly the whole cruise. The C-Keel sensor worked flawless until about half of the cruise and then stopped working for a few days. In fact it had several issues delivering data during the cruise. Cleaning and maintenance were done by the chief engineer on September 4. The probe seems to work reliable since then.

In total were surveyed 4346.84 kilometers with an average speed of 7.52 knots during 312.23 hours generating 1856 files. The overview map shows the total coverage of the HE450 MBES data.

4.1.2 Processing of the Water Column Data (WCD)

A key aim of HE450 was the investigation of active gas emission sites on the seafloor where gas bubbles can be hydroacoustically detected in the watercolumn. For this purpose the watercolumn data generated by the EM710 as well as the signal from the EK60 were monitored constantly and the occurrences of flares were noted in a GIS software (Global Mapper) “on the fly”.

Storage of the watercolumn data (.wcd files) allowed post-analyses of detailed flare occurrences (flare picking) in FM Midwater and FM Fledermaus . The picked flare source-points were then imported in Global Mapper and served as sites of interest for further hydroacoustic surveys, sediment sampling or CTDs.

4.2.1 System Setup

The hull-mounted split beam echosounder KONGSBERG EK60 was utilized to aid discovering seep sites with gas emission during the cruise. To avoid further interferences just the 38kHz transducer ES38B, with 7 degrees beam angle was activated. The split beam principle is used to find the position of individual targets in the transducer beam, compensate for the beam pattern and calculate corrected target strength values. In total 4 out of up to 7 possible split beam transducers are installed on RV Heincke. There frequencies are 38, 70, 120 and 200 kHz. According to the description the 38kHz transducer is able to observe single fish down to 1000m water depth. Due to large distances and other main purposes the survey speed during this cruise was mostly around 8-10kn. Therefor the 38 kHz single beam echosounder has clear advantages in along-track-resolution compared to the multibeam echosounder EM710. The ping rate of the single beam sounder is higher since the 2-way travel times are short at nadir

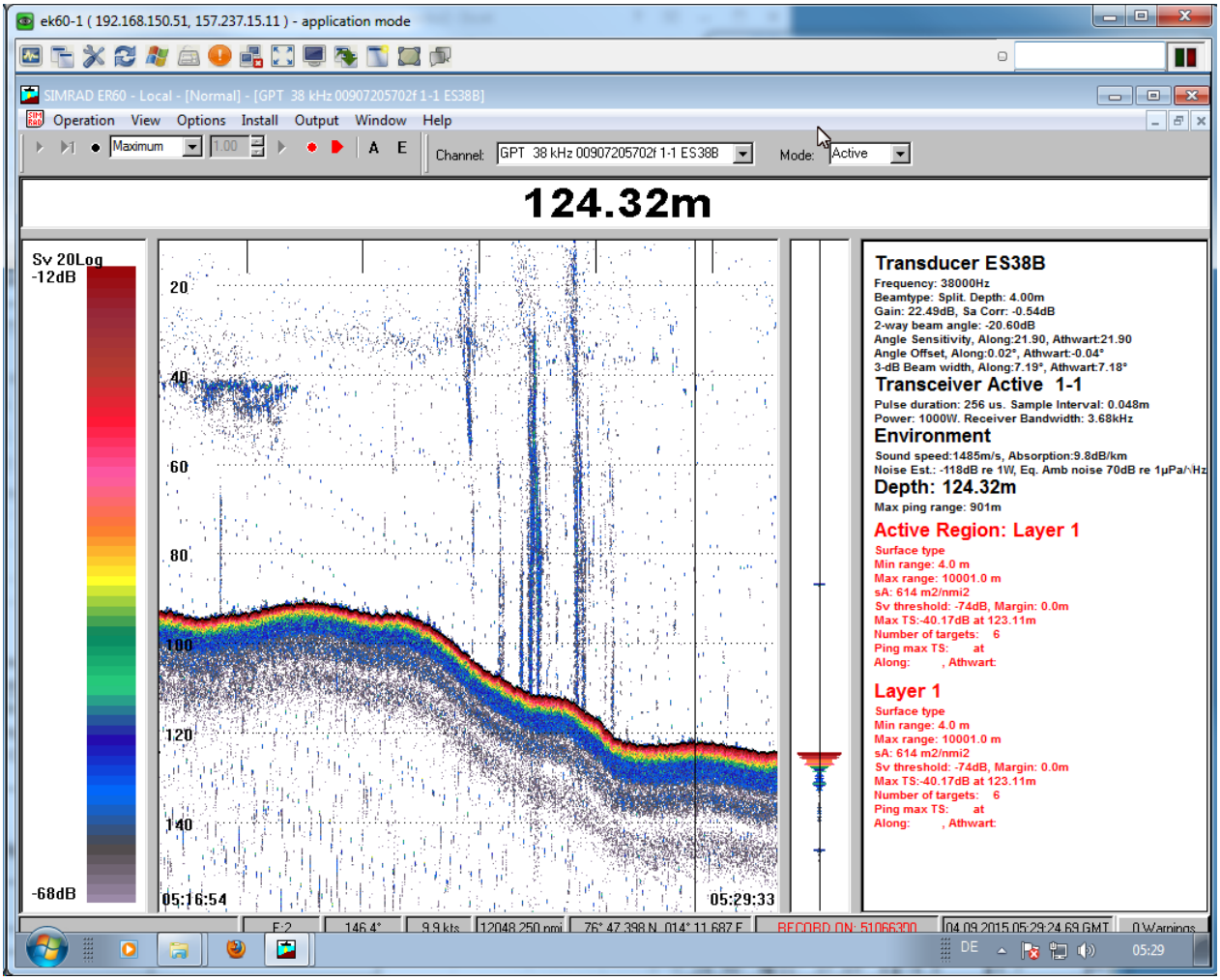

Fig. 11: Screenshot of along-track gas flares in the water column at about 115m WD.

4.3 Parametric Subbottom Echosounder SES2000 (Paul Wintersteller, Markus Loher)

4.3.1 System Setup

The SES2000 medium is a sub-bottom profiler that utilizes the parametric effect based on the non-linear relation of pressure and density during sonar propagation. A primary high frequency (HF) wave (of about 100 kHz) is used to create a secondary low (about 6 kHz) frequency (LF). Throughout the cruise the SES200 was continuously recording and no problems were encountered.

The SES2000 is used to study subsurface structures (different sedimentological units, tectonic structures), to recognize gas charged sediments (blanking zones) as well as to investigate particular seafloor morphologies (pockmarks, sediment waves, glacial deposits) in detail.

Settings during HE450

Transmit:

LF Frequency:	6 kHz
LF Pulses:	1
LF & HF:	Auto Gain Control
HF Signal Damping:	ON

Processing:

Soft TVG:	0.5 dB/m
Median Filter:	ON
Normalize Gain	
Reduce Noise	

Range:

Default:	A range of 100 m was recorded for most of the cruise.
Auto Range Start:	ON
Use of LF-Waterdepth:	ON

Threshold:

LF Mode:	Logarithmic with: Min Level = 1; SRange = 4
HF Mode:	Logarithmic with: Min Level = 4; SRange = 8

Depth:

Detection Sensitivity LF:	40 %
Detection Sensitivity HF:	40 %
Draw LF WD-Line:	ON

4.3.2 Data Analysis

The online view of the SES2000 displayed the LF and HF signal in different panels (s. Fig. xyz). Due to the automatic seafloor detection, data was always displayed over a range of 100 m and automatically adjusted when changes in the water depth occurred. The data output was stored as ".ses" and ".raw" files and could be replayed in the ISE software, available onboard.

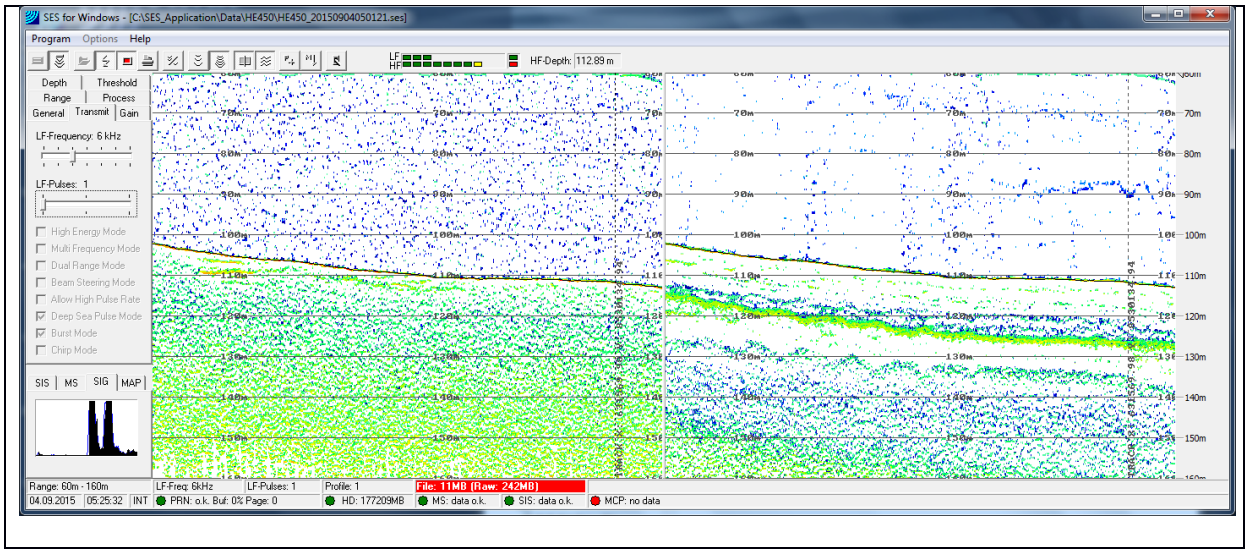

Fig. 12: Online screenshot of the SES2000 (31/09/2015 at 05:26). The low-frequency (LF) panel on the left shows deeper penetration but lower resolution compared to the high-frequency (HF) on the right. In the HF panel, gas plumes are visible as faint anomalies trending vertically in the watercolumn

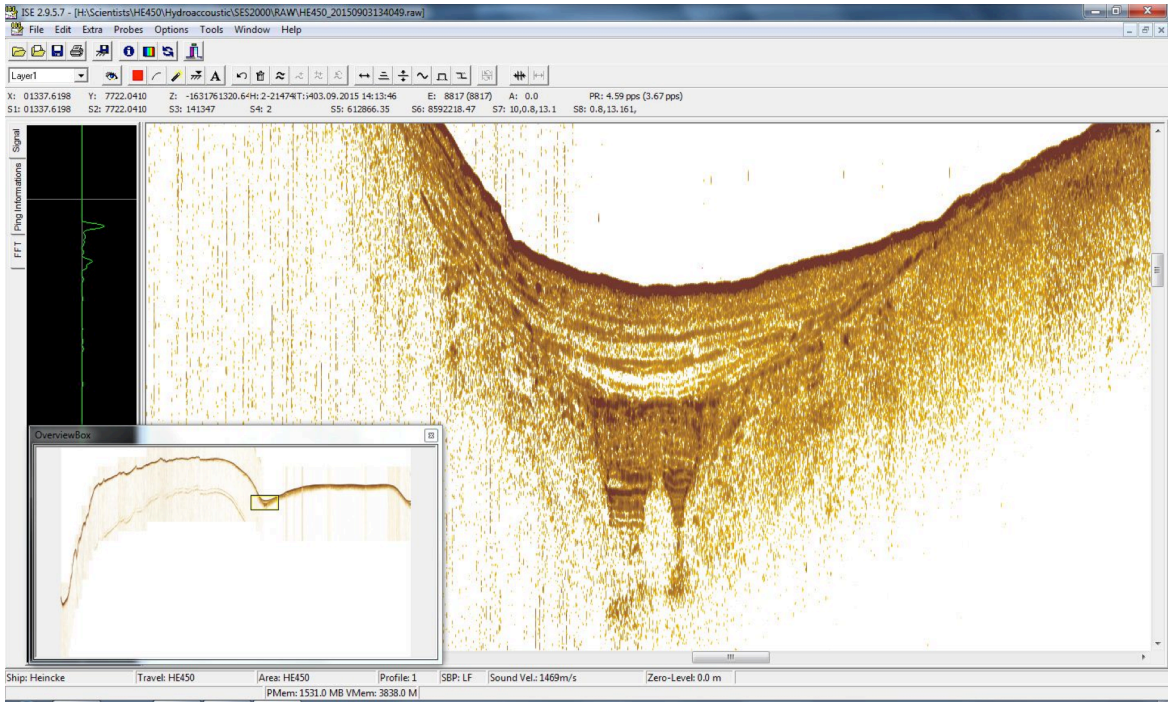

Fig. 13: Screenshot of the ISE software where the SES2000 sub-bottom data is replayed and post-

5. Water Column Work and Air Sampling Program (Marta Torres, Thomas Pape, Mirko Lange)

5.1 Introduction

There is a growing body of data documenting that the continental margin west of Svalbard is prone to hydrocarbon seepage. The presence of gas hydrates (below ~600 m water depth) and free gas below the base of the gas hydrate stability zone is indicated by the presence of a bottom simulating reflector (Vanneste et al., 2005; Westbrook et al., 2009; Chabert et al., 2011). Gas emissions concentrated along a band at seafloor depths just above the 396-m isobath have been attributed to temperature induced gas hydrate dissociation in response to a warming trend of the bottom water of 1°C over the past 30 years (Westbrook et al., 2009). In addition to these well studied seeps on the Svalbard slope, gas-related seismic facies have also been observed on the upper slope and outer shelf (Sarkar et al., 2012; Rajan et al., 2012) and gas discharge has been mapped on outer shelf at water depths up to 150 m (Westbrook et al., 2009). Additional evidence for seepage on the shelf was provided by elevated bottom-water methane concentrations and the stable carbon isotope composition of methane in the water column (Damm et al., 2005; Gentz et al., 2013), as well as by remotely operated vehicle (ROV) observations of widespread occurrence of methane bubbling sites between about 80 and 415 mbsl (Sahling et al., 2014). These authors show that gas emissions are remarkably intensive at the main ridge of the Forlandet moraine complex, and they postulate that they may be related to thawing permafrost.

Because of the warming potential of methane, there have been long-standing efforts to quantify how much of the methane discharged at seafloor seeps reaches the atmosphere. In addition, it is important to quantify the amount of methane that remains in the ocean, as aerobic microbial oxidation of methane releases protons and thus may play a role in ocean acidification (Biastoch et al., 2011). There is therefore, a significant interest to understand the interactions among ice, ocean, microbiology and climate and their sensitivity to both natural and anthropogenic change in Arctic regions. The hydrographic objectives of HE450 were to quantify the relative roles of various sources of methane offshore Svalbard, and extend the study to include the less studied region along the shelf from 71^{o} to 76^{o}N.

The sampling was guided by hydroacoustic observation of flare sites as well as previous data of methane seepage in the area (Sahling et al., 2014; Mau, 2015). Samples were analyzed for their methane concentration onboard, which guided the sampling strategy as the expedition progressed. Additional selected samples were collected for characterization of isotopic composition of methane-carbon and water-oxygen, as well as nutrients and barium. The isotopic composition of methane is used to identify the methane sources (biogenic vs. thermogenic); and in addition, these data may provide information on the degree of methane oxidation. The $\delta^{18}O$ of ocean water is a conservative tracer and meteoric water in high latitudes is highly depleted in ^{18}O, therefore this parameter aids in quantifying the degree of mixing of glacier water and river run-off with ocean water.

5.2 Methods

5.2.1 Water sampling

Hydrocasts were carried out using the ship-based SBE911plus (Sea-Bird Electronics, Inc.) CTD, which is comprised of two conductivity (SBE 4c) and temperature (SBE3 plus) sensors and one pressure

sensor. The system was additionally equipped with dissolved oxygen (DO, SBE 43), fluorometer (WET Labs, Eco FL) and transmissometer (WET Labs, C-Star) probes. The underwater unit was attached to a SBE 32 carousel water sampler with 11x4L water sampling bottles (OceanTest Inc.), which were closed at selected depths during the upcast. The CTD/rosette system was lowered with 0.5 m s^{-1} in the upper to intermediate water column and 0.2 m s^{-1} in bottom waters, whereas heaving in-between the bottle firing procedure was conducted with 0.3 to 0.5 m s^{-1}.

5.2.2 Methane analyses in water samples

For analyses of methane in the water column we used the procedure described by Gepraegs et al. (2015), based on headspace extraction and analyses using off-axis integrated output spectroscopy (ICOS). Water samples from the Niskin bottles were collected in three 140 ml syringes outfitted with a valve. The syringes were flushed and filled with 100 ml of water, with no air bubbles. Two of the syringes were used for the analysis and one served as a spare. After equilibration of the samples to room temperature, 40 ml of Zero Air (synthetic air without methane) were added to the syringes, which were then shaken for 1.5 min. The 80 ml of headspace gas were collected in another syringe and injected into the Los Gatos research Greenhouse Gas Analyzer (GGA, followed by dilution with 60 ml of Zero Air to reach the 140 ml of gas in the chamber required for the instrument to operate.

5.2.3 Methane analyses in air

We took advantage of the GGA capability to measure air samples using a continuous flow mode. Air was collected from an intake located 5 meters above the sea surface and monitored using the slow mode at frequencies of either 10 or 100 seconds. The continuous monitoring was only conducted when weather conditions allowed and when the instrument was not being used for water sample analyses.

5.2.4 Extraction of dissolved gas from water samples

For preparation of dissolved gas for subsequent analysis (e.g. δ13C-CH4), 600 to 800 mL of selected water samples were transferred from the Niskin bottles into pre-evacuated 1 L gas tight glass bottles. The dissolved gas was prepared from the water samples by high-grade vacuum extraction (Lammers & Suess, 1994; Rehder et al., 1999; Schmitt et al., 1991) within a few hours of collection. The liberated gas was taken from the extraction system via a septum with gas-tight syringes and transferred into 20 ml serum glass vials pre-filled with saturated NaCl solution for storage and onshore analysis. In total, 113 gas samples were prepared from water samples collected during 28 CTD stations.

5.3 Results

5.3.1 Water masses in the study area

We used the water mass classification of Slubowska-Wodengen et al. (2007) and the CTD data from 37 vertical profiles collected along the HE450 survey to map the prevailing oceanographic conditions.

In the surface layer, we observe the presence of two distinct water masses (Figure 13). South of 75.5°N, the surface water is characterized by low salinity (34.7<S<34.9) and warm temperatures (5 to 10°C), which corresponds to Arctic Surface Water. Farther north along the Spitsbergen shelf, we observe a mixture of water masses that include the West Spitsbergen current (WSC) flows along the

shelf break carrying Atlantic Water (T>2C and S>35) and a component of fresh Polar Water (PW), with low salinity (S<34.4) and colder temperatures (T<4°C), which is clearly distinct in the TS diagrams. Various mixtures of these surface water masses result in complex and variable TS diagrams. Underneath the surface fresh water pool the Atlantic Water (AW) is characterized by S>34.90 and T>3°C. The deepest water sampled, with S>34.9 and T<3°C corresponds to the Lower Arctic Intermediate Water (Slubowska-Wodengen et al., 2007).

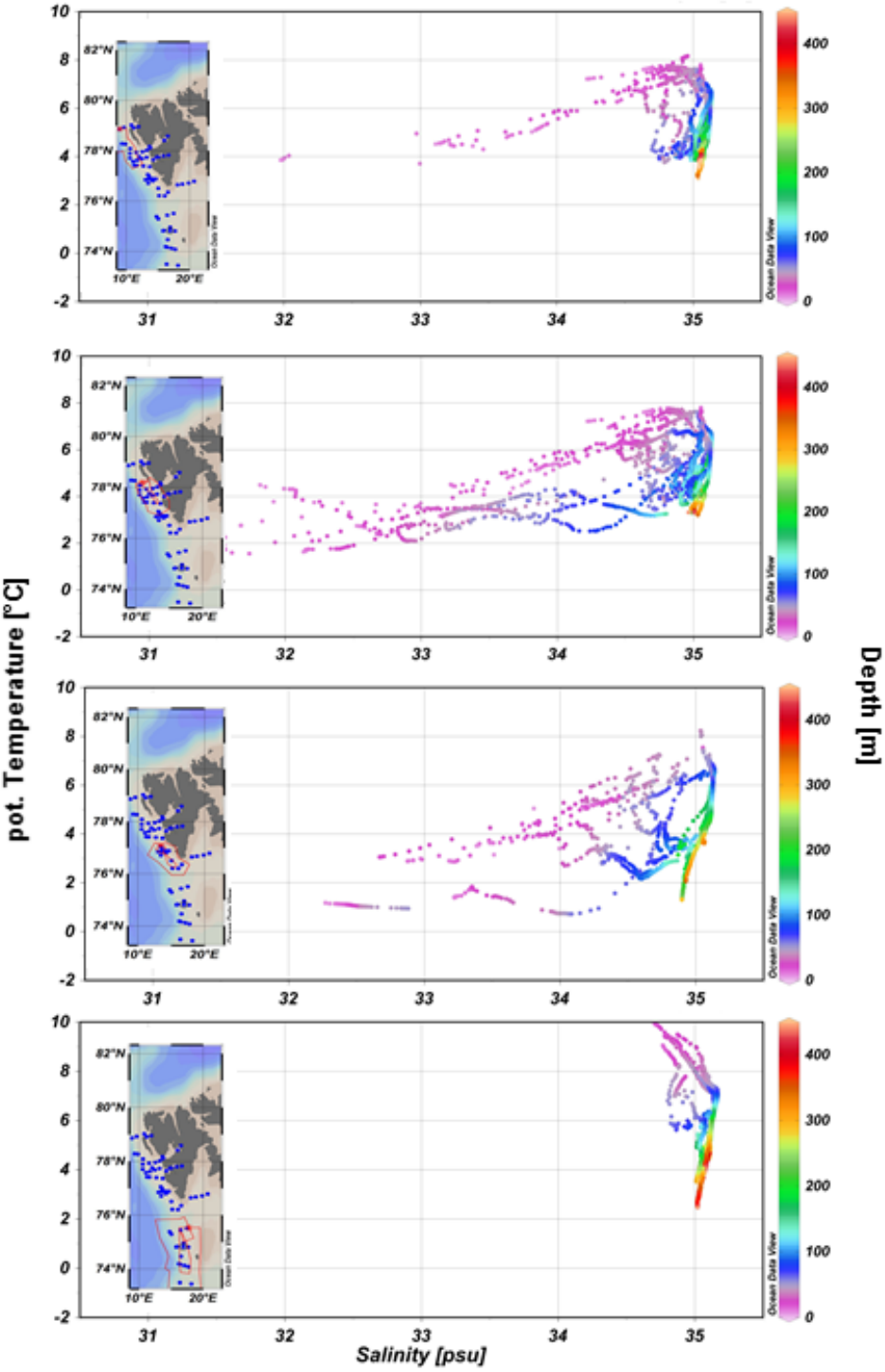

Fig. 13: TS diagrams of the study area. A) Barents sea shelf/slope. B) Spitsbergen outer shelf. C) Spitsbergen inner shelf. D) Hornsund area.

5.3.2 Methane in the water column

The methane concentration in the 37 hydrocasts conducted during this cruise is illustrated in Figs. 14 to XX. We divide the stations in three general areas: Area 1, along the Barents shelf and slope (71° to 76°N); Area 2, Spitsbergen shelf and slope (76° to 79°N); and Area 3, Kongsfjorden.

Area 1. Barents Sea shelf (Figure 14)

Water profiles for samples collected from 71° to 77°N are shown in Fig. 14. From these hydrocasts, only CTD-3 was located directly over a flare area; CTD-29 was taken over a region of previously reported flares. These stations revealed concentrations in bottom water up to 50 nmol/l. In the other stations collected in water depths above 300 m in areas of no flare activity, we document elevated methane to maximum values of ~20 nmol/l. These results, tied to the observations of several flares in the area, indicate the presence of significant methane release in the sediments from several and perhaps abundant sites of micro-seepages distributed along the Barents shelf.

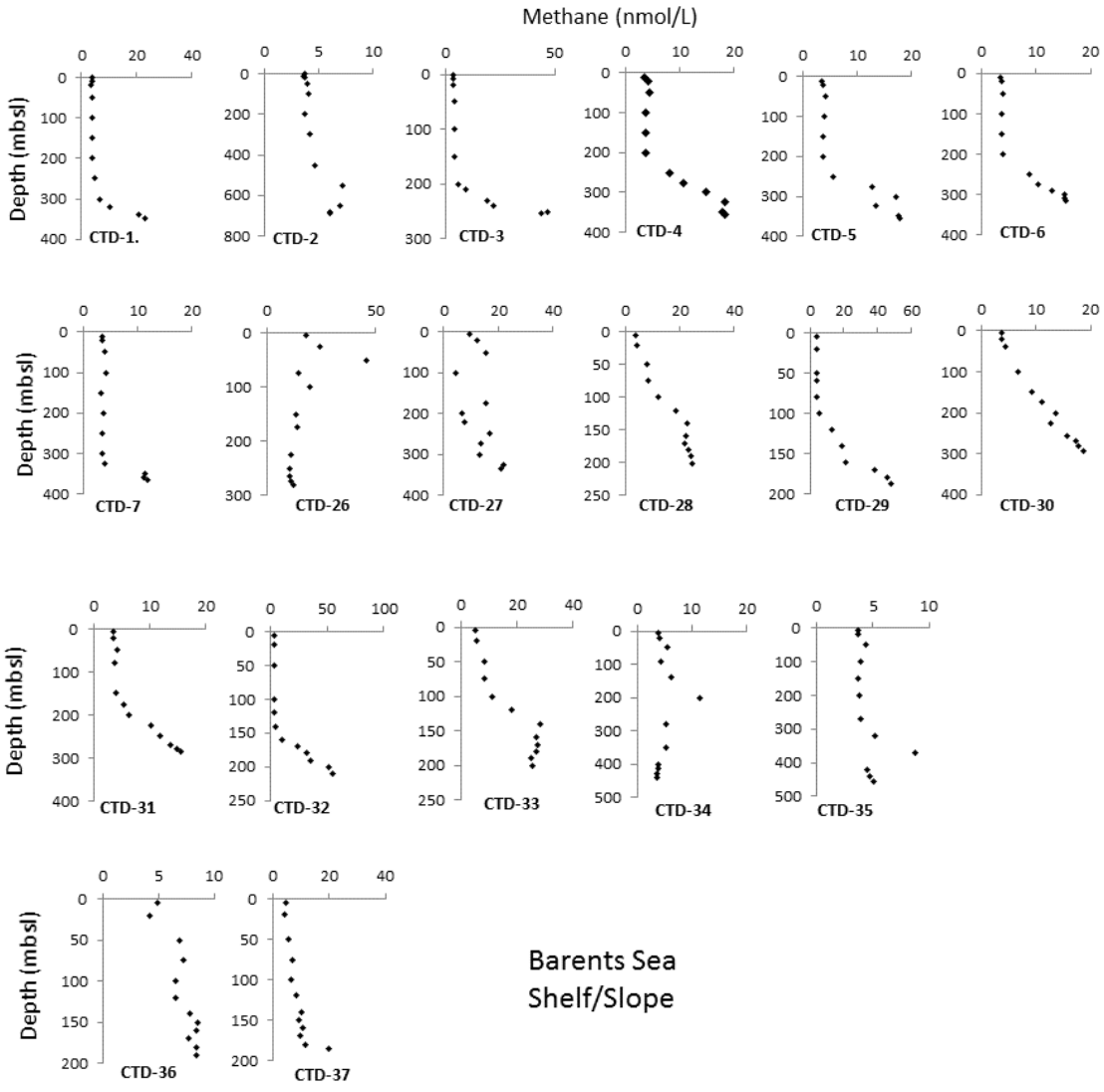

Fig. 14: Methane concentration profiles for stations along the Barents Sea shelf/slope (Area 1), for station locations see Figure 10.

There is a marked concentration gradient between deep and surface waters, which is created by density stratification of the water masses. The elevated methane values are only found beneath water with σ_θ>27.75, in what is commonly referred to as transport along a pycnocline (Cynar and Yayanos, 1992). All values in shallow waters south of 76°N show background concentrations of <5nmol/l. The northernmost stations in the transect (CTD 26 and CTD 27), however show enrichment in surface waters to values of 18 and 9 nmol/l, respectively, consistent with other observations along the Spitsbergen shelf (section below) and reports of Mau (2015).

It is worth noting that CTD-1, collected at 700 m water depth, only 7 km due west of station CTD-2, does not show the methane increase at depth observed in all stations along the shelf. The lack of horizontal extension of the methane plume is consistent with previous observations along Spitsbergen that document methane incorporated into bottom waters as it spreads northwards below the 27.75 pycnocline along the shelf and upper slope (Damm et al., 2005). The elevated methane values in the bottom water can be traced northwards along the Spitsbergen shelf and slope to Prins Karls Forland, as discussed in the section below.

Area 2, Spitsbergen shelf and slope region (Figure 15)

As shown in the surveys during HE459 (Mau, 2015), there is intense flare activity and associated high levels of dissolved methane in the bottom waters of the shallow Spitsbergen shelf. The methane concentrations in the hydrocast stations collected along the inner shelf, all indicate bottom water enrichment, which at station CTD-8 reached values as high as 339 nmol/L. Some of these stations also have elevated values in near surface waters, ranging from 8 to 14 nmol/L, indicating that the Spitsbergen shelf may act as a methane source to the atmosphere.

The water column sampled north of Prins Karls Forland is characterized by the presence of two mid water maxima at ~70 and ~150 meters water depth. The 150 m mid-water maximum peak was observed in both stations CTD-13 and CTD 14, but more pronounced in CTD-13, with a maximum of 60 nmol/L. This likely corresponds to a methane plume originating at the mouth of Kongsfjorden, where intense flare activity was observed. The shallower mid-water maximum in CTD-15, with a methane content of 70 nmol/L at 50 m, likely reflects northwards transport of the shallow seeps off Prins Karls Forland (Sahling et al., 2014), which are located around 80 meters water depth. At station CTD-16, there is still a distinct increase above background between 75 and 100 m, but the methane concentration is only 8 to 9 nmol/L. At this station there is also a slight increase towards depth, with a maximum of 17 nmol/L at 216 m water depth; which may reflect northwards transport of methane from the 200 m water depth seeps described by Sahling et al., (2014).

Area 3, Kongsfjorden (Figure 16)

Only one CTD was collected within the fjord (CTD-12). The station was selected to sample the deepest waters of the fjord. At the onset of the hydrocast, there were no indications of flare activity at this location; however a flare was observed to appear during the hydrocast at ~150 m from our sampling location. Methane concentrations in this station are above 10 nmol/l throughout the water column, with a mid-water maximum of 20 nmol/l at 100 mbsl (Fig. 16).

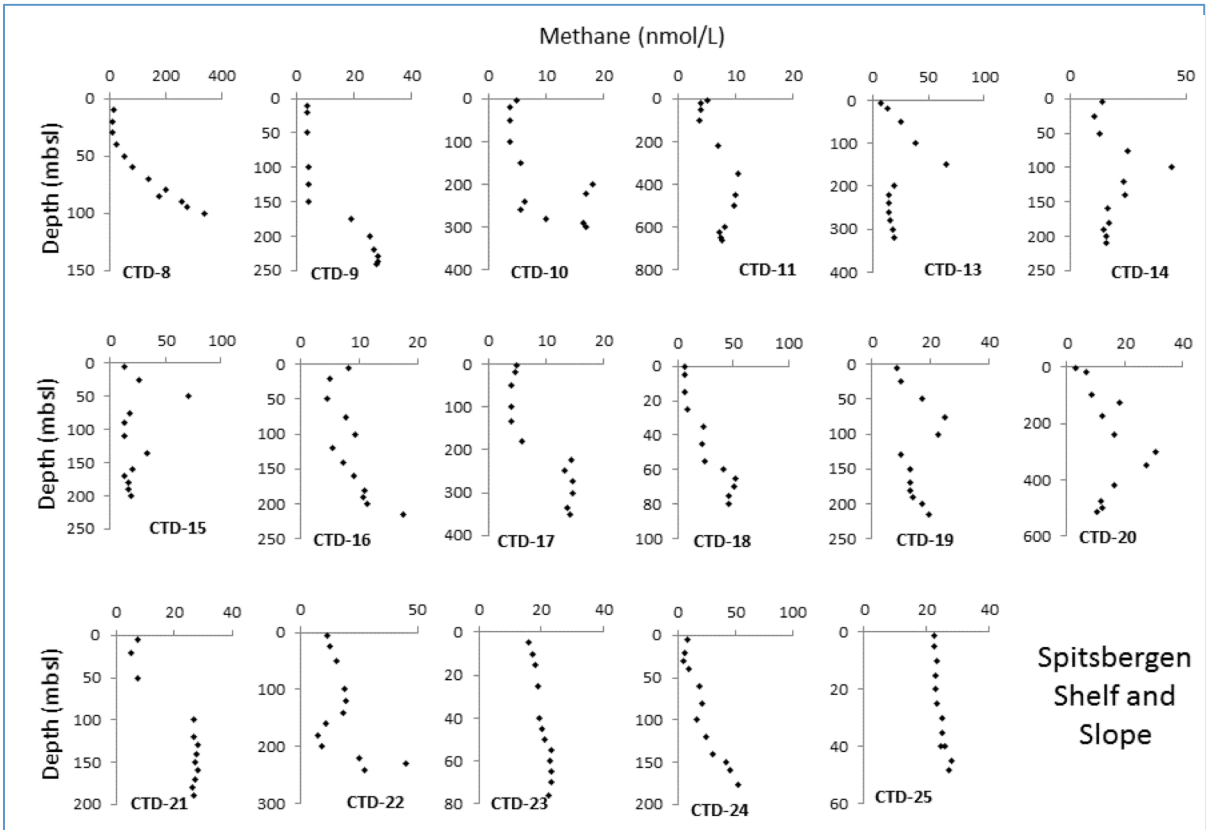

Fig. 15: Methane concentration profiles for stations along the Spitsbergen shelf/slope (Area 2), for station locations see Figure 10

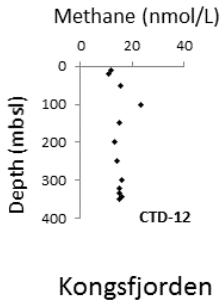

Fig. 16. Methane concentration profile for the Kongsforden station, for station location see Figure 10

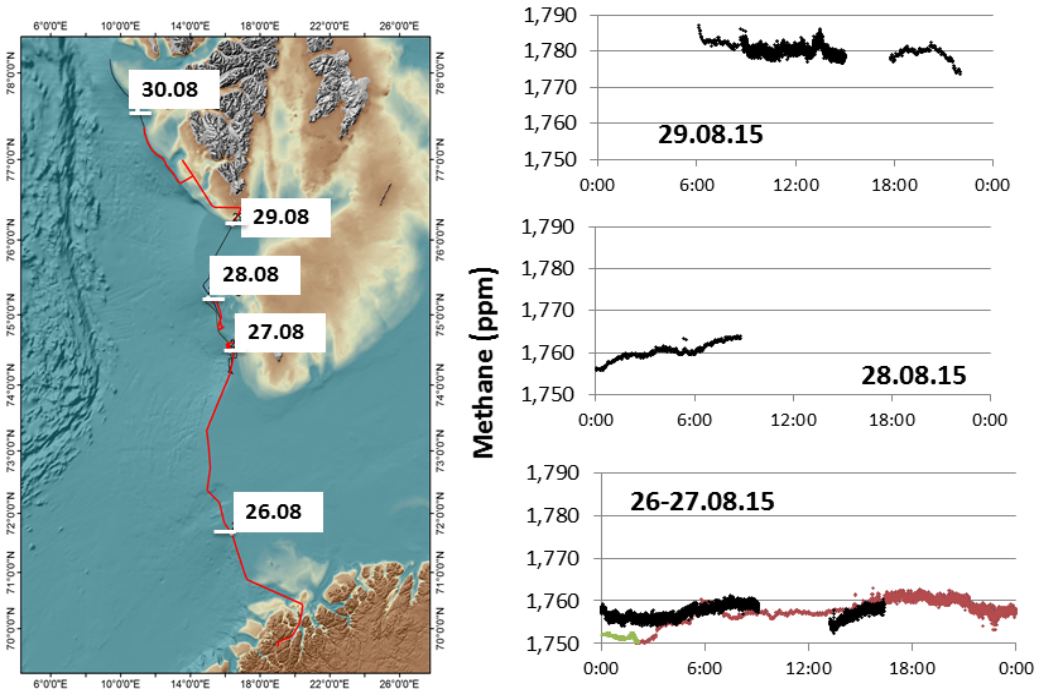

Fig. 17: Example of the methane in continuous air measurements, showing the data from 26.08.15 to 29.08.15 and the corresponding ship tracks.

5.3.3 Methane in air samples

Methane concentration in air samples is illustrated in Fig. 17. Values for samples collected during the transit from Tromsø to Spitsbergen during 26.08. and 28.08., range from 1.7502 to 1.7619 ppm. In contrast, there is a marked increase in concentration along the shelf of Hornsund, with values ranging from 1.774 to 1.787 ppm, with maximum single-point measurements of up to 1.805 ppm (Fig. 17). These elevated values correspond to locations of active seepage along the shelf, where methane in the surface water ranges from 8 to 14 nmol/l, as measured in this study and in several other hydrocasts in this area collected during HE 449 (Mau, 2015). The surface methane concentrations above saturation are confined to the shelf and do not extend towards the slope. Accordingly, air samples show a marked and rapid decrease from an average value of 1.78 ppm above the shelf seep region to the background concentration range of 1.750 to 1.762. Even above the active seepage areas offshore Prins Karls Forland, where numerous flares were observed during this cruise and by others (Westbrook et al., 2009; Gentz et al., 2013; Sahling et al., 2014), methane in air samples do not show significant elevation over background values. This is consistent with the observation that the dissolved methane plume remains below the pycnocline, with little vertical transport. Results from modeling and field work in this area and elsewhere have revealed that gas exchange between methane in bubbles and other gases in seawater is so rapid that just after a 20 m rise from the seafloor, only 20% of the initial methane remains in the bubble (Gentz et al., 2013).

References

Archer, D. and Buffett, B. (2005) Time-dependent response of the global ocean clathrate reservoir to climate and anthropogenic forcing, Geochem. Geophys. Geosy., 6, Q03002,doi:10.1029/2004GC000854.

Berndt, C., Feseker, T., Treude, T., Krastel, S., Liebetrau, V., Niemann, H., Bertics, V. J., Dumke, I., Dünnbier, K., Ferré, B.,Graves, C., Gross, F., Hissmann, K., Hühnerbach, V., Krause, S.,Lieser, K., Schauer, J., and Steinle, L. (2014) Temporal constraints on hydrate-controlled methane seepage off Svalbard, Science, 343, 284–287, doi:10.1126/science.1246298.

Biastoch, A., T. Treude, L. H. Rüpke, U. Riebesell, C. Roth, E. B. Burwicz, W. Park, C. W. Böning, M.Latif, G. Madec and K. Wallmann (2011) Rising Arctic Ocean temperatures cause gas hydratedestabilization and ocean acidification, Geophysical Research Letters, 38, L08602, doi:10.1029/2011GL047222.

Chabert, A., Minshull, T. A., Westbrook, G. K., Berndt, C., Thatcher, K. E., and Sarkar, S. (2011) Characterization of a stratigraphically constrained gas hydrate system along the western continental margin of Svalbard from ocean bottom seismometer data, J. Geophys. Res., 116, B12102, doi:10.1029/2011jb008211.

Chand, S., Thorsnes, T., Rise, L., Brunstad, H., Stoddart, D., Bøe, R., Lågstad, P., Svolsbru, T. (2012) Multiple episodes of fluid flow in the SW Barents Sea (Loppa High) evidenced by gas flares, pockmarks and gas hydrate accumulation. Earth and Planetary Science Letters 331–332, 305-314.

Cynar, F.J., Yayanos, A.A. (1992) The distribution of methane in the upper waters of the southern California Bight. Journal of Geophysical Research: Oceans 97, 11269-11285.

Damm, E., Mackensen, A., Budéus, G., Faber, E., and Hanfland, C. (2005) Pathways of methane in seawater: Plume spreading in an Arctic shelf environment (SW Spitsbergen), Cont. Shelf Res., 25, 1453-1472.

Fisher, R. E., Sriskantharajah, S., Lowry, D., Lanoisellé, M., Fowler, C. M. R., James, R. H., Hermansen, O., Lund Myhre, C., Stohl, A., Greinert, J., Nisbet-Jones, P. B. R., Mienert, J., and Nisbet, E. G. (2011) Arctic methane sources: Isotopic evidence for atmospheric inputs, Geophys. Res. Lett., 38, L21803, doi:10.1029/2011gl049319.

Gentz, T., Damm, E., Schneider von Deimling, J., Mau, S., McGinnis, D.F., Schlüter, M. (2014) A water column study of methane around gas flares located at the West Spitsbergen continental margin. Continental Shelf Research 72, 107-118.

Hustoft, S., Bünz, S., Mienert, J., and Chand, S. (2009) Gas hydrate reservoir and active methane-venting province in sediments on < 20 Ma young oceanic crust in the Fram Strait, offshore NW-Svalbard, Earth Planet. Sc. Lett., 284, 12–24, doi:10.1016/j.epsl.2009.03.038.

Knies, J., Damm, E., Gutt, J., Mann, U., and Pimnturier, L. (2004) Nearsurface hydrocarbon anomalies in shelf sediments off Spitsbergen: Evidence for past seepages, Geoch., Geophys., Geosy., 5, doi:10.1029/2003GC000687.

Lammers, S. and Suess, E. (1994) An improved head-space analysis method for methane in seawater, Mar. Chem., 47, 115-125.

Landvik, J. Y., Bondevik, S., Elverhoi, A., Fjeldskaar, W., Mangerud, J., Salvigsen, O., Siegert, M. J., Svendsen, J.-I., and Vorren, T. O. (1998) The last glacial maximum of Svalbard and the Barents Sea area: Ice sheet extent and configuration, Quaternary Sci. Rev., 17, 43–75.

Landvik, J.Y., Ingólfsson, Ó., Mienert, J., Lehman, S.J., Solheim, A., Elverhøi, A., Ottesen, D.A.G. (2005) Rethinking Late Weichselian ice-sheet dynamics in coastal NW Svalbard. Boreas 34, 7-24.

Mienert, J., Vanneste, M., Haflidason, H., and Bünz, S. (2010) Norwegian margin outer shelf cracking:a consequence of climate-induced gas hydrate dissociation? International Journal for Earth Sciences, DOI 10.1007/s00531-010-0536-z.

Ostanin, I., Anka, Z., di Primio, R., Bernal, A. (2013) Hydrocarbon plumbing systems above the Snøhvit gas field: Structural control and implications for thermogenic methane leakage in the Hammerfest Basin, SW Barents Sea. Marine and Petroleum Geology 43, 127-146.

Pape, T., Bahr, A., Rethemeyer, J., Kessler, J.D., Sahling, H., Hinrichs, K.-U., Klapp, S.A., Reeburgh, W.S., Bohrmann, G. (2010) Molecular and isotopic partitioning of low-molecular-weight hydrocarbons during migration and gas hydrate precipitation in deposits of a high-flux seepage site. Chemical Geology 269, 350-363.

Rajan, A., Mienert, J., and Bünz, S. (2012) Acoustic evidence for a gas migration and release system in Arctic glaciated continental margins offshore NW-Svalbard, Mar Petrol Geol, 32, 36-49.

Rehder, G. (1999) Quellen und Senken marinen Methans zwischen Schelf und offenem Ozean, GEOMAR, Kiel, 161 pp.

Ritzmann, O., Jokat, W., Czuba, W., Guterch, A., Mjelde, R., Nishimura, Y. (2004) A deep seismic transect from Hovgård Ridge to northwestern Svalbard across the continental-ocean transition: A sheared margin study. Geophysical Journal International 157, 683-702.

Sahling, H., Bergès, B., Boelmann, J., Dimmler, W., Geprägs, P., Glockzin, M., Kaboth, S., Nowald, N., Pape, T., Römer, M., Dos Santos Ferreira, C., Schroedter, L., Tomczyk, M. (2012) R/V Heincke cruise report HE-387. Gas emissions at the Svalbard continental margin. Longyearbyen - Bremerhaven, 20 August - 16 September 2012., Berichte, MARUM - Zentrum für Marine Umweltwissenschaften, Fachbereich Geowissenschaften, Universität Bremen, p. 170.

Sahling, H., Römer, M., Pape, T., Bergès, B., dos Santos Fereirra, C., Boelmann, J., Geprägs, P., Tomczyk, M., Nowald, N., Dimmler, W., Schroedter, L., Glockzin, M., Bohrmann, G. (2014) Gas emissions at the continental margin west of Svalbard: mapping, sampling, and quantification. Biogeosciences 11, 6029-6046.

Sarkar, S., Berndt, C., Minshull, T. A., Westbrook, G. K., Klaeschen, D., Masson, D. G., Chabert, A., and Thatcher, K. E. (2012) Seismic evidence for shallow gas-escape features associated with a retreating gas hydrate zone offshore west Svalbard, J. Geophys. Res.-Sol Ea, 117, B09102, doi:10.1029/2011jb009126.

Ślubowska-Woldengen, M., Rasmussen, T.L., Koç, N., Klitgaard-Kristensen, D., Nilsen, F., Solheim, A. (2007) Advection of Atlantic Water to the western and northern Svalbard shelf since 17,500 cal yr BP Quaternary Science Reviews 26, 463-478.

Svendsen, J.I., Alexanderson, H., Astakhov, V.I., Demidov, I., Dowdeswell, J.A., Funder, S., Gataullin, V., Henriksen, M., Hjort, C., Houmark-Nielsen, M., Hubberten, H.W., Ingólfsson, Ó., Jakobsson, M., Kjær, K.H., Larsen, E., Lokrantz, H., Lunkka, J.P., Lysså, A., Mangerud, J., Matiouchkov, A., Murray, A., Möller, P., Niessen, F., Nikolskaya, O., Polyak, L., Saarnisto, M., Siegert, C., Siegert, M.J., Spielhagen, R.F., Stein, R. (2004) Late Quaternary ice sheet history of northern Eurasia. Quaternary Science Reviews 23, 1229-1271.

Vanneste, M., Guidard, S., and Mienert, J. (2005) Bottom-simulating reflections and geothermal gradients across the western Svalbard margin, Terra Nova, 17, 510–516, doi:10.1111/j.1365-3121.2005.00643.x.

Vogt, P.R., Crane, K., Sundvor, E., Max, M.D., Pfirman, S.L. (1994) Methane-generated(?) pockmarks on young, thickly sedimented oceanic crust in the Arctic: Vestnesa ridge, Fram strait. Geology 22, 255-258.

Westbrook, G. K., Thatcher, K. E., Rohling, E. J., Piotrowski, A. M., Pälike, H., Osborne, A. H., Nisbet, E. G., Minshull, T. A., Lanoiselle, M., James, R. H., Hühnerbach, V., Green, D., Fisher, R. E., Crocker, A. J., Chabert, A., Bolton, C., Beszczynska-Möller, A., Berndt, C., and Aquilina, A. (2009) Escape of methane gas from the seabed along the West Spitsbergen continental margin, Geophys Res Lett, 36, 10.1029/2009GL039191.

Winkelmann, D. and R. Stein (2007) Triggering of the Hinlopen/Yermak Megaslide in relation to paleoceanography and climate history of the continental margin north of Spitsbergen. Geochemistry, Geophysics, Geosystems 8(6): Q06018.

Geochemistry Data Report
December 2015

Pore water geochemistry- Svalbard margin
Data Report

Introduction:

Since the discovery of hydroacoustic flares coincident with the upper limit of gas hydrate stability zone (GHSZ) west of Spitsbergen (Westbrook et al., 2009), there have been many studies aimed at investigating the potential link between gas hydrate dissociation due to warming and fate of the methane released to the water column and potentially the atmosphere (Gentz et al., 2013; Sahling et al., 2014, Berndt et al., 2014). Hydroacoustic flares indicative of methane gas discharge have been shown to cluster at water depths shallower than 400 meters west of Prins Karls Foreland, i.e at water depths shallower than those at which gas hydrate becomes thermodynamically unstable. There is an ongoing debate as to whether the observed bottom water temperature increase due to the recent warming of Arctic waters may enhance the dissociation of gas hydrate, or whether the observed methane release is controlled by seasonal temperature fluctuations (Westbrook, Berndt). The geochemistry of pore fluid provides fundamental information on the dynamics of the system, fluid sources and pathways. Geochemical data can also indicate recent changes in methane flux as well as the pattern of fluid migration in sediments (Kim et al., 2014).

Methods

Porewater samples were extracted from both multicores and gravity cores immediately after core recovery using acid-washed rhizons under the temperature of ~4 ^{o}C. Before subsampling of porewater and onboard analyses, samples were stored under room temperature for ca. 15 minutes to allow for temperature equilibration. The samples were collected in 20 ml acid washed syringes and subsequently filtered through 0.2 µm cellulose acetate in-line filters. Subsamples were preserved for shorebased analyses of sulfate by adding 6 ml of a 23.8 mM $Zn(OAc)_2$ solution (Sigma-Aldrich prod. #: 383317) less than 30 minutes after the syringe was disconnected from the rhizon. Samples for isotopic composition of dissolved inorganic carbon were preserved by addition of $HgCl_2$. Nutrient subsamples were frozen immediately andsubsamples for cation analyses were acidified with concentrated HNO_3.

Alkalinity and Fe^{2+} were measured onboard. Alkalinity was determined with a pH-controlled titration to a pH just under 4. The pH electrode was calibrated against pH 4, 7 and 10 Metrohm Instrument buffers. HCl titrant (12M Sigma-Aldrich TraceSELECT HCL diluted to 0.012M) was calibrated against 0.05M borax standard prepared in 0.7M KCl, diluted to 2, 10, 50 mM alkalinity. Each 2 ml sample aliquot was diluted with 8 ml of KCl (0.7M), and sequential aliquots of 0.012M HCl standard were added while constantly stirring in an open 50 ml beaker. The amount of acid and pH was manually recorded during each addition. Alkalinity was calculated from the Gran function plots, which were made by plotting Gran functions against the titrant volume. Gran function is defined as:

$(V_0+V_t)*10^{-pH}$

where V_0 is the initial volume of sample and V_t is the volume of titrant added. The concentration of alkalinity was then estimated from the slope and intercept of the regression line from the Gran function plot. Eight to ten points were used for regression.

Dissolved iron (Fe^{2+}) was determined spectrophotometrically using a ferrospectral complex in ascorbic acid (1%) at 565nm. Calibration curves were prepared from iron sulfate standards (10 points from 0.067 to 1 mg/L Fe) and run with each sample batch. Standard and ferrospectral solutions were prepared daily with anoxic MilliQ water using acid-washed volumetric flasks. Measurements were done within an hour after the water samples were extracted.

Analysis of the isotopic composition ($\delta^{13}C$) of dissolved inorganic carbon was conducted at Oregon State University using a Gas-Bench II automated sampler interfaced to a gas source stable isotope mass spectrometer as described in Torres et al., (2005). DIC is allowed to evolve as CO_2 by addition of H_3PO_4. A known volume of dry CO_2 is transferred to a Finnigan DELTAplusXL mass spectrometer, which integrates the relevant isotope masses (m/z = 44, 45, and 46) as the CO_2 peak enters the source. The precision of the $\delta^{13}C$ measurements based on replicate analyses of a $NaHCO_3$ stock solution is better than ±0.1‰. Estimates of DIC concentration [DIC] reported here are based on the voltage peak obtained during $\delta^{13}C$ measurements, also calibrated against analyses of a $NaHCO_3$ stock solution. Precision of the [DIC] measured by this technique is ~4%.

For sulfate and chloride analyses, we used a Dionex ICS - 1100 Ion Chromatograph at the laboratory of the Norwegian Geological Survey (NGU) at Trondheim. The instrument is outfitted with an AS-DV autosampler and an IonPac AS23 column (eluent: 4.5 mM Na_2CO_3/0.8 mM $NaHCO_3$, flow: 1ml/min), and calibrated against IAPSO standards. The error of the analyses is usually lower than 2%.

Concentrations of major cations were measured by external calibration on a Leeman Labs Prodigy ICP-OES at Oregon State University. Calibration standards were diluted from primary solutions in 1% sub-boiling-distilled HNO_3, and samples were diluted 100-fold by volume in 1% HNO_3 prior to measurement. Accuracy is determined by repeat analysis of IAPSO Standard Seawater with a practical salinity of 34.993.

Results

Data are listed in Table 1, and downcore profiles are shown in Figure 1. We target the metabolites associated with anaerobic oxidation of methane (AOM) to investigate the biogeochemical consequence of methane supply at depth. From these porewater profiles, we can estimate the fluxes of key species to understand and quantify the carbon cycling in the shallow sediments (Figure 2).

We observe non-steady state behavior at several sites (Figure 1) that we interpret as the consequence of an enhanced methane supply from gas hydrate dissociation, in varying timescales. Further analyses will be conducted to unravel the history of gas venting in this region. Collectively these data will allow us to bridge the gap between flares detected in the water column and the seismic mapping of fluid migration at depth; information that is needed to unravel the complex interactions among ocean chemical, physical, geological, and biological processes operating on the seafloor and their sensitivity to both natural and anthropogenic changes in the Arctic region.

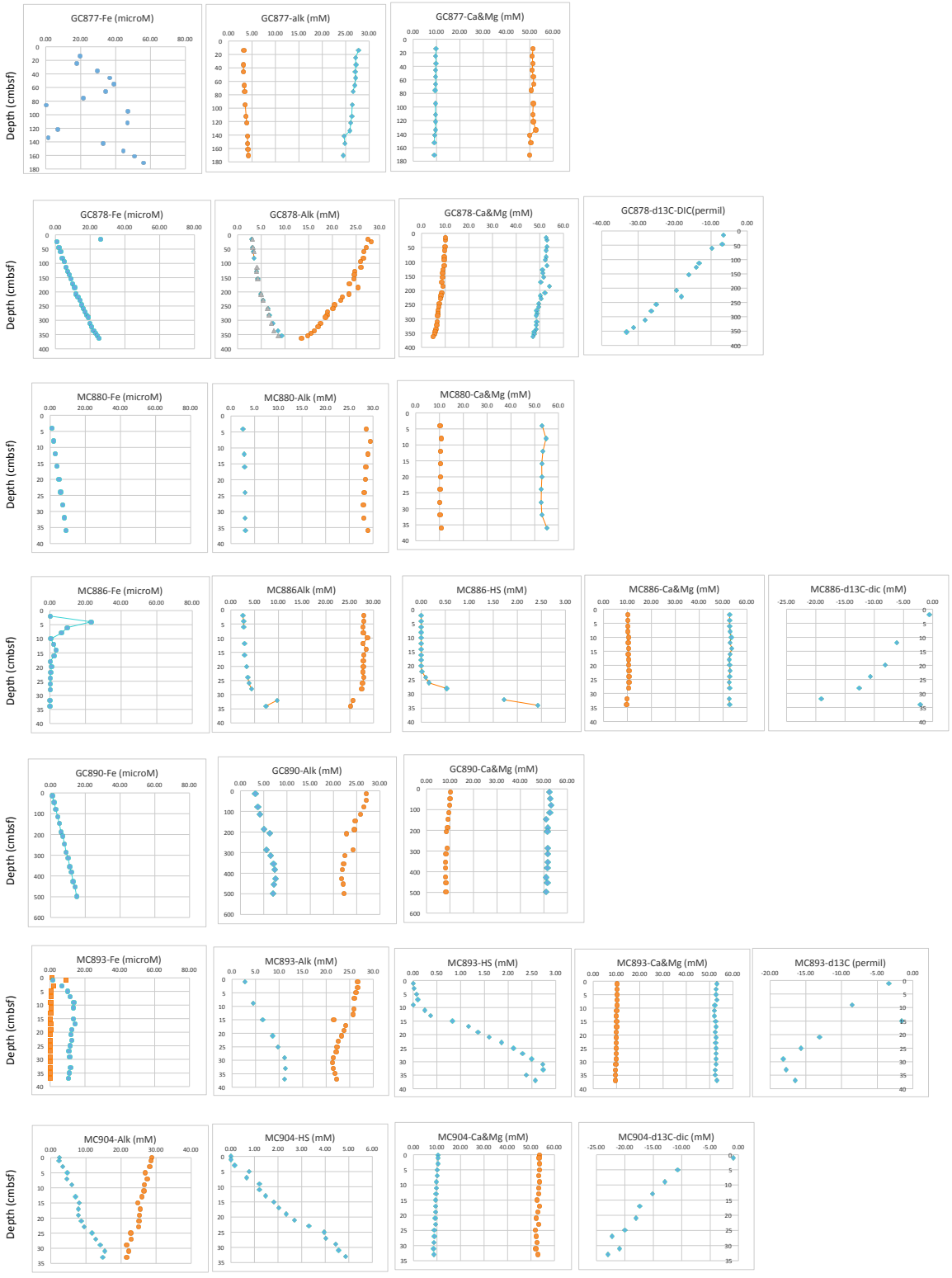

Figure 1. Downcore profiles of geochemical parameters in cores recovered from the Svalbard margin

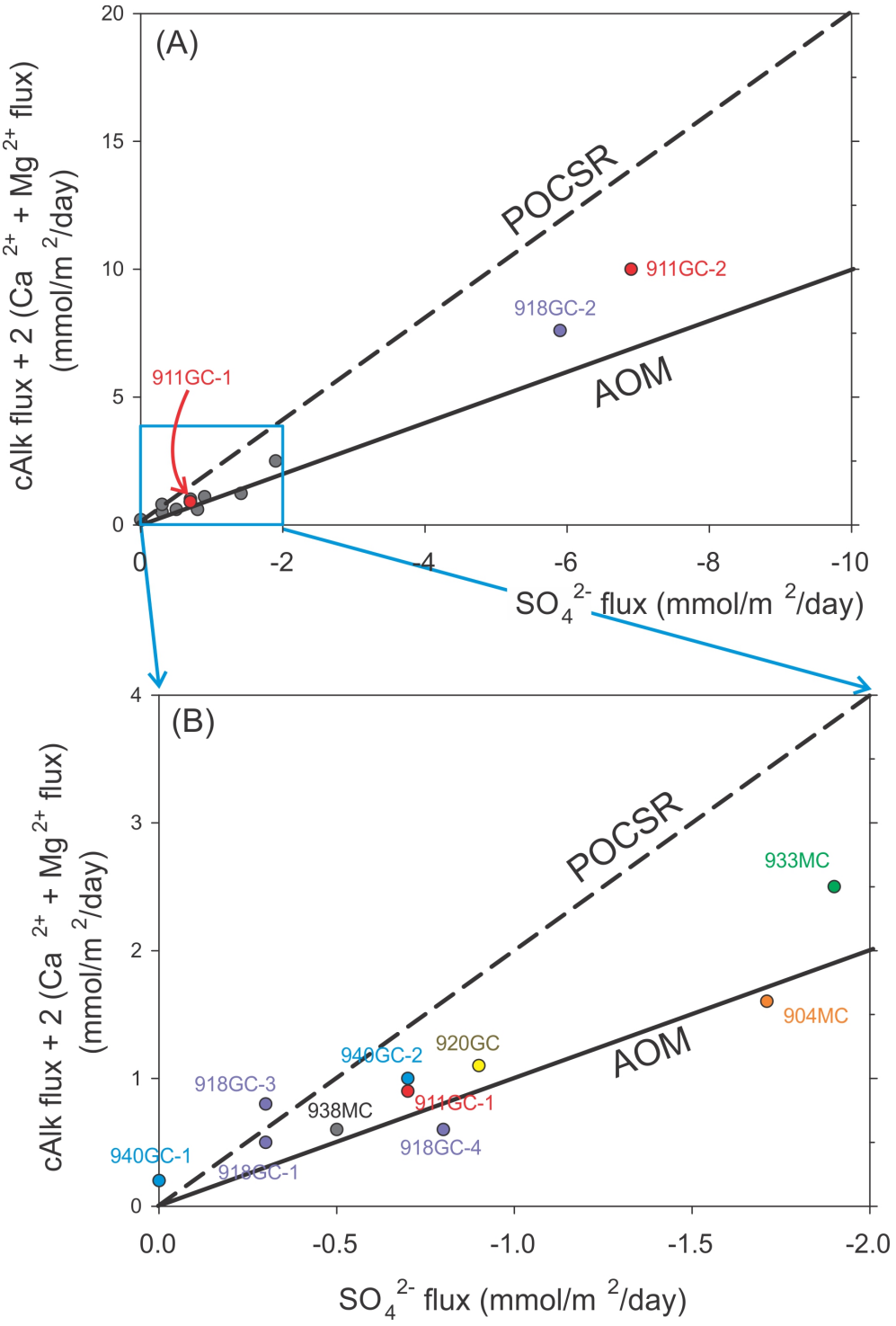

Figure 2- Preliminary flux estimates off Svalbard. AOM= anaerobic oxidation of methane, POCSR=particulate organic carbon sulfate reduction

Table 1- Pore water results from cores collected offshore Svalbard

Core number	depth (cm)	alk (mM)	d13C-DIC (ppt)	DIC (mM)	Fe2+ (microM)	HS (mM)	SO4 (mM)	SO4-ICPOES (mM)	Cl (mM)	Br (mM)	Na (mM)	Mg (mM)	K (mM)	Ca (mM)	d18O ppt	dD ppt
GC877	14	3.27			19.63	0.00	27.2	27.75	550	0.84	456.64	51.40	12.10	9.87		
	25				17.63	0.00		27.11			454.47	51.01	12.20	9.71		
	36	3.21			29.60	0.00		27.20			461.87	51.36	12.27	9.75		
	46	3.18			36.70	0.00	37.6	27.07	770	1.04	458.65	50.94	12.24	9.65		
	55				38.90	0.00		27.14			466.39	51.58	12.50	9.72		
	66	3.35			34.18	0.00		26.94			466.38	51.68	12.38	9.73		
	76	3.46			21.70	0.00		26.58			458.39	50.66	12.28	9.47		
	86				0.29	0.00										
	95	3.54			47.23	0.00		26.37			468.51	51.50	12.57	9.58		
	112	3.73			46.84	0.00	25.0	26.33	547	0.84	471.85	51.30	12.59	9.55		
	122	3.86			6.72	0.00		26.10			470.20	51.61	12.23	9.56		
	134				1.46	0.00		25.95			485.00	52.61	12.71	9.64		
	142	4.00			33.02	0.00		24.68			458.43	49.94	12.05	9.14		
	153	4.08			44.53	0.00		24.85			463.35	50.45	12.15	9.13		
	162	4.13			50.77	0.00										
	171	4.21			56.00	0.00	23.8	24.54	556	0.89	466.92	50.07	12.27	9.06		
GC878	25				bd			28.2			467	53.0	11.4	10.1		
	46	3.18	-6.90	3.24	9.33	0.00		27.3			469	53.0	11.3	9.9		
	60	3.31	-9.81	3.5	21.66	0.00	25.5	26.7	544	0.7	466	52.6	11.3	9.8		
	83	3.53			30.98	0.00		26.6			469	52.6	11.3	9.6		
	94				29.93	0.00		26.0			466	52.5	11.2	9.5		
	113		-13.22	4.09	21.93	0.00		26.0			476	53.2	11.4	9.6		
	128	3.98	-14.04	3.97	23.04	0.00	23.0	24.8	522	0.7	457	51.2	10.9	9.1		
	140				9.47	0.00		24.7			460	51.4	10.9	9.0		
	154	4.28	-16.07	4.27	16.06	0.00	23.4	24.5	547	0.8	464	51.7	11.1	8.9		
	172				bd	0.00		23.6			459	50.5	11.1	8.6		
	185				4.65	0.00		25.4			493	54.1	11.6	9.1		
	209	4.92	-19.47	4.99	bd	0.00	24.4	23.5	604	0.9	476	52.2	11.3	8.6		
	219				bd	0.00		22.1			459	50.3	10.9	8.1		
	230	5.42	-18.08	5.40	bd			21.8			465	50.5	11.1	8.0		
	246				0.21	0.00		20.5			460	49.5	11.0	7.5		
	258	6.43	-25.02	6.36	bd	0.00	19.8	20.1	553	0.8	461	49.6	10.9	7.4		
	271				bd	0.00		***19.0***			455	***48.7***	***10.6***	7.0		
	281	6.71	-26.40	6.62	bd	0.00		18.9			458	48.9	10.8	7.0		

Table 1- Pore water results from cores collected offshore Svalbard

Core number	depth	alk	d13C-DIC	DIC	Fe2+	HS	SO4	SO4-ICPOES	Cl	Br	Na	Mg	K	Ca	d18O	dD
	289				bd	0.00		18.6			458	48.6	10.7	6.9		
	311	7.51	-28.04	7.12	bd	0.00	17.4	17.5	553	0.7	460	48.7	10.6	6.5		
	322				bd	0.00		17.0			461	48.6	10.7	6.3		
	337	8.48	-31.32	7.62	bd	0.00		16.2			464	48.4	10.6	6.1		
	345				bd	0.00		15.5			457	47.6	10.5	5.8		
	354	9.33	-33.18	8.6	bd	0.00	14.5	14.8	558	0.8	462	47.6	10.6	5.5		
	364				0.03			13.5			459	47.0	10.6	5.0		
	16	2.95	-6.46	3.10	8.46	0.00	26.5	27.6	547	0.7	461	52.67	11.00	10.0		
MC880	4	2.50			bd	0.00	27.6	28.6	556	0.7	463.0	53.2	11.0	10.3		
	8				0.26	0.00		29.4			478.1	54.8	11.3	10.7		
	12	2.79			4.03	0.00		29.0			469.5	53.5	11.4	10.5		
	16	2.84			11.37	0.00		28.5			465.2	53.0	11.3	10.4		
	20				12.69	0.00		28.4			465.1	53.0	11.2	10.3		
	24	2.91			24.46	0.00	27.0	28.1	553	0.8	461.7	52.8	11.2	10.3		
	28				31.72	0.00		28.0			460.8	52.8	11.3	10.2		
	32	3.01			34.75	0.00		28.0			464.3	53.1	11.2	10.3		
	36	3.03			41.40	0.00	26.9	28.9	553	0.8	484.4	55.2	11.8	10.6		
MC886	0				0.59	0.00	26.7	28.24	539	0.68	464.74	53.27	10.96	10.20		
	2	2.51	-0.54	2.65	0.34	0.00		28.01			458.87	52.84	10.62	10.12	0.22	1.76
	4	2.70			23.32	0.00		27.97			459.11	52.80	10.77	10.22	6.50	10.32
	6	2.71			9.74	0.00		27.81			459.30	52.81	10.72	10.24	0.14	1.90
	8				6.54	0.00		27.88			458.46	52.98	10.88	10.21	0.11	1.67
	10				0.57	0.00		28.74			464.94	53.48	10.94	10.44		
	12	2.89	-6.12	3.01	2.04	0.00	26.7	27.81	542	0.80	460.99	52.91	11.05	10.32	0.22	2.05
	14				3.57	0.00		28.50			468.15	53.71	11.00	10.47	0.36	2.61
	16	2.86			2.42	0.00		27.97			461.51	52.95	10.92	10.34	0.60	2.72
	18				0.11	0.00		27.85			458.37	52.68	10.77	10.57		
	20	3.27	-8.12	3.39	0.90	0.00	26.5	27.85	536	0.79	459.54	52.85	10.89	10.54		
	22				0.47	0.01		27.83			457.57	52.91	10.71	10.62		
	24	3.60	-10.67	3.55	0.27	0.09		27.99			454.97	52.78	10.82	10.65		
	26	3.80			0.36	0.16	26.5	27.71	530	0.67	456.19	52.64	10.86	10.72		
	28	4.38	-12.56	3.86	0.16	0.54	26.3	27.53	536	0.72	456.10	52.79	10.79	10.53		
	30															
	32	9.74	-19.08	4.45	0.07	1.72	24.2	25.68	539	0.67	454.43	52.54	10.81	9.88		
	34	7.44	-2.15	4.96	0.09	2.43	23.8	25.22	542	0.80	455.23	52.75	10.96	9.69		

Table 1- Pore water results from cores collected offshore Svalbard

Core number	depth	alk	d13C-DIC	DIC	Fe2+	HS	SO4	SO4-ICPOES	Cl	Br	Na	Mg	K	Ca	d18O	dD
GC890	14	3.20			9.13	0.00	26.1	27.13	539	0.76	459.18	52.51	11.04	10.20		
	46				25.31	0.00		27.04			465.28	52.68	11.21	10.06		
	79	3.75			19.56	0.00		26.53			466.69	53.02	11.08	9.85		
	115	4.21			15.16	0.00	24.8	25.86	542	0.83	463.60	52.55	10.97	9.55		
	146				bd	na		24.67			450.16	50.88	10.73	9.06		
	188	5.08			1.43	0.00		24.49			459.66	51.85	10.76	8.99		
	208	6.30			bd	0.00	22.3	22.87	542	0.81	461.19	51.50	10.76	8.41		
	246															
	286	5.54			bd	0.00		24.27			462.25	51.82	10.79	8.81		
	315	6.46			0.05	0.00		22.49			461.91	51.60	10.83	8.24		
	355	7.11			0.07	0.00	21.6	22.19	553	0.76	465.99	51.71	10.88	8.18		
	382	7.30			0.07	0.00		21.95			465.30	51.49	10.88	8.06		
	428	7.49			bd	0.00	22.3	21.81	575	0.78	460.99	50.99	10.81	8.09		
	454	7.27			bd	0.00		22.08			465.66	51.52	10.81	8.23		
	499	7.03			0.01	0.00	25.2	22.25	632	0.91	461.15	51.15	10.62	8.28		
MC893	0				0.93			26.58			455.83	52.67	10.35	10.19		
	1	2.75	-3.36	2.56	9.27	0.01	26.7	27.18	544	0.76	461.75	53.23	10.51	10.30	0.18	2.31
	3				2.21	0.02	26.7	27.07	544	0.62	460.76	52.93	10.60	10.23	0.17	2.39
	5				0.78	0.07	26.3	26.97	544	0.71	460.79	52.92	10.68	10.25	0.11	2.23
	7				0.52	0.10	26.0	26.80	539	0.71	464.46	53.27	10.69	10.34	0.11	2.13
	9	4.52	-8.54	3.97	0.32	0.00		26.33			458.29	52.29	10.59	10.18	0.18	2.35
	11				0.49	0.24	25.9	26.08	547	0.72	456.11	52.20	10.72	10.11	0.12	2.22
	13				0.32	0.37	25.7	25.62	547	0.73	457.96	52.17	10.46	10.05	0.12	2.16
	15	6.51	-1.61	4.38	0.24	0.83	**21.63**	25.46	480	0.51	461.28	52.64	10.66	10.11		
	17				0.29	1.17	24.2	25.20	544	0.70	461.65	52.87	10.75	10.12	3.85	6.68
	19				0.32	1.37	23.8	24.93	542	0.61	457.07	52.48	10.51	9.97	0.14	2.33
	21	8.62	-13.07	5.31	0.15	1.60	23.3	24.55	542	0.81	459.67	52.78	10.53	9.97	0.21	2.23
	23				0.22	1.87	22.6	24.31	536	0.63	462.23	52.63	10.63	9.88	0.52	2.52
	25	9.72	-15.71	6.09	0.13	2.12	22.3	24.23	539	0.73	461.33	52.67	10.51	9.88	0.16	2.32
	27				0.16	2.30	22.1	23.63	542	0.74	462.00	52.83	10.75	9.79	0.15	2.24
	29	11.14	-18.16	6.95	0.22	2.49	21.5	23.01	542	0.72	463.98	52.87	10.75	9.80		
	31				0.16	2.73	21.3	23.25	542	0.73	464.38	52.85	10.54	9.69	0.15	2.28
	33	11.38	-17.73	6.37	0.15	2.74	21.5	22.94	533	0.65	457.55	52.46	10.60	9.57		
	35				0.22	2.38	21.9	23.04	544	0.68	461.35	52.53	10.66	9.56	0.15	2.04
	37	11.15	-16.45	5.91	0.21	2.58	22.2	23.42	550	0.68	467.44	53.24	10.73	9.62	0.26	2.53

Table 1- Pore water results from cores collected offshore Svalbard

Core number	depth	alk	d13C-DIC	DIC	Fe2+	HS	SO4	SO4-ICPOES	Cl	Br	Na	Mg	K	Ca	d18O	dD
MC904	0	2.41			0.08	0.00	31.8	28.87	556	6.18	468.05	53.71	10.65	10.34		
	1	2.30	-0.87	2.04	98.51	0.00	26.8	28.63	553	0.64	467.71	53.48	10.68	10.54		
	3	3.47			1.97	0.15	26.1	28.23	550	0.76	468.81	53.61	10.83	10.38		
	5	4.68	-10.72	3.59	0.26	0.76	26.2	26.95	570	0.74	470.48	53.80	10.83	10.24		
	7	4.56			0.16	0.67	25.6	27.52	547	0.63	466.94	53.25	10.78	10.02		
	9	6.06	-12.92	3.53	0.03	1.21	24.7	26.74	553	0.73	473.06	53.66	10.72	9.84		
	11				0.12	1.22	24.8	26.50	550	0.64	470.04	53.35	10.83	9.74		
	13	7.02	-15.12	3.54	0.14	1.48	24.0	25.96	553	0.77	469.09	53.37	10.77	9.57		
	15	8.02			0.30	1.83	23.3	24.79	556	0.76	461.77	52.65	10.70	9.28		
	17	7.89	-17.39	4.18	0.08	2.04	23.8	25.53	561	0.74	470.27	53.56	10.90	9.45		
	19	7.93			0.08	2.35	23.5	25.26	558	0.72	464.11	52.86	10.63	9.27		
	21	8.72	-18.03	4.55	0.07	2.69	23.2	25.13	556	0.72	461.18	52.43	10.53	9.22		
	23	9.57			0.03	3.31	22.4	25.11	550	0.71	470.80	53.27	10.67	9.30		
	25	11.79	-20.02	4.68	0.02	3.97	21.0	22.84	550	0.79	460.62	52.00	10.61	8.87		
	27	12.82	-22.22	6.06	0.16	4.03	20.8	22.92	556	0.72	462.93	52.33	10.76	8.83		
	29	14.10			0.02	4.45	19.0	21.61	539	0.69	465.02	52.55	10.74	8.62		
	31	15.43	-20.91	5.51	0.02	4.58	19.5	22.14	550	0.68	465.86	52.11	10.67	8.55		
	33	14.82	-22.99	6.86	0.06	4.88	19.3	21.65	550	0.72	468.19	52.85	10.88	8.61		
GC911	15	6.90	-16.94	4.56	1.24	1.23	23.9	26.39	553	0.82	461.80	52.11	10.69	9.55	0.12	2.17
	20	8.53	-19.40	4.83	1.24	2.30	22.9	25.98	544	0.77	470.85	53.18	10.87	9.60	0.10	1.63
	30	8.80	-17.83	4.26	1.03	2.94	22.9	28.70	536	0.71	451.36	52.18	10.14	9.64	0.03	1.52
	40	14.37	-24.64	7.70	0.06	4.81	19.6	26.39	547	0.77	455.44	52.31	10.48	8.73	0.15	1.80
	52	37.99	-27.10	17.67	0.06	10.27	0.7	7.11	542	0.78	450.42	50.23	10.40	4.77		
	57	35.06	-20.61	13.04	0.12	9.20	1.4	5.82	533	0.75	447.00	49.76	10.21	4.53	-0.07	0.63
	63	31.11	-18.89	18.02	0.12	5.95	0.0	3.11	550	0.74	453.71	49.77	11.17	3.62	0.01	1.15
	74	33.16	-15.23	18.38	0.12			2.45			440.98	48.94	10.73	3.47	0.06	0.33
GC918	8	4.00	-1.23	3.99	1.52	0.00	28.2	28.78	558	1.05	467.96	53.59	10.96	10.25	0.12	1.53
	18	4.31	-12.42	4.11	0.24	0.007	27.3	28.03	558	1.17	471.71	54.57	11.28	9.82	0.13	2.21
	27	19.78	-23.74	11.26	0.31	3.908	15.2	23.58	553	0.93	468.26	53.57	11.31	8.34	0.21	1.10
	32		-24.04	13.30	0.06	7.00	12.7	17.44	556	0.91	470.95	54.26	11.01	8.51	0.10	0.70
	38	26.44	-15.10	6.95		10.43	14.5	20.35	544	0.94	451.30	52.16	10.81	8.72		
	52	28.25	-18.54	9.71	0.11			19.91			466.45	53.79	11.18	9.02		
	66	30.95	-19.65	11.00		15.21	8.5	18.46	547	0.93	449.44	51.13	10.80	6.89		

Table 1- Pore water results from cores collected offshore Svalbard

Core number	depth	alk	d13C-DIC	DIC	Fe2+	HS	SO4	SO4-ICPOES	Cl	Br	Na	Mg	K	Ca	d18O	dD
GC920	10	2.97	-3.68	3.14	5.12	0.01	28.2	28.86	547	0.93	470.09	53.84	11.10	10.54	0.19	1.33
	31	10.28	-8.54	7.06	0.46	1.55	21.5	25.68	567	0.83	472.46	53.83	11.19	9.07	0.09	0.71
	50	17.39	-9.84	11.48	0.08	3.06	15.8	23.18	553	0.93	471.08	53.59	10.87	7.55		
	70	21.47	-10.79	14.53	0.13	4.15	13.5	19.15	556	0.87	480.70	54.66	11.31	7.05	0.11	0.51
	91	24.23	-10.96	14.88	0.13	4.41	11.7	22.25	556	0.83	471.22	53.61	10.96	6.50	0.02	0.36
	122	31.91	-5.31	11.66	1.00	5.90	5.9	10.10	558	0.83	475.80	53.82	11.14	5.10		
	146	37.68	-9.74	20.28	0.05	8.10	0.9	9.87	558	0.89	476.30	53.37	11.07	4.02		
	169	39.98	-6.52	20.70	0.16	7.20	0.0	5.00	564	0.83	468.98	52.96	10.63	3.55	0.04	0.40
	192	42.10	-1.11	25.33	0.10	7.34	0.0	4.63	561	0.85	472.55	53.99	10.74	3.71		
	215				0.07	2.50	0.0	1.27	575	0.91	482.28	55.39	10.93	3.84		
	240	43.93	6.32	30.68	0.13			0.84	584	0.81	486.18	56.38	10.95	3.90		
MC932	1	2.51			3.13	0.00	28.5	27.35	573	0.82974569	471.15	53.52	10.48	10.35		
	3	2.59			208.15	0.00		27.63			476.15	54.09	10.84	10.52		
	5	3.51			139.12	0.00	27.3	27.36	556	0.90	468.54	53.62	10.64	10.24		
	7	4.43			48.31	0.00		26.68			469.32	53.77	10.63	10.07		
	9	5.72			10.19	0.00		26.27			474.96	54.15	10.76	9.87		
	11	7.21			0.47	0.00	24.0	25.46	544	0.88	474.22	53.72	10.79	9.45		
MC938	2	2.56			34.99	0.00		27.93			459.88	52.52	10.65	10.35		
	3				58.06	0.00		28.11			471.38	53.59	10.77	10.52		
	6	2.79			13.23	0.00		28.39			469.47	53.35	10.79	10.50		
	10				0.38	0.00		28.07			460.20	52.67	10.57	10.36		
	12	2.96			0.72	0.09	26.9	27.84	547	0.74	466.42	52.92	10.83	10.43		
	14				0.80	0.15		28.00			466.16	52.94	10.67	10.40		
	16	3.07			0.44	0.17		28.10			468.28	53.15	10.72	10.45		
	18				0.62	0.25		28.18			470.79	53.62	10.79	10.55		
	20	3.35			0.33	0.43	27.3	28.34	547	0.92	474.32	53.55	10.76	10.50		
	22				0.27	0.72		28.48			474.49	53.96	10.92	10.51		
	24	4.30			0.17	1.10	26.6	28.01	553	0.89	468.80	53.17	10.81	10.28		
	26				0.17	1.28		28.29			472.05	53.56	10.85	10.23		
	28	5.09			0.19	1.33	25.5	26.75	544	0.89	470.03	53.15	10.86	10.17		
	30				0.17	1.50		26.72			468.79	53.33	10.81	10.08		
	32	5.49			0.16	1.66	25.6	26.44	558	0.87	468.21	53.02	10.76	10.00		
	34				0.17	1.47		26.77			472.39	53.59	10.93	10.09		
	36	5.45			0.17	1.60	26.9	26.62	584	0.82	473.36	53.58	10.73	10.09		
	8	2.91			1.23	0.00		28.44			468.60	53.72	10.92	10.63		

Table 1- Pore water results from cores collected offshore Svalbard

Core number	depth	alk	d13C-DIC	DIC	Fe2+	HS	SO4	SO4-ICPOES	Cl	Br	Na	Mg	K	Ca	d18O	dD
	0	2.60			0.19	0.00	29.2	28.77	581	0.89	475.86	54.20	10.81	10.68		
GC940	5	3.06	-4.05	3.10	60.05	0.00	27.6	28.94	550	0.80	475.62	54.01	11.11	10.68	0.91	2.53
	26	3.70	-8.35	3.66	0.19	0.00	27.2	28.15	556	0.91	475.92	53.87	11.35	10.58	0.76	2.24
	49	4.77	-13.82	4.56	0.13	0.09	27.0	27.13	575	0.91	474.16	53.53	11.28	10.29	0.13	1.08
	67	5.46	-17.56	5.12	0.11	0.30	27.1	25.95	604	0.80	474.81	53.23	11.20	10.05	0.04	1.09
	86	6.91	-20.05	6.18	0.26	0.59	24.6	24.89	578	0.94	478.99	52.87	11.33	9.71		
	107	7.73	-22.28	6.74	0.14	0.88	22.6	23.92	567	0.86	473.36	52.02	11.15	9.22	0.05	0.94
	129	9.37	-24.54	7.91	0.11	1.17	26.5	22.31	578	7.46	475.22	51.57	11.27	8.62	0.18	1.09
	150	10.84	-25.98	9.08	0.09	1.41	18.1	20.11	567	0.64	471.29	50.44	11.00	7.89	0.10	0.98
	166		-28.03	11.03				16.44			458.81	48.46	10.88	6.96		
	185	14.80	-28.66	12.58	0.06	1.88	11.8	13.19	556	0.64	458.07	47.80	10.64	6.08	0.01	0.49
	209	19.26	-31.79	14.53	0.06	2.57	6.5	8.43	564	0.67	467.72	46.46	10.79	4.73		
	313	20.64			0.21		0.0		561	0.79	454.57	38.78	9.96	1.91		
	235	24.19	-30.88	21.45	0.04	2.88	1.6	2.67	561	0.77	457.54	44.33	10.25	3.73		
	254	23.56	-25.46	19.28	0.19	2.51	0.0	1.07	556	0.64	458.69	42.69	10.11	2.99		
	271	21.65	-23.80	19.96	0.07	1.65	0.0	0.91	558	0.76	449.99	41.58	9.87	2.61		
	293	21.03	-18.60	18.89	0.21	0.47	0.0		553	0.70	454.58	39.85	10.07	2.19		
MC960	1	2.74			25.71	0.00	28.7	28.51	573	0.95	474.18	53.80	10.79	10.69		
	3	2.83			58.80	0.00		28.57			473.96	54.06	10.94	10.73		
	5	2.68			43.73	0.00		28.56			477.05	53.78	11.09	10.70		
	7	2.64			25.56	0.00		28.27			474.50	53.33	11.12	10.62		
	9	2.78			25.71	0.00	28.6	28.51	570	0.83	475.48	53.67	11.21	10.62		
MC965	1	2.63			15.61	0.00		28.43			477.92	54.35	10.90	10.66		
	3	2.64			21.33	0.00		28.44			476.41	54.01	10.78	10.64		
	5	2.72				0.00	27.8		553	0.91						
	7	2.51			11.19	0.00		28.10			471.01	53.36	10.76	10.53		
	11	3.07			14.70	0.00	27.8	27.92	553	0.80	471.67	53.52	10.74	10.51		

computation

MDPI

Article

Reduced Numerical Model for Methane Hydrate Formation under Conditions of Variable Salinity. Time-Stepping Variants and Sensitivity

Malgorzata Peszynska [1,*,†], Francis Patricia Medina [1,†], Wei-Li Hong [2,3,†] and Marta E. Torres [2,†]

Received: 28 November 2015; Accepted: 18 December 2015; Published: date
Academic Editors: Qinjun Kang and Li Chen

[1] Department of Mathematics, Oregon State University, Corvallis, OR 97331, USA; medinaf@science.oregonstate.edu
[2] College of Earth, Ocean, and Atmospheric Sciences, Oregon State University, Corvallis, OR 97331, USA; wei.l.hung@uit.no (W.-L. H.); mtorres@coas.oregonstate.edu (M.E.T.)
[3] CAGE (Centre for Arctic Gas Hydrate, Environment and Climate), Department of Geology, UiT The Arctic University of Norway, Tromso, Norway
* Correspondence: mpesz@math.oregonstate.edu; Tel.: 1-541-737-9847
† These authors contributed equally to this work.

Abstract: In this paper, we consider a reduced computational model of methane hydrate formation in variable salinity conditions, and give details on the discretization and phase equilibria implementation. We describe three time-stepping variants: Implicit, Semi-implicit, and Sequential, and we compare the accuracy and efficiency of these variants depending on the spatial and temporal discretization parameters. We also study the sensitivity of the model to the simulation parameters and in particular to the reduced phase equilibria model.

Keywords: methane hydrate; multiphase multicomponent flow and transport; reduced computational model; time-stepping; phase equilibria; salinity

MSC: 65M06; 76S05; 76V05; 35R35

1. Introduction

Computational simulation of complex phenomena can provide answers to problems for which no experimental data or theoretical studies are available, but it requires robust, efficient, and accurate numerical models. The problem considered in this paper is of evolution of methane hydrate, which is an ice-like substance present in large amounts in subsea sediments, and which plays an important role both as a potential energy source and environmental hazard as well as in global climate studies [1,2].

In the paper [3] we introduced a reduced model for methane hydrate formation in variable salinity conditions and provided details on the equilibrium phase behavior adapted to a case study from Ulleung Basin. One of the advantages of this reduced model in contrast to fully comprehensive models such as in, e.g., [4], is that the reduced model is easy to implement and to extend, and is amenable to various analyses.

In this paper we describe the computational aspects of the model, with the emphasis placed on the variants of time-stepping. Our reduced model accounts for three components: water, methane, and salt, and two phases: aqueous, and solid (hydrate). Thus, it places in the general framework of multiphase multicomponent models such as those in [5–7] for which accuracy and efficiency have been studied extensively in the past decades. In particular, for the oil-water or black-oil models

described e.g., in [8–13] the best practice is to use mass-conservative spatial schemes combined either with an implicit treatment of pressures and explicit treatment of saturations/concentrations, or with a fully implicit treatment of all phases and components. Typically, the computational complexity of implicit models is the highest, while other variants are easier to implement. In compositional models [14] with M components the pressure solver is complemented with M-1 transport equationssolved for concentration of the selected M-1 species, and followed by flash, *i.e.*, the equilibrium solver. The typical time scales of interest for reservoir simulation with these models are days to decades of production or environmental remediation. On the other hand, in [3] and here we are interested in long-term behavior and hydrate basin modeling, and it makes sense to assume that the pressures and temperatures are known and given by hydrostatic and geothermal distributions. Our models need only to resolve the interdependence between methane and water phase equilibria that depend on the presence of salt, and our time-stepping algorithms have different features than those for the oil-gas reservoir simulators.

We implement the interdependence between the components and phases as follows. The water-methane-salt equilibria are handled using the approach of nonlinear complementarity constraints, and are either tightly or loosely coupled to the salt mass conservation; their implementation is especially easy with the reduced phase behavior model adopted in [3]. We consider and compare three variants of time-stepping that realize these tight or loose couplings: the fully implicit (I), semi-implicit (SI), and sequential (SEQ) algorithms. The comparison that we carry out is intended to demonstrate the merits of these approaches, and guide the choice of a model.

In addition, in this paper we test the sensitivity of the approach to the assumed phase behavior model, as well as to various parameters defining the discretization. The latter is new and was not undertaken for the comprehensive model [4]. It is significant in that it guides the reader in the choice of optimal parameters and shows the robustness of the reduced model.

The paper is organized as follows. In Section 2 we briefly recall the model proposed in [3] including the phase behavior. In Section 3 we describe in detail the time-stepping variants and spatial discretization for that model. In Section 4 we compare the I, SI, and SEQ time-stepping variants, and in Section 5 we discuss the sensitivity of the model to the various parameters of the computational model. We conclude in Section 6.

2. Mathematical Model

In the last decade two classes of models for hydrates have been used to describe hydrate behavior in natural systems. These are the fully comprehensive equilibrium models such as [4], and the simpler conceptual models [2,15,16], in which simplified mechanisms for fluid equilibria and/or kinetics were assumed. The model presented in [3] and discussed here falls somewhere inbetween, and is a direct simplification of the comprehensive model in [4]. The simplicity of the reduced model allows for rigorous mathematical well-posedness analysis in the case of the diffusive transport in [17], and more general analysis in [18] for advective/diffusive transport.

We consider the transport of methane and salt in the sediment reservoir $\Omega \subset \mathbb{R}^d, d = 1,2,3$. The notation used throughout is provided in Table 1. Each point $x = (x_1, x_2, x_3) \in \Omega$ is at some depth $D(x)$ below the sea surface, with the origin $x = 0$ at the bottom of the Gas Hydrate Stability Zone (GHSZ). At the seafloor, *i.e.*, at the top of the reservoir Ω, we have $x = L$ where L is the thickness of the hydrate zone. Next, at the seafloor, the depth of water above seafloor is the reference depth $D_{ref} = H$, so the sea surface is at $x = L + H$. We also set the coordinate $z = D(x) - D_{ref} = D(x) - H$ measured in mbsf (meters below seafloor) which is used in other models [19]. In the general case of a 2D or 3D reservoir the bathymetry is variable, thus $D(x)$ is measured relative to the (constant) sea surface rather than to the seafloor.

Table 1. Notation and definitions.

Symbol	Definition	Units/value
	Data about reservoir and fluids	
$x = (x_1, x_2, x_3)$	Spatial coordinate	[m]
t	Time variable	[yr]
G	Gravitational acceleration	9.8 m/s^2
$D(x)$	Depth of point x from sea level	[m]
$D_{ref}(x)$	Seafloor depth	[m]
	In 1D case $x = x_3$, $H = D_{ref}$	
$z = D(x_3) - H$	Depth below seafloor	[m]
(G)HSZ	(Gas) Hydrate stability zone	
P	Pressure	[Pa,MPa]
G_H	Hydrostatic gradient	$\approx 10^4$Pa/m
T	Temperature	[K]
G_T	Geothermal gradient	[K/m]
q	Darcy volumetric flux of liquid phase	[m/yr]
$D_M = D_S = D^0 S_l \phi_0$	Diffusivity of component C in the liquid phase	[m^2/yr]
	$D^0 = 10^{-9}$m^2/s $= 3 \times 10^{-2}$m^2/yr	
ρ_l	Seawater density	1030 kg/m^3
ρ_h	Hydrate density	925 kg/m^3
χ_{hM}	Mass fraction of methane in hydrate phase	0.134 kg/kg
$R = \chi_{hM}\rho_h/\rho_l$	Constant used for methane concentration	0.1203 kg/kg
$\phi_0, \phi = S_l\phi_0$	Porosity in Ω without/with hydrate present	
K_0, K	Permeability in Ω without/with hydrate present	
χ_{lS}^{sw}	Seawater salinity	$0.035[kg/kg]$
f_M	Supply of methane (source/sink term)	[kg/kg/yr]
α	Parameter of the reduced model	[kg/kg]
	Variables in the model	
$S_l, S_h = 1 - S_l$	Void fraction of liquid and hydrate phases	
χ_{lM}	Mass fraction of methane (solubility) in liquid phase	[kg/kg]
χ_{lS}	Mass fraction of salt (salinity) in liquid phase	[kg/kg]
N_M, N_S	Mass concentration of methane and salt	[kg/kg]
	per kg of liquid phase	

In this paper as in [3] we assume that the conditions in Ω are favorable for hydrate presence and that Ω is entirely within the GHSZ, while the methane is supplied by advection and diffusion from beneath GHSZ. We also assume that $T(x)$ is known and follows the geothermal gradient

$$T(x) = T_{ref} + (D(x) - D_{ref})G_T, \tag{1}$$

where T_{ref} is the temperature at some reference depth D_{ref} and $G_T \approx const$ is the geothermal gradient; see [3] for experimental values. The pressure $P(x)$ is assumed close to the hydrostatic

$$P(x) \approx P_l^0(x) := P_l^0|_{D_{ref}} + \rho_l G(D(x) - D_{ref}). \tag{2}$$

Here P_l^0 is known at the reference depth D_{ref}.

Finally, the actual porosity $\phi(x)$ available to the liquid phase at x is $\phi = \phi_0 S_l$, where S_l is the liquid phase saturation, *i.e.*, void fraction of the liquid phase. The actual permeability $K(x)$ in the presence of hydrate is an important property. However, it is not needed in the 1D model with a constant flux and an assumed hydrostatic pressure distribution.

2.1. Mass Conservation

In region Ω we have the following mass conservation equations for methane and salt components, respectively

$$\frac{\partial \phi_0 N_M}{\partial t} - \nabla \cdot D_M \nabla \chi_{lM} + \nabla \cdot (q \chi_{lM}) = f_M, \tag{3a}$$

$$\frac{\partial \phi_0 N_S}{\partial t} - \nabla \cdot D_S \nabla \chi_{lS} + \nabla \cdot (q \chi_{lS}) = 0, \tag{3b}$$

with the definitions

$$N_M = S_l \chi_M + R(1 - S_l), \tag{3c}$$

$$N_S = \chi_{lS} S_l. \tag{3d}$$

where R is given in Table 1. The model is complemented by a pressure equation or q must be given; here we assume the latter. As we explain in [3], the Equation (3) arises as a special case of the first-principles comprehensive model in [4].

We see that in Equation (3) we have two mass conservation Equations (3a),(3b) with three unknowns that must be chosen from $N_M, N_S, \chi_{lS}, \chi_{lM}$ and S_l. To close the system we use the nonlinear complementarity constraint abbbreviated below as [NCC-M] phase constraint. We explain it below.

2.2. Phase Equilibria and [NCC-M] Constraint

The (maximum) amount χ_{lM}^{max} of methane that can be dissolved in the liquid phase depends on the pressure P, temperature T, and the salinity χ_{lS}. Equivalently, these variables determine the circumstances in which $S_l < 1$ and $S_h > 0$, *i.e.*, when the hydrate phase can be present. In addition, χ_{lM}^{max} determines how the total amount of methane N_M is partitioned between the liquid and hydrate phases. This phase equilibrium is expressed concisely as a nonlinear complementarity constraint [NCC-M]

$$\begin{cases} \chi_{lM} \leq \chi_{lM}^{max}, & S_l = 1, \\ \chi_{lM} = \chi_{lM}^{max}, & S_l \leq 1, \\ (\chi_{lM}^{max} - \chi_{lM})(1 - S_l) & = 0. \end{cases} \tag{3e}$$

In other words, if $N_M(x,t)$ is small enough so that $N_M < \chi_{lM}^{max}$, then only the liquid phase is present $S_l(x,t) = 1$, and $\chi_{lM} = N_M$ is the independent variable that describes how much methane is dissolved in the liquid. On the other hand, when the amount present $N_M \geq \chi_{lM}^{max}$, the excess amount of methane above χ_{lM}^{max} forms the hydrate phase with $S_h = 1 - S_l > 0$, and $S_l < 1$ becomes the independent variable while $\chi_{lM} = \chi_{lM}^{max}$. This relationship has to be satisfied at every point x, t.

2.2.1. Data for χ_{lM}^{max}

In the hydrate literature [4,20] there are tabulated data, or algebraic models, for how χ_{lM}^{max} depends on P, T, χ_{lS}. In addition, there may be dependence of Equation (3e) on the type of sediment [19,21] but this is out of scope here. In [3] we developed a particular approximation

$$\chi_{lM}^{max} \approx \chi_{lM}^{max}(x, \chi_{lS}) \approx \chi_{lM}^{max,0}(x) + \alpha(x) \chi_{lS}, \tag{4}$$

in which the data $\chi_{lM}^{max,0}(x)$ and $\alpha(x)$ must be provided. This approximation Equation (4) includes as a special case the algebraic model in [19]. In [3] we describe how to obtain $\chi_{lM}^{max,0}(x)$ and $\alpha(x)$ by a fit to the lookup tables extracted from the well known phase equilibrium software CSMGem [22], and we calibrate them for the typical depth, temperature, and salinity conditions found in Ulleung Basin; see the plot of $\chi_{lM}^{max,0}(x)$ and $\alpha(x)$ in Figu[illegible]. As is well known, $\chi_{lM}^{max,0}$ increases with depth, thus

decreases with x. On the other hand, $\alpha(x)$ found with CSMGem is positive while the authors in [23] believe it should be negative; see [3] for details. In Section 5 we discuss the sensitivity of the model to the assumed profile of $\alpha(x)$.

2.2.2. Other Constraints

There are additional constraints that are not part of Equation (3) but are motivated by the physical meaning of the variables S_l, S_h, and χ_{lM}. In particular, we must have $S_h \leq 1$ or

$$S_l \geq 0, \chi_{lM} \geq 0. \tag{5}$$

With some assumptions on χ_{lM}^{max}, the boundary and initial data, and small f_M, q one can prove that Equation (5) holds as a consequence of the maximum principle and other abstract analyses. (See [17] for the diffusive case and [18] for advective and diffusive transport case).

In more general circumstances one cannot prove that Equation (5) holds. In fact, a numerical model may readily produce S_h increasing to 1 and beyond. This clearly is nonphysical, since even before the pores become plugged up and $\phi = S_l\phi_0 = 0$, all the flow and diffusion ceases, local pressures increase, and the sediment may break.

When Equation (5) is violated, a model more general than Equation (3) should be considered. In particular, such a model should include geomechanics and pore-scale effects; see, e.g., the conceptual model described in [21]. However, the analysis of such a model is presently out of scope. In the model discussed in this paper we terminate the simulation when Equation (5) does not hold.

2.3. Boundary and Initial Conditions

The model Equation (3) must be supplemented with appropriate initial conditions imposed on N_M and N_S, and the boundary conditions on the fluxes or on the values of the transport variables χ_{lM} and χ_{lS}. In this paper we set

$$N_M(x,0) = N_M^0(x), \quad N_S(x,0) = N_S^0(x), \quad x \in \Omega \tag{6a}$$

$$\chi_{lM}(0,t) = \chi_{lM}^0, \quad \chi_{lM}(L,t) = \chi_{lM}^L = 0, \quad t > 0 \tag{6b}$$

$$\chi_{lS}(0,t) = \chi_{lS}^0, \quad \chi_{lS}(L,t) = \chi_{lS}^L \chi_{lS}^{sw}, \quad t > 0 \tag{6c}$$

The conditions Equation (6c) assign the seawater salinity at $x = L$ and some other salinity χ_{lS}^0 at HSZ known from observations. The conditions Equation (6b) assume some methane present at HSZ $x = 0$, and that there is no methane in the ocean at $x = L$. The choice consistent with Equation (4)

$$\chi_{lM}^0 = \chi_{lM}^{max,0}(0) + \alpha(0)\chi_{lS}^0 \tag{7}$$

allows the maximum possible amount of methane to be transported by advection and diffusion from underneath the HSZ.

3. Numerical Model

Now we provide details of the numerical model for Equation (3). We use mass-conservative spatial discretization based on cell-centered finite differences (FD) with harmonic averaging and a nonuniform structured spatial grid. An alternative discretization of the case $q = 0$, with Finite Elements and mass lumping, was considered in [17], but it would not accommodate large advective fluxes and is not locally mass conservative. For time discretization we use operator splitting: we treat advection explicitly and diffusion implicitly as in [24–26]. The diffusion/equilibria handle two components and are organized in several time-stepping variants. In each variant we have to solve a linear or nonlinear system of equations; for the latter we use Newton (or semismooth Newton) iteration.

After the discretization of Equation (3), at each time step, one solves for the approximate values of the five unknowns $N_M, N_S, \chi_{lM}, \chi_{lS}, S_l$. (At this point we are not yet providing any notation specific to time steps or grid points). Note that Equation (3c) and Equation (3d) are merely the definitions of the terms used in the transport equations Equation (3a), Equation (3b) complemented by the phase equilibria Equation (3e). Thus we can eliminate and actually solve only for three variables $S_l, \chi_{lM}, \chi_{lS}$ the system of three equations which we write as

$$F_M(S_l, \chi_{lM}, \chi_{lS}) = 0, \tag{8a}$$
$$F_S(S_l, \chi_{lM}, \chi_{lS}) = 0, \tag{8b}$$
$$F_{NCC}(S_l, \chi_{lM}, \chi_{lS}) = 0. \tag{8c}$$

The details on discrete form of F_M, F_S, and F_{NCC} which correspond to Equations (3a), (3b), (3e), respectively, are developed below. We discuss first the most difficult part of implementing Equation (3e), then we provide details of discretization of the transport equations. The system Equation (8) is nonlinear, and we discuss next the particular variants of the solvers and time-stepping variants.

3.1. Implementing Phase Constraint [NCC-M] in Fully Implicit Models

While it is well known how to discretize and solve advection-diffusion equations, implementing phase equilibria constraint Equation (3e) is challenging. There are practical approaches which have been successfully implemented [4,7]. In addition, approaches known from constrained optimization [27,28] have been recently applied; see [17,29].

In the first class of approaches, the constraint Equation (3e) can be rewritten using the notion of *active/inactive sets* [27]. In this approach at each time step and/or iteration, the (grid) points are identified as either those for which the first part of the inequality Equation (3e) holds, or those where the other complementary inequality must hold. Next, the mass conservation equations are specialized depending on the state of the primary unknowns, and are grouped together and solved for the particular active set of independent unknowns. In summary, in each time step and/or iteration of the nonlinear numerical solver, the solver changes the vector of unknowns depending on which variables need to be used. In consequence, not just the values, but also the sparsity structure of the Jacobian matrix change from iteration to iteration. This approach is known as *variable switching* [4,7] where at each gridpoint one identifies the appropriate independent variable depending on which of the inequalities holds.

In another equivalent approach one takes advantage of the semismooth "min" function as proposed in [29]. We recall that the function "min(u,v)" equals u if $u \leq v$ and v otherwise. We represent Equation (3e) in an equivalent way as

$$\min(\chi_{lM}^{max} - \chi_{lM}, 1 - S_l) = 0. \tag{9}$$

In [17] we showed that the "min" representation of Equation (3e) is equivalent to variable switching discussed above. With the "min" function approach, Equation (9) is a nonlinear equation in the variables χ_{lM} and S_l, and it provides the fifth equation to complement Equations (3a)–(3d) that can be solved together for the five unknowns $N_M, N_S, \chi_{lM}, \chi_{lS}, S_l$.

Since the function "min(u,v)" is piecewise linear and non-differentiable along $u = v$, it is also *semismooth* [28]. The theory of semismooth maps developed in [28] allows us then to analyze the solvability of the resulting nonlinear system of equations.

We found that the approach using Equation (9) is easy to implement and vectorize, and is modular, *i.e.*, it does not require that we rewrite the complex logic of active/inactive sets whenever there is need to expand the logic or the physics in the model. The potential disadvantage of using Equation (9) is that the number of unknowns involved grows from two per grid point to three per

grid point. In practice, however, this has minimal implications on the storage, since all the variables must be stored anyway. On the other hand, the size of the linear system that arises at each iteration when solving Equation (8) is by 50% larger than the size of that with explicit variable switching. However, the matrices in the linear systems corresponding to both approaches are sparse. An efficient implementation of the "min" approach in which sparsity is fixed, can outweigh the cost of the variable switching approach in which the pattern of sparsity varies from iteration to iteration.

3.2. Implementing Phase Constraints in Non-Implicit Models

Some of the time-stepping variants other than fully implicit require local nonlinear solvers called "flash". These are invoked at each grid point ans solve a system simpler than Equation (3e) in which the values of one or of more of the variables are assumed known.

Simple flash. The simplest situation is when N_M is known and we know χ_{lM}^{max}. To determine S_l and χ_{lM} we simply use Equations (3e), (3c) to calculate

$$S_l = \frac{N_M - R}{\chi_{lM} - R} = \begin{cases} 1, & N_M \le \chi_{lM}^{max}(x,t), \\ \frac{N_M - R}{\chi_{lM}^{max}(x,t) - R}, & N_M > \chi_{lM}^{max}(x). \end{cases} \tag{10}$$

Simple flash only is applicable if salinity is fixed because of the dependence of χ_{lM} on χ_{lS}.

Two-variable flash. Given N_M, N_S we can solve for the three unknowns S_l, χ_{lM}, χ_{lS} using Equations (3c), (3d) and (9). The implementation is especially easy if Equation (4) is used. This flash solver typically takes 2 or 3 iterations to complete, but may fail when S_h is close to 1.

3.3. Notation in Fully Discrete Model

The notation for discretization is straightforward. We find approximations to the relevant variables at discrete time steps $t_1, t_2, \ldots t_n, \ldots$. The transport model Equation (3) advances the model variables from t_n to t_{n+1}, with the time step $\tau = t_{n+1} - t_n$ considered uniform for simplicity. Also for simplicity, we consider the 1D reservoir $\Omega = \bigcup_i \Omega_i$, where Ω_i are the cells with the centers x_i and uniform length h, and $i = 1, \ldots N_x$. We approximate $N_M(x_i, t_n) \approx N_{M,i}^n$ and set N_M^n to be a vector of $N_{M,i}^n$, with analogous notation applied to other variables.

We start by integrating each of the mass conservation equations over each Ω_i. We show the calculations for methane; the ones for salt are analogous.

Accumulation and source terms. For each i, n we calculate the approximation of accumulation and source terms as follows

$$\int_{\Omega_i} \phi_0 N_M(x, t^n) dx \approx \phi_0(x_i) N_{M,i}^n h. \quad \int_{\Omega_i} f_M(x) dx \approx h f_{M,i}. \tag{11}$$

Advection terms. It suffices to consider only methane advection, since salt advection si treated the same way. We consider first the case $q > 0$. The advective flux

$$\int_{\Omega_i} \nabla \cdot (q \chi_{lM}(x, t^n)) dx \approx q(\chi_{lM,i}^n - \chi_{lM,i-1}^n) \tag{12}$$

is handled by upwinding. Close to the inflow boundary at $i = 1$, we set $\chi_{lM,0}^n$ to the boundary value χ_{lM}^0. If $q < 0$, we replace the right hand side by $\chi_{lM,i+1}^n - q\chi_{lM,i}^n$, and use the boundary condition χ_{lM}^L on top of the reservoir.

Diffusion terms. For the spatially dependent diffusion coefficient $D_M(x)$ and the variable $\chi_{lM}(x)$ we have, in a standard way [30,31]

$$-\int_{\Omega_i} \nabla \cdot D_M \nabla \chi_{lM} dx \approx -h\left(\frac{D_{M,i+1/2}(\chi_{lM,i+1}-\chi_{lM,i}) - D_{M,i-1/2}(\chi_{lM,i}-\chi_{lM,i-1})}{h^2}\right) \quad (13)$$

where $D_{M,i+1/2}, D_{M,i-1/2}$ are found by harmonic averaging of the values $D_{M,i}, D_{M,i+1}$ and $D_{M,i}, D_{M,i-1}$, respectively. Close to the boundary we apply the discretization described in [32], e.g., at $i = 1$ in place of $\chi_{lM,0}$ we use the boundary value χ^0_{lM}, with $D_{M,1/2}$ set to $2D_{M,1}$.

We also define the discrete diffusion matrix A with the entries defined so that $h(A\chi_{lM})_i$ is equal to the right hand side of Equation (13). In particular, $A_{ii} = \frac{D_{M,i-1/2}+D_{M,i+1/2}}{h^2}$. With Dirichlet boundary conditions A is symmetric and positive definite, as long as $D > 0$. In 1d A is also tridiagonal. Further, since D_M depends on $\phi_0 S_l$ as in Table 1, the matrix $A = A(S_l)$ depends on the local saturation values. Finally, since $D_M = D_S$ and the type of boundary conditions on χ_{lM} matches that for χ_{lS}, the matrix for salt equation is the same as that for methane.

3.4. Advection Step

The time-stepping variants considered in this paper are explicit in the advection. This allows development of higher-order schemes as well as avoids additional numerical diffusion associated with implicit treatment of advection [24–26]. With this step, we have to consider appropriate boundary conditions which in the operator splitting come from Equations (6b),(6c); in the advection step we can only impose the boundary condition on the inflow boundary.

In the 1D case considered here $\nabla \cdot q = 0$ implies that q is constant, thus the inflow boundary is determined by the sign of q. If $q > 0$, the inflow bundary is at the bottom of the reservoir at $x = 0$, otherwise it is at $x = L$. In the advection step, we must know χ_{lM} and χ_{lS} on the inflow boundary, and we use here exactly two of Equations (6b),(6c).

The advection step is as follows. Given N^n_M from previous time step, with the corresponding χ^n_{lM}, we can easily calculate $N^{n+1/2}_M$

$$\frac{\phi_0 N^{n+1/2}_M - \phi_0 N^n_M}{\tau} + \nabla \cdot (q\chi^n_{lM}) = 0 \quad (14a)$$

where the terms $\nabla\cdot$ are approximated by Equation (12). Rearranging Equation (14a) we obtain an explicit expression for the methane amount $\phi_0 N^{n+1/2}_{M,i}$ at the intermediate auxiliary time $t^{n+1/2}$

$$\phi_0 N^{n+1/2}_{M,i} = \phi_0 N^n_{M,i} - \frac{q\tau}{h_i}(\chi^n_{M,i} - \chi^n_{M,i-1}) = 0. \quad (15)$$

As is well known, stability of this explicit advection scheme requires that

$$\frac{|q|\tau}{\phi h} \leq 1 \quad (16)$$

via the well-known Courant-Friedrichs-Lévy (CFL) condition [33] adapted to porous media.

Advection scheme for $N^{n+1/2}_S$ is defined analogously to Equation (15).

3.5. Diffusion Step

Knowing $N^{n+1/2}_M$ and $N^{n+1/2}_S$ from the advection step, we solve the coupled diffusion/phase behavior system for N^{n+1}_M and N^{n+1}_S with the boundary conditions Equations (6b),(6c). To distinguish

between the variants and avoid additional superscripts, we reserve the notation N_M^{n+1} and N_S^{n+1} for the solutions to the fully implicit variant I.

First we recall that with Equation (13) and matrix A we have the vector equation

$$\frac{\phi_0 N_M^{n+1} - \phi_0 N_M^{n+1/2}}{\tau} + A(S_l^n)\chi_{lM}^{n+1} = f_M^{n+1} \tag{17}$$

Note the time lagging of the dependence of matrix A on S_l.

For N_S^{n+1} we have an equation analogous to Equation (17). Additionally, we need to account for [NCC-M]. This coupled system of two component diffusion and phase equilibria is solved with one of the three variants: fully implicit (I), semi-implicit (SI), and sequential (SEQ). See Figure 1 for graphical illustration of the operator splitting and different variants.

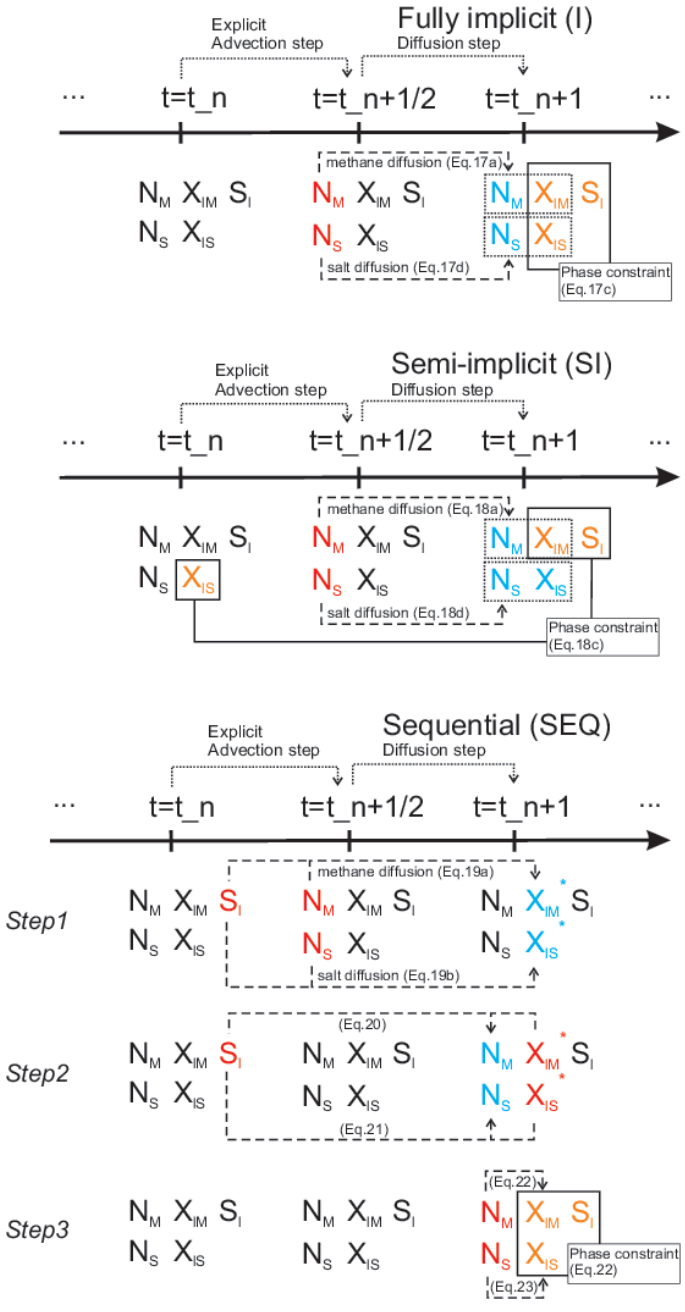

Figure 1. Illustration of time stepping variants.

3.5.1. Variant (I): Fully Implicit

The fully implicit variant solves the coupled two-component diffusion/phase behavior system for $(S_l^{n+1}, \chi_{lM}^{n+1}, \chi_{lS}^{n+1})$ as follows

$$\frac{\phi_0 N_M^{n+1} - \phi_0 N_M^{n+1/2}}{\tau} + A\chi_{lM}^{n+1} = f_M^{n+1}, \tag{18a}$$

$$N_M^{n+1} = S_l^{n+1}\chi_{lM}^{n+1} + R(1 - S_l^{n+1}). \tag{18b}$$

Here Equation (18b) provides the definition of N_M^{n+1} needed in Equation (18a), and is directly implemented in the code. The two unknowns in Equation (18a) are S_l^{n+1} and χ_{lM}^{n+1}; these are connected to each other via Equations (9) and (4)

$$\min(\chi_{lM}^{max,0}(x) + \alpha(x)\chi_{lS}^{n+1} - \chi_{lM}^{n+1}, 1 - S_l^{n+1}) = 0, \tag{18c}$$

with the dependence on χ_{lS}^{n+1} defined directly by

$$\frac{\phi_0 N_S^{n+1} - \phi_0 N_S^{n+1/2}}{\tau} + A\chi_{lS}^{n+1} = 0, \tag{18d}$$

$$N_S^{n+1} = S_l^{n+1}\chi_{lS}^{n+1}. \tag{18e}$$

The Equation (18) is solved using Newton's method for $(S_l^{n+1}, \chi_{lM}^{n+1}, \chi_{lS}^{n+1})$, and the Jacobian of the system is a 3×3 sparse block matrix. Its form and particular pattern of sparsity depend on Equation (18c). Note that in Equation (18) we maintain full consistency of mass conservation between the time steps (up to the tolerance of nonlinear solver), as well as consistency of thermodynamic constraints.

3.5.2. Variant (SI): Semi-Implicit

The semi-implicit variant differs from (18) in the treatment of χ_{lS} in (18c). We time-lag χ_{lS} and remove the two-way coupling between the methane transport and salinity transport. Methane transport in this model is governed by

$$\frac{\phi_0 \widehat{N_M^{n+1}} - \phi_0 N_M^{n+1/2}}{\tau} + A\widehat{\chi_{lM}^{n+1}} = f_M^{n+1}, \tag{19a}$$

$$\widehat{N_M^{n+1}} = \widehat{S_l^{n+1}}\widehat{\chi_{lM}^{n+1}} + R(1 - \widehat{S_l^{n+1}}). \tag{19b}$$

$$\min(\chi_{lM}^{max,0}(x) + \alpha(x)\widehat{\chi_{lS}^{n}} - \widehat{\chi_{lM}^{n+1}}, 1 - \widehat{S_l^{n+1}}) = 0. \tag{19c}$$

so that these equations are solved for $(\widehat{S_l^{n+1}}, \widehat{\chi_{lM}^{n+1}})$ using Newton's method. The Jacobian of the system is a 2×2 sparse block matrix.

Knowing $\widehat{S_l^{n+1}}$ we can solve the system for $\widehat{\chi_{lS}^{n+1}}$ which is linear

$$\frac{\phi_0 \widehat{N_S^{n+1}} - \phi_0 N_S^{n+1/2}}{\tau} + A\widehat{\chi_{lS}^{n+1}} = 0, \tag{19d}$$

$$\widehat{N_S^{n+1}} = \widehat{S_l^{n+1}}\widehat{\chi_{lS}^{n+1}}. \tag{19e}$$

while the mass conservation between the time steps is enforced in this variant, there is potential inconsistency in thermodynamic constraints introduced by the time-lagging in Equation (19c). To correct this, we follow up with the two-variable local flash solver which corrects the saturations and solubilities while keeping $(\widehat{N_M^{n+1}}$, and $\widehat{N_S^{n+1}})$ fixed.

3.5.3. Variant (SEQ): Sequential

The sequential variant is the simplest to implement and one can easily adapt an existing advection-diffusion code. The advantage of this variant is that each of the global algebraic systems is linear. The disdvantage is that the phase behavior is not fully coupled to the transport dynamics, and fine time-stepping may be needed to ensure accuracy.

The SEQ variant time-lags the saturation variable in the methane and salinity transport equations

$$\frac{\phi_0 \widetilde{S_l^n} \widetilde{\chi_{lM}^{n+1,*}} - \phi_0 N_M^{n+1/2}}{\tau} + A\widetilde{\chi_{lM}^{n+1,*}} = f_M^{n+1} - \frac{\phi R(1-\widetilde{S_l^n})}{\tau}, \tag{20a}$$

$$\frac{\phi_0 \widetilde{S_l^n} \widetilde{\chi_{lS}^{n+1,*}} - \phi_0 N_S^{n+1/2}}{\tau} + A\widetilde{\chi_{lS}^{n+1,*}} = 0. \tag{20b}$$

Note that the phase constraint is not imposed in Equation (20), and that the equations are not coupled. We solve them for the temporary unknowns $\widetilde{\chi_{lM}^{n+1,*}}, \widetilde{\chi_{lS}^{n+1,*}}$, and next we recalculate the mass concentrations corresponding to the new solubilities from Equations (19b),(19e)

$$\widetilde{N_M^{n+1}} = \widetilde{S_l^n}\widetilde{\chi_{lM}^{n+1,*}} + R(1-\widetilde{S_l^n}). \tag{21}$$

$$\widetilde{N_S^{n+1}} = \widetilde{S_l^n}\widetilde{\chi_{lS}^{n+1,*}}. \tag{22}$$

To keep these consistent with Equation (9), we invoke the nonlinear two variable flash solver. Its input are the mass concentrations $\widetilde{N_M^{n+1}}, \widetilde{N_S^{n+1}}$, and its output are the final new values of solubilities $\widetilde{\chi_{lM}^{n+1}}, \widetilde{\chi_{lS}^{n+1}}$, and saturations $\widetilde{S_l^{n+1}}$ which satisfy the discrete version of Equation (9) plus the mass concentration definitions

$$\min(\chi_{lM}^{max,0}(x) + \alpha(x)\widetilde{\chi_{lS}^{n+1}} - \widetilde{\chi_{lM}^{n+1}}, 1 - \widetilde{S_l^{n+1}}) = 0. \tag{23}$$

$$\widetilde{N_M^{n+1}} = \widetilde{S_l^{n+1}}\widetilde{\chi_{lM}^{n+1}} + R(1-\widetilde{S_l^{n+1}}). \tag{24}$$

$$\widetilde{N_S^{n+1}} = \widetilde{S_l^{n+1}}\widetilde{\chi_{lS}^{n+1}}. \tag{25}$$

The flash solver for Equations (23) (24) and (25) provides the consistency between the mass-related variables and thermodynamic constraints. However, the mass conservation between time steps is not strictly enforced due to time-lagging.

4. Comparison of Performance of the Time Stepping Variants

In this section we evaluate the accuracy, robustness and computational complexity of the proposed I, SI, and SEQ variants of hydrate models using realistic scenarios of methane hydrate formation in typical sediments. We also give details on what time steps appear reasonable, and how to choose discretization parameters.

In oil-gas reservoir simulation the fully implicit algorithms implement directly the backward Euler formula. The fully implicit formulations are usually the most accurate, but also most complex to implement. In turn, sequential and semi-implicit variants are typically less accurate but, at least in principle, they have smaller computational complexity per time step, and are easier to implement than the fully implicit algorithms. Typically, the results of non-implicit schemes converge to those of fully implicit models as $\tau \to 0$. In fact, non-implicit variants may require small τ in in order to resolve, e.g., complicated phase equilibria, heterogeneity, or complex well behavior; the use of small τ somewhat erases the benefits of small computational cost per time step. The non-implicit variants may still have advantages in the easiness of implementation.

The computational experiments we set up to test the variants I, SI, and SEQ are built from the following base case similar to those in [3] for the methane hydrate and salinity conditions in Ulleung Basin.

We set $\Omega = (0, L)$ with $L = 159$ m, and use uniform porosity $\phi = 0.5$. We vary q from large $q = 0.1$m/yr for which advection dominates, to the case where diffusion is dominant and $q \leq 0.001$m/yr. We assume that advection and diffusion provide the only transport mechanisms and that $f_M = 0 = f_S$, that is, the only sources of methane are from upward fluxes. For thermodynamics we use the reduced model Equation (4) and [NCC-M] constraint is implemented with Equation (9). Unless otherwise specified, we use the data $\chi^0_{max}(x)$ and $\alpha(x)$ calibrated for Ulleung Basin and shown in Figure 6, with the same boundary and initial conditions. We use zero initial conidtions for methane, and assume that the initial distribution of salinities varies linearly between the boundary conditions χ^0_{lS} and χ^M_{lS}. We run simulations until $T = 10^5$yr $= 100$Kyr, or until S_h reaches the unphysical values close to 1.

Discretization parameters are chosen as follows. We use $N_x = 100$ with $h = 1.59$ in the base case. The time step is subject to the CFL constraint Equation (16). In particular for $q = 0.01$ the largest time step $\tau_{CFL} \approx 78$yr.

For illustration of the base case in Figure 2 we show the evolution of S_h and χ_{lS} for the case $q = 0.01$m/yr, with small $\tau = 1$yr. In this case of strong advective flux the hydrate forms quickly and fills up the domain. These results are similar to those in [3] and more generally to the test cases in [4]. The evolution of salinity shows that there is a boundary layer close to the outflow which forms around $T = 10K$ and remains unchanged afterwards.

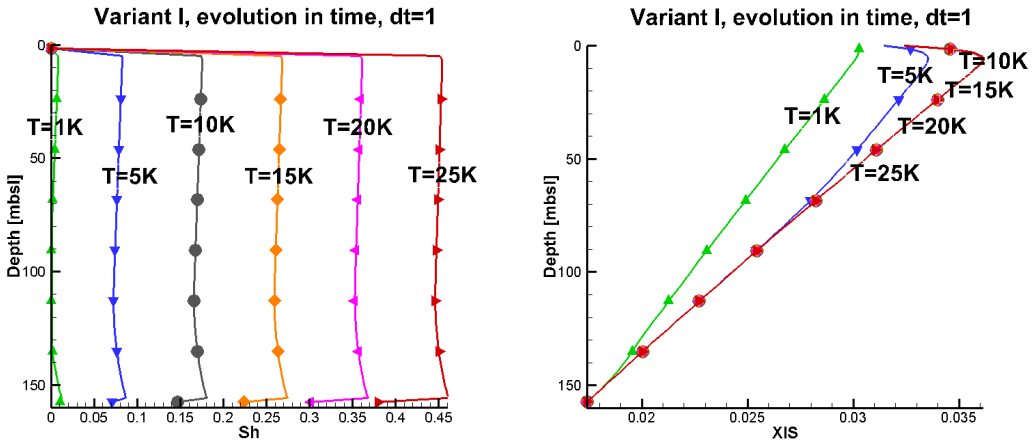

Figure 2. Evolution of hydrate saturation and of salinity for the base case. **Left**: plot of S_h, **right**: plot of χ_{lS}. Variable χ_{lM} equals χ^{max}_{lM} at these times and is not shown.

4.1. Accuracy of the Time-Stepping Variants and Choice of Time Step

Here we study the sensitivity to τ which can guide its choice. In general, one wants to use small enough τ obeying the upper bound (16) and such that its further decrease does not have much influence. However, small τ means large number $\frac{T}{\tau}$ of time steps; this is significant in hydrate basin simulations since $\frac{T}{\tau}$ may be easily 10^4 or more. Further, as suggested by our experience from oil-gas reservoir simulations [10,11,13], we expect that for small τ the results of the three variants I, SI, SEQ are very similar, and that for large τ they differ.

In Figure 3 we present the plots of S_h obtained for different τ. Quantitative information supporting these observations is included in Table 2. (We do not present details concerning the evolution of χ_{lS} since the results differ by less than 0.01% in each case.) We notice that the results corresponding to $\tau = 1$ and the variants I, SI, and SEQ are essentially indistinguishable; this degree

of closeness is more than expected. In addition, the results corresponding to the largest advection step $\tau = 78$ and to the variants I, SI and SEQ are close to each other as well; they tend to overpredict those for $\tau = 1$.

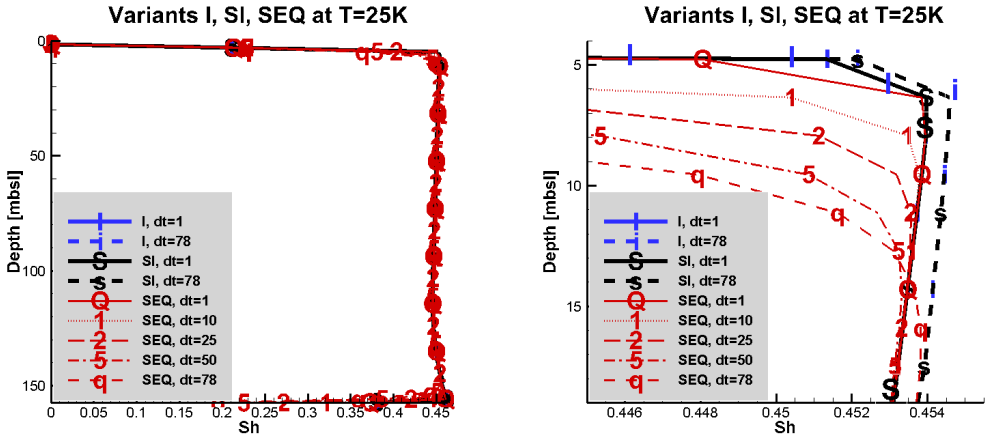

Figure 3. Plots of S_h for different time steps τ (denoted on figure by dt), and different time-stepping variants fully implicit (I), semi-implicit (SI), and sequential (SEQ). **Left**: plots over the full range of depth and S_h are essentially indistinguishable. **Right**: the zoom of the left plot shows a small sensitivity to the choice of time step and of the model variant.

Table 2. Maximum hydrate saturation S_h obtained with different model variants and time steps at $T = 10K$ and $T = 25K$, all parameters as in base case.

τ	**SEQ**	**SI**	**I**
		$T = 10K$	
78	0.177208	0.182844	0.182844
70	0.176441	0.181803	0.181803
50	0.176834	0.181267	0.181267
25	0.177841	0.180908	0.180908
10	0.178834	0.180736	0.180736
5	0.179238	0.180688	0.180688
1	0.180183	0.180651	0.180651
		$T = 25K$	
78	0.456162	0.463925	0.463925
70	0.456803	0.464271	0.464271
50	0.45644	0.462797	0.462797
25	0.457708	0.462438	0.462438
10	0.458886	0.462266	0.462266
5	0.459731	0.462218	0.462218
1	0.460878	0.462181	0.462181

In addition, we see that the model SEQ is potentially the most sensitive of all three to τ close to the boundaries and in areas with larger methane gradients. (This suggests the need for adaptive gridding). In addition, as τ decreases, the results tend to converge to the value for $\tau = 1$. Further decrease of τ (not shown here) does not influence the solution much, thus $\tau = 1$ appears as the smallest sensible choice for this N_x.

4.2. Robustness and Efficiency of the Variants

Above we established that the simulated hydrate saturation values do not seem to significantly depend on the time step τ or on the variant of time stepping. Next we consider the robustness of the variants and in particular, how they handle difficult physical circumstances such as when S_h is large due to large advective fluxes.

In Table 3 we report on the performance of the nonlinear solver, tested intentionally without any fine-tuning such as line-search. We see that between $T = 25K$ and $T = 50K$ all variants I, SI, SEQ struggle when $\tau \geq 25$. The model I appears somewhat more robust than the other two and it can simulate the hydrate evolution up to higher values.

Table 3. Robustness of nonlinear solvers depending on the variant and the time step for the simulations of the base case between $T = 25K$ and $T = 50K$. The robustness is assessed by checking which solver variant is more prone or more robust to failing in the difficult modeling circumstances close to unphysical. We report the critical value S_h^{crit} obtained before the solver fails, and on the number N_{it} of iterations. When N_{it} is denoted by "-", this means the solver did not complete. For SEQ model, N_{it} denotes the number of flash iterations. For the SI and I models, N_{it} denotes the number of global Newton iterations.

τ	**SEQ**		**SI**		**I**	
	S_h^{crit}	N_{it}	S_h^{crit}	N_{it}	S_h^{crit}	N_{it}
78	0.75833	-	0.767473	-	0.773341	-
70	0.772449	-	0.782752	-	0.781435	-
50	0.806955	-	0.817198	-	0.817198	-
25	0.873396	-	0.880766	-	0.880766	-
10	0.925712	2	0.932267	2	0.932267	3
5	0.926744	2	0.93222	2	0.93222	3

Dependence of the results on q. Next, it is known that the advective fluxes are the hardest physically to handle for hydrate systems, since they provide the source for the fastest hydrate formation.

To test our solvers, we consider the advection-dominated case with large and moderate q, down to the purely diffusive case with $q = 0$. In Figure 4 we present the plots of hydrate saturations at $T = 31K$ for different fluxes q. In addition, in Table 4 we report the time T_I when the computational model I predicts that $\max_x S_h(x, T_I) \approx 0.5$. We also report the values T_{SI} and T_{SEQ} also for the variants SI and SEQ.

We see that the variants I and SI report essentially the same values. In fact, a close inspection reveals that the model results differ in less than 0.001% between I and SI for the time steps we used in our implementation. This experiment shows again the robustness of all variants with respect to q, with a slight advantage of the implicit variants.

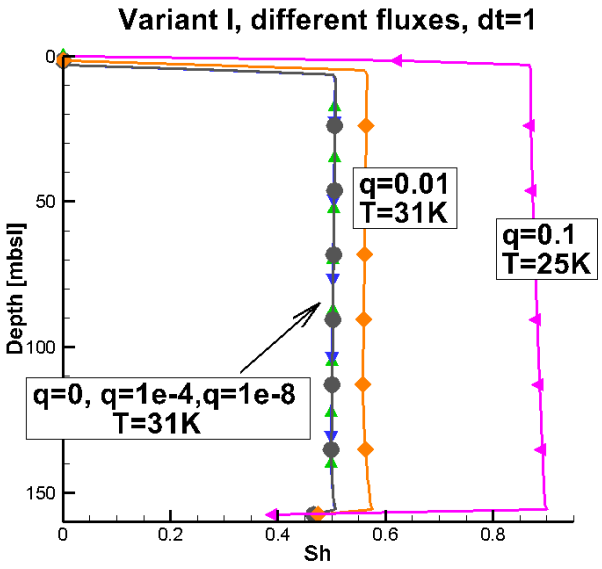

Figure 4. Hydrate saturation at $T = 31K$ when different advective fluxes are assumed. For $q = 0.1$ for which high saturation is attained already at $T = 25K$ we do not show the plot at $T = 31K$.

Table 4. The time T when $\max S_h \approx 0.5$ depending on q, for the base case for each time-stepping variant, respectively, T_I, T_{SI}, T_{SEQ}. Here we use $\tau = 1$.

q	T_I	T_{SI}	T_{SEQ}
0.1	13917	13917	13972
0.01	27014	27014	27091
0.005	28629	28629	28691
0.0001	30568	30568	30587
1e-8	30614	30614	30624

Computational time and the choice of time step. Finally, we evaluate the computational complexity of the variants, and this is done by comparing the wall clock times for our MATLAB implementation. In order to compare the solvers on equal footing, no additional code vectorization is implemented, but the code takes advantage of the natural MATALB vector data types. In Table 5 we report the wall clock time.

In general, one expects that for the same time step τ the SEQ model is faster than SI and I, since SEQ only uses global linear solvers and local nonlinear flash routines. However, we see that all solvers require similar amounts of computational time, with a slight advantage of model SI. This may be due to the lack of vectorization applied in local flash routines, while the global linear solvers are naturally vectorized in MATLAB. In addition, the SEQ solver computes more local variables than SI and I.

Since with uniform τ the total computational time scales proportionally to the number of time steps, the choice of τ balances the desired accuracy and computational time. For the case considered here it seems that the time step $\tau = 10$ may be the best practical choice.

The efficiency of the solvers may be very different in 2d or 3d simulations, and we intend to report on these in the future.

Table 5. Comparison of computational wall clock time $T^w[s]$ for the three model variants and different time steps, for the base case and $T = 25K$

τ	$T^w_{\mathbf{SEQ}}$	$T^w_{\mathbf{SI}}$	$T^w_{\mathbf{I}}$
1	591.801	439.806	441.394
10	60.2528	44.0688	47.6352
50	11.8322	8.81442	9.63327
78	7.55206	5.655	6.08011

5. Sensitivity to Physical and Coputational Parameters

For a computational model it is crucial to determine what discretization parameters one should use for a given model. In addition, it is important to investigate the sensitivity of the model to the data on $\alpha(x)$ in Equation (4).

Discretization parameters. As the discretization parameters $h, \tau \to 0$ and the numbers of cells $N_x = \frac{L}{h}$ and time steps increase, it is expected that the numerical solutions of a PDE model converge to the analytical ones in an appropriate sense dictated by the theoretical numerical analysis. The convergence studies for the purely diffusive one component case of Equation (3) in [17] suggest to vary τ wit h either linearly or faster, and to consider various metrics of convergence in appropriate functional spaces. For the present case with significant advection q and variable salinity, we expect the rates to be inferior of the approximate $O(h + \tau)$ rates observed in [17]. The theoretical analysis is underway and will be presented elsewhere.

Here we choose $\tau = O(h)$ and the implicit model; in Figure 5 and Table 6 we present the evidence which confirms that as h decreases, the results seem to converge. At the same time it is obvious that the convergence in saturations is quite rough, as observed earlier in [34].

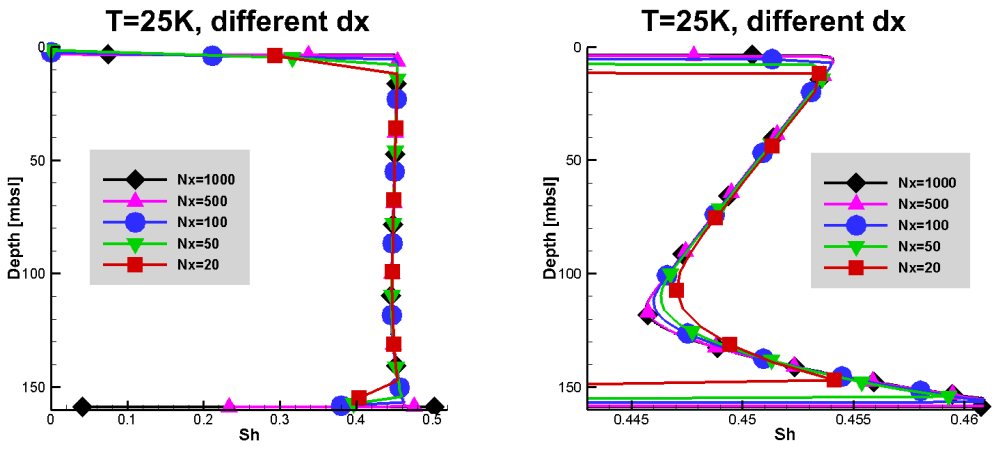

Figure 5. Hydrate saturation for different N_x and h denoted by dx. See Table 6 for the related quantitative information extracted from the simulations.

Table 6. Accuracy and complexity of the computational model depending on N_x, with the time step τ adjusted to vary linearly with h. As the quantity of interest depending on N_x we show the saturation values at $T = 25K$. This table complements the plots in Figure 5.

N_x	h	τ	$\max S_h$	**Wall-Clock Time**
10	15.9	10	0.453079	5.6533
25	6.36	4	0.455525	32.644
50	3.18	2	0.459280	121.411
100	1.59	1	0.462181	489.101
200	0.795	0.5	0.465253	2301.53

The question then is what choice of h and τ balance the conflicting need to decrease the computational time as well as to increase the accuracy, while maintaining an adequate model resolution. From the results presented, we suggest that $N_x = 100$ or $N_x = 50$ corresponding to the discretization in space $h \approx 1$m and in time $\tau \approx 1$yr are a good choice, since they appear to keep the simulation results within the uncertainty envelope that might not be verifiable experimentally.

However, the sensitivity to τ and h at the boundaries needs to be addressed by a more accurate and adaptive formulation especially if nonhomogeneous sediments and/or additional physics are considered.

Sensitivity to the parameters of the reduced model Equation (4). There is large uncertainty as to what χ_{lM}^{max} one should use. In particular, there may be an error associated with the look-up table process of finding α described in [3] and due to the lack of information on salinity. More broadly, in a comprehensive model χ_{lM}^{max} depends on the unknown pressure and temperature values, and possibly rock type, thus further variability and uncertainty of $\alpha(x)$ should be expected.

We set up therefore test cases to assess this sensitivity. We dub the values of $\alpha(x)$ obtained for Ulleung Basin in [3] the "true" $\alpha_{\text{true}}(x)$. Next we simulate the hydrate formation with $\alpha(x) = c\alpha_{\text{true}}(x)$ with $c = 1, c = 10$ and $c = -1$. Furthermore, we consider a constant value equal to the average of the true $\alpha(x) = \frac{1}{|\Omega|}\int_\Omega \alpha_{\text{true}}(x)dx$, and another $\alpha(x)$ which randomly perturbs $\alpha_{\text{true}}(x)$. The different cases of α are shown in Figure 6, with the corespnding χ_{lM}^{max} which we calculated, for illustration purposes, assuming $\chi_{lS} = \chi_{lS}^{sw}$. In Figure 7 we show the profiles of S_h at $T = 25K$ coresponding to the different $\alpha(x)$.

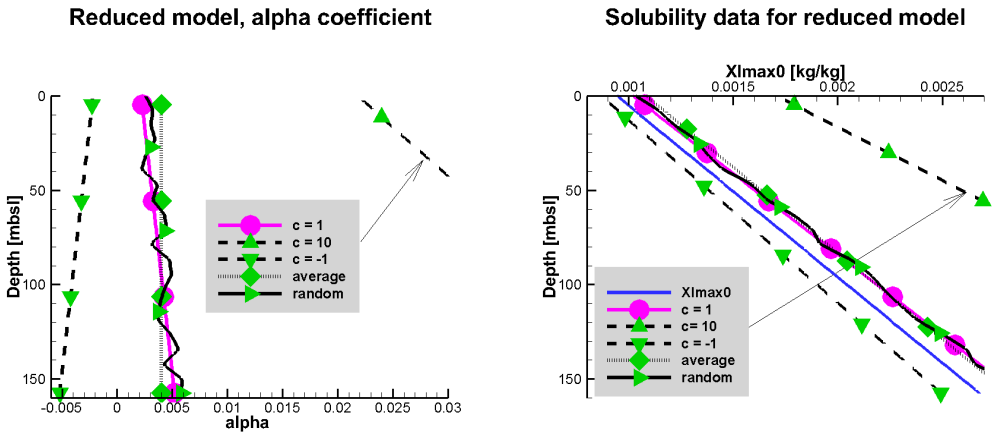

Figure 6. Parameter $\alpha(x)$ as a function of depth used in Section 5 (**left**) and the corresponding $\chi_{lM}^{max,0}(x)$ computed from Equation (4) and assuming $\chi_{LS} \approx \chi_{ls}^{sw}$ (**right**). On right the plot of $\chi_{lM}^{max,0}(x)$ is also shown. The base case from Ulleung Basin [3] in both plots is denoted with circles. The other cases correspond to $c = -1$, $c = 10$, the average of $\alpha(x)$, and to a randomly perturbed $\alpha(x)$. The plots for $c = 10$ are out of range and are not fully included.

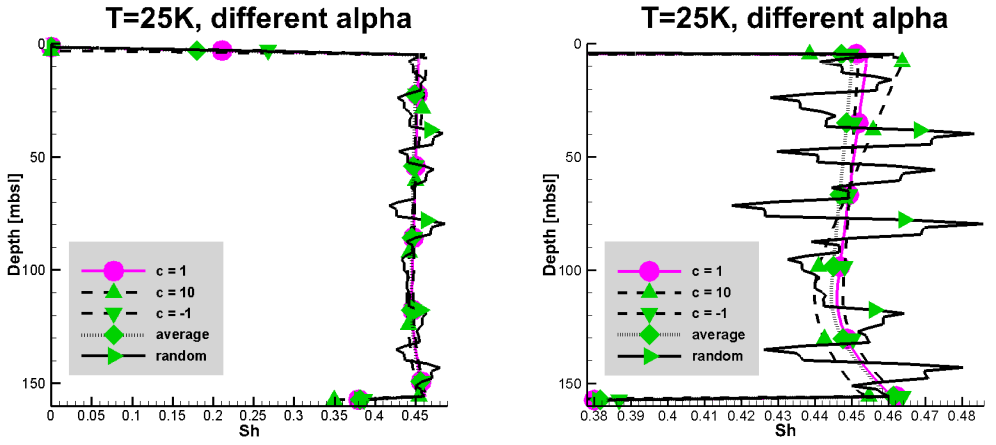

Figure 7. Hydrate saturation for different coefficients α. The figure on the right is a zoomed in version of that on the left.

Comparing the hydrate saturation for $c = -1$ and $c = 10$ shown in Figure 7 to the base case with $c = 1$ we see that since χ_{lM}^{max} is significantly higher when $c = 10$, somewhat less hydrate forms. On the other hand, a randomly pertubed $\alpha(x)$ gives χ_{lM}^{max} with large local variation, and this is reflected in the corresponding hydrate saturation. This significant sensitivity appears to be of qualitative nature, and requires further studies.

6. Conclusions

In this paper we described the details of the discretization and implementation of a reduced methane hydrate model with variable salinity and significant advection proposed in [3]. We carried out several convergence and parameter studies to show that the model is robust and computationally sound. Studies of this type have not been provided for the simplified or the comprehensive implicit hydrate models from literature, but are crucial to guide the implementation and to inspire further theoretical and algorithmic developments.

In particular, we defined several time stepping variants: implicit I, semi-implicit SI, and sequential SEQ, which were tested and compared using realistic reservoir data from [3]. We found, somewhat surprisingly, that the I and SI variants give almost identical results; this may be explained by only a mild dependence of the model on the salinity variable whose treatment differs in I and SI. Furthermore, in the current implementation and 1d test cases there is no significant advantage in one variant over the others as concerns accuracy, robustness, or efficiency. Still, the I model appears as expected somewhat most robust, while SEQ is the easiest to implement by modifying standard advection-diffusion solvers. We also demonstrated the apparent convergence of the solutions when $h, \tau \to 0$, and determined practical choices of h, τ. In addition, there is apparent need for grid and model refinement near the boundaries.

Furthermore, we demonstrated the small sensitivity of the reduced thermodynamics model proposed in [3] to the particular value of the coefficient α as long as it is qualitatively close to the one from the reservoir data and is monotone. However, a randomly perturbed and nonmonotone α reveals large sensitivity, and we plan to investigate the reasons further.

Our future work includes theoretical and practical studies of the model convergence as well as its efficiency. There is further need to study additional sets of realistic data and thermodynamics models, and to consider extensions to more complex physical problems.

Acknowledgments: Malgorzata Peszynska and Francis Patricia Medina's research was partially supported by the NSF DMS-1115827 "Hybrid modeling in porous media" and by DMS-1522734 "Phase transitions in porous media across multiple scales". Marta E. Torres and Wei-Li Hong were supported by US Department of Energy grant #DE-FE00135331 and by the Research Council of Norway through its Centres of Excellence funding scheme, project 223259. The authors thank the anonymous reviewers for their comments which helped to improve the manuscript.

Author Contributions: Malgorzata Peszynska, Marta E. Torres and Wei-Li Hong adapted the reduced model to the case study from Ulleung Basin. Malgorzata Peszynska and Wei-Li Hong implemented the reduced model; Malgorzata Peszynska and Francis Patricia Medina set up and tested the numerical model.

Conflicts of Interest: The authors declare no conflict of interest.

References

1. Dickens, G.R. Rethinking the global carbon cycle with a large, dynamic and microbially mediated gas hydrate capacitor. *Earth Planet. Sci. Lett.* **2003**, *213*, 169–183.
2. Torres, M.; Wallmann, K.; Tréhu, A.; Bohrmann, G.; Borowski, W.; Tomaru, H. Gas hydrate growth, methane transport, and chloride enrichment at the southern summit of Hydrate Ridge, Cascadia margin off Oregon. *Earth Planet. Sci. Lett.* **2004**, *226*, 225 – 241.
3. Peszynska, M.; Hong, W.L.; Torres, M.; Kim, J.H. Methane hydrate formation in Ulleung Basin under conditions of variable salinity. Reduced model and experiments. **2015,** submitted.
4. Liu, X.; Flemings, P.B. Dynamic multiphase flow model of hydrate formation in marine sediments. *J. Geophys. Res.* **2007**, *112*, B03101.
5. Lake, L.W. *Enhanced Oil Recovery*; Prentice Hall: Upper Saddle River, NJ, USA, 1989.
6. Helmig, R. *Multiphase Flow and Transport Processes in the Subsurface*; Springer: Berlin, Germany, 1997.
7. Class, H.; Helmig, R. Numerical simulation of non-isothermal ultiphase multicomponent processes in porous media 2. Applications for the injection of steam and air. *Adv. Water Resour.* **2002**, *25*, 533–550.
8. Trangenstein, J.A.; Bell, J.B. Mathematical structure of the black-oil model for petroleum reservoir simulation. *SIAM J. Appl. Math.* **1989**, *49*, 749–783.
9. Chen, Z.; Khlopina, N.L. Degenerate two-phase incompressible flow problems. I. Regularization and numerical results. *Commun. Appl. Anal.* **2001**, *5*, 319–334.
10. Lu, Q.; Peszyńska, M.; Wheeler, M.F. A Parallel Multi-Block Black-Oil Model in Multi-Model Implementation. *SPE J.* **2002**, *7*, 278–287.
11. Peszyńska, M.; Lu, Q.; Wheeler, M.F. Multiphysics Coupling of Codes. In *Computational Methods in Water Resources*; Balkema: Leiden, The Netherlands, 2000.

12. Wheeler, M.F.; Wheeler, J.A.; Peszyńska, M. A Distributed Computing Portal for Coupling Multi-Physics and Multiple Domains in Porous Media, *Computational Methods in Water Resources*; Balkema: Leiden, The Netherlands, 2000.
13. Wheeler, M.F.; Peszyńska, M. Computational Engineering and Science Methodologies for Modeling and Simulation of Subsurface Applications. *Adv. Water Resour.* **2002**, *25*, 1147–1173.
14. Coats, K.H.; Thomas, L.K.; Pierson, R.G. Compositional and black oil reservoir simulator. *SPE Reserv. Eval. Eng.* **1995**, *1*, 372–379.
15. Xu, W.; Ruppel, C. Predicting the occurence, distribution, and evolution of methane hydrate in porous marine sediments. *J. Geophys. Res.* **1999**, *104*, 5081–5095.
16. Nimblett, J.; Ruppel, C. Permeability evolution during the formation of gas hydratees in marine sediments. *J. Geophys. Res.* **2003**, *108*, B9.
17. Gibson, N.L.; Medina, F.P.; Peszynska, M.; Showalter, R.E. Evolution of phase transitions in methane hydrate. *J. Math. Anal. Appl.* **2014**, *409*, 816 – 833.
18. Peszynska, M.; Showalter, R.; Webster, J. Advection of Methane in the Hydrate Zone: Model, Analysis and Examples. *Mathe. Methods Appl. Sci.* **2014**, doi:10.1002/mma.3401.
19. Rempel, A.W. Hydromechanical Processes in Freezing Soils. *Vadose Zone J.* **2012**, *11*, 4.
20. Sloan, E.; Koh, C.A. *Clathrate Hydrates of Natural Gases*, 3rd ed.; CRC Press: Leiden, The Netherlands, 2008.
21. Daigle, H.; Dugan, B. Capillary controls on methane hydrate distribution and fracturing in advective systems. *Geochem. Geophys. Geosyst.* **2011**, *12*, 1–18.
22. Center for Hydrate Research Software CSMHYD and CSMG accessed April 9, 2015.
23. Zatsepina, O.; Buffett, B. Phase equilibrium of gas hydrate: Implications for the formation of hydrate in the deep sea floor. *Geophys. Res. Lett.* **1997**, *24*, 1567–1570.
24. Dawson, C.N. Godunov-mixed methods for advection-diffusion equations in multidimensions. *SIAM J. Numer. Anal.* **1993**, *30*, 1315–1332.
25. Dawson, C.N.; Wheeler, M.F. Time-splitting methods for advection-diffusion-reaction equations arising in contaminant transport. In Proceedings of the second International Conference on Industrial and Applied Mathematics, SIAM: Philadelphia, PA, USA, 1992.
26. Wheeler, M.F.; Dawson, C.N. An operator-splitting method for advection-diffusion-reaction problems. In *The Mathematics of Finite Elements and Applications VI*; Whiteman, J.R., Ed.; Academic Press: London, UK, 1987; pp. 463–382.
27. Ito, K.; Kunisch, K. Semi-smooth Newton methods for variational inequalities of the first kind. *M2AN Math. Model. Numer. Anal.* **2003**, *37*, 41–62.
28. Ulbrich, M. *Semismooth Newton Methods for Variational Inequalities and Constrained Optimization Problems in Function Spaces*; *Vol. 11, MOS-SIAM Series on Optimization*, Society for Industrial and Applied Mathematics (SIAM): Philadelphia, PA, USA, 2011.
29. Gharbia, I.B.; Jaffre, J. Gas phase appearance and disappearance as a problem with complementarity constraints. *Math. Comput. Simul.* **2014**, *99*, 28–36.
30. Peaceman, D.W. *Fundamentals of Numerical Reservoir Simulation*; Elsevier Scientfic Publishing Company: Amsterdam, The Netherlands, 1977.
31. Russell, T.F.; Wheeler, M.F. Finite element and finite difference methods for continuous flows in porous media. In *The Mathematics of Reservoir Simulation*; Ewing, R.E., Ed.; SIAM: Philadelphia, PA, USA, 1983.
32. Peszyńska, M.; Jenkins, E.; Wheeler, M.F. Boundary conditions for fully implicit two-phase flow model. In *Recent Advances in Numerical Methods for Partial Differential Equations and Applications*; American Mathematical Soc.: Ann Arbor, MI, USA, 2002.
33. LeVeque, R.J. *Finite Difference Methods for Ordinary and Partial Differential Equations*; Society for Industrial and Applied Mathematics (SIAM): Philadelphia, PA, USA, 2007.
34. Peszyńska, M.; Torres, M.; Tréhu, A. Adaptive modeling of methane hydrates. *Procedia Computer Sci.* **2010**, *1*, 709-717.

Temporal resilience and dynamics of anaerobic methane-oxidizing microbial communities to short-term changes in methane partial pressures

Scott Klasek[1], Tiantian Yu[2], Marta Torres[3], Frederick Colwell[1,3] and Fengping Wang[2]

1 Department of Microbiology, Oregon State University, Corvallis, Oregon, USA
2 State Key Laboratory of Microbial Metabolism and State Key Laboratory of Ocean Engineering, Shanghai Jiao Tong University, Shanghai, People's Republic of China
3 College of Earth, Ocean, and Atmospheric Sciences, Oregon State University, Corvallis, Oregon, USA

Marine sediments produce tens to hundreds of teragrams of methane annually, which is released from the seabed at thousands of cold seeps distributed globally along continental margins. Around 80-90% of this methane is consumed in shallower sediment layers before reaching the hydrosphere, in a microbially-mediated process known as anaerobic oxidation of methane (AOM) However, cold seeps appear to exhibit temporal variation in gas flux intensity, and AOM filter efficiency at cold seeps generally decreases with fluid flow rate. To our knowledge, the degree to which temporal heterogeneity in subsurface methane flux stimulates AOM community growth and adaptation to increased methane concentrations has not been investigated. Static high-pressure bioreactors were used to incubate sulfate-methane transition zone (SMTZ) and methanogenic zone sediments underlying a Mediterranean mud volcano gas flare under *in situ* temperature and pressure at 8 MPa methane. Sulfide production rates of 0.4 μmol/cm^3/day in both sediment regimes after 4 months of incubation suggested the resilience of the marine subsurface methane filter may extend well below the SMTZ (40 cm). Similar incubations of SMTZ samples from below a gas flare off Svalbard at saturating (3.8 MPa) and 0.2 MPa methane are being sampled after 1 week, 4 weeks, and 4 months; sulfide production rates of 8-18 nmol/cm^3/day were first observed after 4 weeks of incubation. Sediment samples at all specified time points for both sets of incubations were collected for nucleic acid extraction and cell fixation. Anaerobic methanotrophic archaea (ANME) and sulfate-reducing bacteria (SRB) are expected dominant taxa in enriched and non-enriched communities. 16S rDNA community analysis is expected to reveal additional microbial players involved in the short-term adaptation to higher methane partial pressures in the marine subsurface. Increased AOM community activity (RNA/DNA ratio) and copy numbers of methane cycling transcripts (*mcrA, dsrAB*) are anticipated at longer enrichments and higher methane concentrations. A more thorough understanding of AOM community dynamics in response to changes in methane concentrations is expected to yield more accurate carbon cycling models pertaining to the world's largest reduced carbon reservoir.

National Energy Technology Laboratory

626 Cochrans Mill Road
P.O. Box 10940
Pittsburgh, PA 15236-0940

3610 Collins Ferry Road
P.O. Box 880
Morgantown, WV 26507-0880

13131 Dairy Ashford, Suite 225
Sugarland, TX 77478

1450 Queen Avenue SW
Albany, OR 97321-2198

2175 University Ave. South
Suite 201
Fairbanks, AK 99709

Visit the NETL website at:
www.netl.doe.gov

Customer Service:
1-800-553-7681